DEPARTMENT OF PHYSICS

UNRAVELING SPIN CURRENT CONTROL IN SOLUTION-PROCESSED-ORGANIC MATERIAL SYSTEMS

DOCTOR OF PHILOSOPHY DISSERTATION

CONSTANTINOS NICOLAIDES

2023

DEPARTMENT OF PHYSICS

UNRAVELING SPIN CURRENT CONTROL IN SOLUTION-PROCESSED-ORGANIC MATERIAL SYSTEMS

CONSTANTINOS NICOLAIDES

A Dissertation Submitted to the University of Cyprus in Partial Fulfillment of the Requirements for the Degree of Doctor of Philosophy

OCTOBER 2023

VALIDATION PAGE

Doctoral Candidate : Constantinos Nicolaides

Doctoral Thesis Title : Unraveling spin current control in solution-processed-organic material systems

The present doctoral dissertation was submitted in partial fulfillment of the requirements for the Degree of Doctor of Philosophy at the ***Department of Physics*** *and was approved on October 17, 2023 by the members of the* ***Examination Committee****.*

Examination Committee:

Research supervisor : Theodossis Trypiniotis Assistant Prof._____

Committee member : Spiros Skourtis Associate Prof._____

Committee member : Grigorios Itskos Associate Prof._____

Committee member : Anastasios J. Tasiopoulos Prof._____

Committee member : Yossi Paltiel Prof. _____

DECLARATION OF DOCTORAL CANDIDATE

The present doctoral dissertation was submitted in partial fulfilment of the requirements for the degree of Doctor of Philosophy of the University of Cyprus. It is a product of original work of my own, unless otherwise mentioned through references, notes, or any other statements.

Constantinos Nicolaides

_____

Περίληψη

Η παρούσα διατριβή ασχολείται με τη διερεύνηση των φυσικών διεργασιών του σπιν ρεύματος σε solution-processed υλικά μέσω της μεθόδου spin pumping και αποτελείται από τρεις ανεξάρτητες μελέτες.

Προκειμένου να κατανοήσουμε το σύνθετο θέμα των ιδιοτήτων μεταφοράς σπιν σε αγώγιμα πολυμερή, παρουσιάζουμε μια συστηματική μελέτη της μεταφοράς σπιν στο PEDOT:PSS, ένα κοινό solution-processed οργανικό υλικό, σε διαφορετικά χημικά καθορισμένα επίπεδα doping. Οι κυριότερες παράμετροι που ελέγχουν τις σπιν ιδιότητες του PEDOT:PSS υπολογίστηκαν ξεχωριστά και έδειξαν ότι η διακύμανση των σπιν ιδιοτήτων σε διαφορετικά επίπεδα doping μπορεί να αποδοθεί στην αλλαγή ισχύος της σύζευξης ιδιοστροφορμής-τροχιακής στροφορμής (spin-orbit coupling), που προκαλείται από την αλλαγή της δομικής διαμόρφωσης του πολυμερούς. Αυτό το αποτέλεσμα αναμένεται να έχει ευρύτερες δυνατότητες εφαρμογής σε άλλα συστήματα πολυμερών υλικών.

Στη δεύτερη μελέτη, διερευνούμε τη δυνατότητα μιας solution-processed οργανικής ρίζας να λειτουργήσει ως εκπομπός σπιν με σκοπό να αντικαταστήσει τους κοινούς μεταλλικούς σιδηρομαγνήτες στις spintronic συσκευές. Αναφέρουμε την κατασκευή μιας σταθερής διεπιφάνειας τύπου-Blatter ρίζας/Permalloy και πραγματοποιούμε ταυτόχρονες μετρήσεις συντονισμού ηλεκτρονικού-σπιν και σιδηρομαγνητικού συντονισμού. Η εκπομπή σπιν ρεύματος από τη ρίζα επιβεβαιώθηκε μέσω του αυξημένου εύρους του φάσματος απορρόφησης της ρίζας. Αυτή η αύξηση εξαφανίζεται όταν θέτουμε προσεκτικά τους δύο συντονισμούς ώστε να συμπίπτουν, δείχνοντας ότι η αύξηση του εύρους του φάσματος της ρίζας μπορεί να ανατραπεί λόγω της εκπομπής σπιν ρεύματος από το σιδηρομαγνητικό στρώμα, ακυρώνοντας αποτελεσματικά την εκπομπή σπιν ρεύματος από τη ρίζα. Αυτή η μελέτη, από όσο

γνωρίζουμε, είναι η πρώτη στο είδος της και έχει τη δυνατότητα να συνδυάσει διαφορετικούς ερευνητικούς τομείς και να προκύψει ένα νέο ερευνητικό θέμα.

Τέλος, εξετάζουμε την επίδραση της μορφολογίας ενός σιδηρομαγνητικού στρώματος, το οποίο αναπτύσσεται πάνω σε solution-processed οργανικό-ανόργανο υβριδικό περοβσκίτη, στη spin pumping μέθοδο. Παρασκευάστηκε μια σειρά ετεροδομών $CH_3NH_3PbI_{3-x}Cl_x/NiFe$ με διαφορετικά πάχη $NiFe$ όπου παρατηρούμε εξέλιξη της μορφολογίας του σιδηρομαγνητικού υλικού αρχικά από την ανάπτυξη τρισδιάστατων δομών να καταλήγει σε ένα συνεχές λεπτό υμένιο. Αυτή η εξέλιξη της μορφολογίας φαίνεται να επηρεάζει την ικανότητα μεταφοράς σπιν στο $CH_3NH_3PbI_{3-x}Cl_x$ στρώμα που αποτυπώνεται σαν απότομη αύξηση του spin mixing conductance της διεπαφής. Τα αποτελέσματά μας έχουν ευρύτερες συνέπειες όσον αφορά την αποδοτικότητα εισαγωγής σπιν ρεύματος σε περοβσκίτες και γενικότερα σε solution-processed υμένια.

Abstract

This dissertation deals with the investigation of the physics of spin current in solution-processed materials via the spin pumping method and consists of three independent studies.

In order to shed light on the puzzling topic of the spin transport properties in conducting polymers, we report a systematic study of spin transport in PEDOT:PSS, a typical solution-processed organic material, at different chemically defined doping levels. The key parameters governing the spin properties of PEDOT:PSS are estimated separately and reveal that the variation of the spin properties at different doping level can be attributed to the change of the spin orbit coupling strength, induced by alteration of the structural conformation in the polymer. The result has wider applicability in other polymer material systems.

In the second study, we investigate the possibility of a solution-processed organic radical operating as a spin emitter to replace common metal ferromagnets in spintronic devices. We report the fabrication of a stable Blatter-type radical/Permalloy bilayer and carry out simultaneous electron-spin and ferromagnetic resonance measurements. A signature of spin current emission from the radical is obtained through its increased linewidth. This increase is vanished when carefully tuning the two resonances to coincide, demonstrating that the radical linewidth increase can be reversibly reduced due to emission of a backward spin current from the ferromagnetic layer, effectively canceling the radical's emission. This study, to the best of our knowledge, is the first of its kind and has the potential to bring different research areas together, and opens up a new research topic.

Finally, we deal with the influence on the spin pumping process of the morphology of a ferromagnetic film grown onto a solution-processed organic-inorganic

hybrid perovskite. A series of $CH_3NH_3PbI_{3-x}Cl_x/NiFe$ heterostructures is prepared at various NiFe thicknesses and we observe an evolution of the morphology from island growth to continuous thin film. This evolution seems to affect the ability of spin transfer to the $CH_3NH_3PbI_{3-x}Cl_x$ layer observed as a sharp increase of the spin mixing conductance of the interface. Our results have wider implications for the efficiency of spin current injection in perovskites and generally in solution-processed films.

Acknowledgements

First and foremost, I would like to express my deepest appreciation and sincere gratitude to my research supervisor and mentor, Assistant Prof. Theodossis Trypiniotis, for giving me the opportunity to join the organic spintronic community and providing me the proper guidelines to evolve from a student to a researcher. I am very thankful for his great guidance, teaching me the way of scientific thinking, the fruitful endless discussions and the continuous support providing the strength to carry out the research.

I would like to warmly thank my Thesis committee members: Associate Prof. Spiros Skourtis, Associate Prof. Grigorios Itskos, Prof. Anastasios Tasiopoulos and Prof. Yossi Paltiel for honoring me with their acceptance to be part of my Thesis committee.

I would also like to thank our collaborators whose contribution was decisive for the completion of this research: Associate Prof. Sophia Charalambous-Hayes and Dr. Eliana Nicolaidou from the Department of Chemistry at the University of Cyprus for carrying out Resonance Raman measurements for the PEDOT:PSS samples, for the great cooperation and fruitful meetings, Prof. Panayiotis Koutentis' group from the Department of Chemistry at the University of Cyprus and Assistant Prof. Christos Constantinides' group from the Department of Natural Sciences at the University of Michigan-Dearborn for providing us the ideal and high quality Blatter radical derivative and Associate Prof. Grigorios Itskos' group for providing me access to their lab for photoluminescence measurements for the PEDOT:PSS samples.

Last, I am deeply grateful to my beloved family, my parents, my brother and sister and my wife for their unconditional love, their support in all possible ways and especially their patience and encouragement during my PhD study.

Στην οικογένειά μου

Contents

List of Abbreviations

α	Gilbert damping term
γ	Spin-admixture parameter
γ_e	Gyromagnetic ratio
ΔH	Linewidth of ferromagnetic resonance absorption
θ	Dihedral angle
θ_H	Out-of-plane magnetic field angle
θ_M	Out-of-plane magnetization angle
θ_{SHE}	Spin Hall angle
λ_N	Spin diffusion length
μ	Mobility
μ_B	Bohr magneton
μ_s	Spin magnetic moment
ξ	Polaron localization length
ϕ	In-plane magnetic field angle
χ_y	Microwave magnetic susceptibility
AFM	Atomic force microscopy
AHE	Anomalous Hall effect
D	Spin diffusion coefficient
DCM	Dichloromethane
DNP	Dynamic nuclear polarization
DMSO	Dimethyl sulfoxide
EBR	1-(2-ethoxyphenyl)-3-phelyl-1,4-dihydro-1,2,4-benzotriazin-4yl
ESR	Electron spin resonance
FA	Formamidinium
FM	Ferromagnet
FMR	Ferromagnetic resonance

GMR	Giant magnetoresistance
$g^{\uparrow\downarrow}$	Spin mixing conductance
H	External magnetic field
h	Microwave magnetic field
H_{an}	Magnetocrystalline anisotropy field
H_c	Coercivity
HFI	Hyperfine interaction
H_{FMR}	Ferromagnetic resonance magnetic field
H_M	Magnetostatic anisotropy field
h_{rf}	Radio-frequency magnetic field
$\hbar$	Planck constant
H_s	Surface magnetic field
I	Nuclear magnetic momentum
J_c	Charge current
J_s	Spin current
k_B	Boltzman constant
LLG	Landau-Lifshitz-Gilbert
MA	Methylammonium
MBE	Molecular Beam Epitaxy
MBR	1-(2-methoxyphenyl) Blatter radical
M_{eff}	Effective magnetization
MOKE	Magneto-optic Kerr effect
M_s	Saturation magnetization
m_s	Spin magnetic moment
n	Polaron concentration
NiFe	Permalloy
NM	Non-magnet
OIHP	Organic-inorganic hybrid perovskite
OSC	Organic semiconductor
PEDOT:PSS	Poly(3-4-ethylenedioxythiophene):polysterenesulfonate
PL	Photoluminescence
q	Magnon's wavevector
RR	Resonance Raman spectroscopy

SDL	Spin diffusion length
SHE	Spin Hall effect
STT-MRAM	Spin-transfer-torque magnetic-random-access-memory
SOC	Spin-orbit coupling
SOMO	Singly occupied molecular orbital
T_1	Spin relaxation time
T_2	Spin dephasing time
T_6	Sexithiophene
TMS	Two-magnon scattering
YIG	Yttrium Iron Garnet

List of Figures

List of Tables

Chapter 1

Introduction

The insatiable need of humanity for faster and smaller devices, leads the common electronic transistor currently used in conventional electronics to its limits, imposed by the laws of nature and fabrication techniques. In order to continue the evolution of technology, there is an urgent need to overcome such obstacles. Spintronics offers one of the most promising methods [4] towards this goal. By exploiting the internal angular momentum of the electron, which is called spin, for data transfer and processing, a significant energy saving in reduced time and high speed data processing is expected [5]. A further understanding of the behavior of the electronic spin in various materials and the creation of the necessary expertise in order to inject, manipulate and detect it, could lead to replacement of conventional electronics with spintronic based electronics.

The discovery of the giant magnetoresistance (GMR) mechanism [6, 7], which triggered an enormous revolution in information technology paving the way for some of today's most useful devices, marked a crucial milestone in spintronic progress. A series of spintronic-based memory applications followed in recent years [5], where one of its most representative cases is the spin-transfer-torque magnetic-random-access-memory (STT-MRAM) [8], a type of non-volatile memory that uses spin current to read data, still maintain the momentum in spintronics research. However, the development of spintronics is not limited to spin-related memory applications, since other subsections of spintronics, such as spin caloritronics [9], semiconductor spintronics [10], antiferromagnetic spintronics [11],

e.t.c. are in parallel progress, aiming to integrate spintronics with current technology and enabling unprecedented advances in many other aspects of technology.

Most research in spintronics to date, has predominantly focused on metals and inorganic semiconductors, since they are traditional materials whose properties had been extensively investigated, therefore it was easier to study and exploit their spin properties. However, the emerging field of solution-processed organic spintronics is developing rapidly over the past few years [12,13]. Solution-processed organic materials present unique electrical, optical and mechanical properties leading to a variety of applications in many technological sectors such as organic light emitting diodes [14], solar cells [15] and organic transistors [16, 17]. They also offer several advantages over their traditional inorganic ones, as they allow for flexibility and vast parameter space for tuning their properties by chemical synthesis and also for low cost production and ease of processing methods. Hence they have the potential to take spintronics in a level that inorganic materials cannot offer. In this context, this dissertation aims to study a series of basic phenomena related to spin physics in this material.

The main objective of the presented research, is to unravel the spin mechanisms that guide spin current propagation through solution-processed organic materials and across their interface with inorganic materials, and address some currently not well understood scientific questions in spintronics, opening opportunities for realizing novel spintronic devices for spin-based information processing. More specifically, this work studies spin current transmission through ferromagnet/solution-processed organic bilayers by using spin pumping under ferromagnetic resonance, as the main experimental technique. The work is supported by supplementary techniques that investigate magnetic, electric, structural and optical properties.

In this dissertation initially in Chapter 2 some of the most important concepts of the spintronics field are briefly outlined such as spin current, spin relaxation, spin-orbit coupling and spin-Hall effect. After that, in Chapter 3 a detailed phenomenological and theoretical description of ferromagnetic resonance is given together with a calculation of ferromagnetic resonance linewidth lineshape. The main mechanisms of intrinsic and extrinsic damping are then discussed in Chapter 4, by giving more emphasis on the spin pumping mechanism, which is the center for our

projects. Then, in Chapter 5, the fundamental principle of electron spin resonance is reported in brief, accompanied by selected topics that relate to this thesis. Chapter 6, is dedicated to briefly cover the experimental methods used to develop and characterize the spintronic devices described in this dissertation. Next, in Chapters 7-9, the three main projects that were carried out are presented with the topics "Effect of structural conformation of conjucated polymers on spin transport", "Metal-free organic radical spin source" and "Spin pumping across hybrid organic-inorganic perovskite/ferromagnet interface: the effect of ferromagnet morphology". Finally, the dissertation closes with concluding remarks in Chapter 10 of the presented projects and future work motivated by the research presented in this thesis.

Chapter 2

Spin Current

Spin current is a fundamental concept in the field of spintronics. In this chapter, the fundamentals of spin current are presented and compared with charge current, together with phenomena related to spin current like spin orbit coupling, spin relaxation and spin Hall effect.

2.1 The concept of spin current

Except of its mass and elementary charge, an electron has an intrinsic angular momentum, called spin. This is a quantum mechanical quantity and is expressed by the spin angular momentum operator [18]

$$\widehat{\overrightarrow{S}} = \frac{\hbar}{2}\overrightarrow{\sigma}, \tag{2.1}$$

where $\hbar$ is the Planck's constant and $\overrightarrow{\sigma}$ are the Pauli spin matrix.

$$\sigma_x = \begin{pmatrix} 0 & 1 \\ 1 & 0 \end{pmatrix}, \sigma_y = \begin{pmatrix} 0 & i \\ -i & 0 \end{pmatrix}, \sigma_z = \begin{pmatrix} 1 & 0 \\ 0 & -1 \end{pmatrix}. \tag{2.2}$$

There are only two eigenstates: $|\frac{1}{2}, \frac{1}{2}\rangle$, which is called spin up ($\uparrow$) and $|\frac{1}{2}, -\frac{1}{2}\rangle$ which is called spin down ($\downarrow$). By using them as base vectors, the general condition of an electronic spin can be expressed as a spinor:

$$|\Psi\rangle = \begin{pmatrix} a \\ b \end{pmatrix} = a|X_+\rangle + b|X_-\rangle \tag{2.3}$$

with

$$X_+ = \begin{pmatrix} 1 \\ 0 \end{pmatrix} X_- = \begin{pmatrix} 0 \\ 1 \end{pmatrix} \tag{2.4}$$

representing spin up and spin down and corresponding to the eigenvalues $+\frac{\hbar}{2}$ and $-\frac{\hbar}{2}$ respectively.

Directional and coherent motion of electron spin in materials of nanometric dimensions circulates a spin current [19]. In contrast with electric current, that is directional motion of electron charge, spin current is angular momentum flow, which is created through spin injection or spin accumulation and vanished by spin relaxation or spin diffusion [20].

In order to get an intuitive understanding of spin currents, we consider a simplified two-channel model system in which conduction electrons are charge carriers and there is no spin relaxation. Furthermore, in order to define spin current in analogous way to charge current we set $n_\uparrow$ and $n_\downarrow$, to denote the number of spin-up and spin-down electrons, respectively [21]. The charge density ρ_c and the spin density $\rho_{s,\hat{s}}$ can be defined as

$$\rho_c = \langle\Psi|Q|\Psi\rangle \quad , \quad \rho_{s,\hat{s}} = \hat{s}\langle\Psi|S|\Psi\rangle \tag{2.5}$$

where $Q = -e\mathbf{1}$ is the charge operator and S is the spin angular momentum operator (equation 2.1). By introducing Ψ from equations 2.3, 2.4 and $\hat{s} = (0, 0, 1)$ resulting in,

$$\rho_c = -e\langle\Psi|\Psi\rangle = -e(n_\uparrow + n_\downarrow) \quad , \quad \rho_{s,\hat{s}} = \frac{\hbar}{2}\langle\Psi|\sigma_z|\Psi\rangle = \frac{\hbar}{2}(n_\uparrow - n_\downarrow) \tag{2.6}$$

By multiplying charge density and spin density with the average electron velocity, charge current density and spin current density are given as $\overrightarrow{J_c} = \rho_c \overrightarrow{v}$ and $\overrightarrow{J_s} = \rho_{s,\hat{s}} \overrightarrow{v}$,respectively. Moreover, by setting $\overrightarrow{J_\uparrow} = en_\uparrow\overrightarrow{v_\uparrow}$ and $\overrightarrow{J_\downarrow} = en_\downarrow\overrightarrow{v_\downarrow}$ the charge current density and spin current density can be expressed as:

$$\overrightarrow{J_c} = -(\overrightarrow{J_\uparrow} + \overrightarrow{J_\downarrow}) \quad , \quad \overrightarrow{J_s} = \frac{\hbar}{2e}(\overrightarrow{J_\uparrow} - \overrightarrow{J_\downarrow}) \tag{2.7}$$

Therefore, by using equation (2.7) we can separate currents in three different categories [20]. If charge current density for spin-up and spin-down are equal ($\overrightarrow{J_\uparrow} = \overrightarrow{J_\downarrow}$), this corresponds to a net charge transfer without spin transfer and is referred to as a pure charge current (Figure 2.1.a). When the two charge current densities are unequal ($\overrightarrow{J_\uparrow} > \overrightarrow{J_\downarrow}$) or ($\overrightarrow{J_\uparrow} < \overrightarrow{J_\downarrow}$), then a spin polarized current appears where charge and

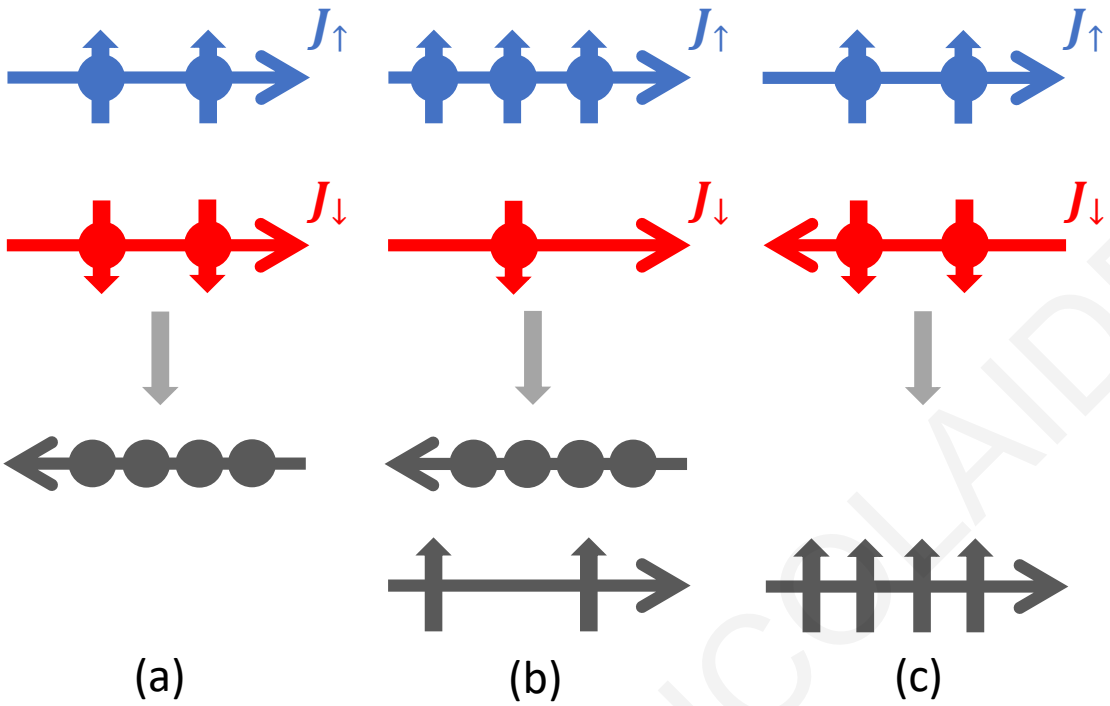

Figure 2.1: Illustration of (a) a pure charge current, (b) a spin-polarized current and (c) a pure spin current. Charge carriers are marked by spheres, while the direction of the spin is indicated by the arrows.

spin are transferred simultaneously (Figure 2.1.b). Finally, in the third case the two charge current densities have equal magnitude but propagate in opposite directions ($\overrightarrow{J_\uparrow} = -\overrightarrow{J_\downarrow}$). This results in a spin flow without the presence of charge current and is called pure spin current (Figure 2.1.c).

2.2 Spin Relaxation

The fact that non-equilibrium populations of spin, that is spin current, lives relatively long in some materials (typically of the order of tens of nanoseconds) allow spin-encoded information to travel macroscopic distances and makes spintronics a viable option for future technology breakthroughs [22]. Spin relaxation and spin dephasing are processes that lead to spin equilibration and is the central issue for all spin phenomena, so it is of great importance to understand the mechanisms governing them. In general, they can be understood as the result of the action of time dependent magnetic fields, which are not real but rather effective magnetic fields,

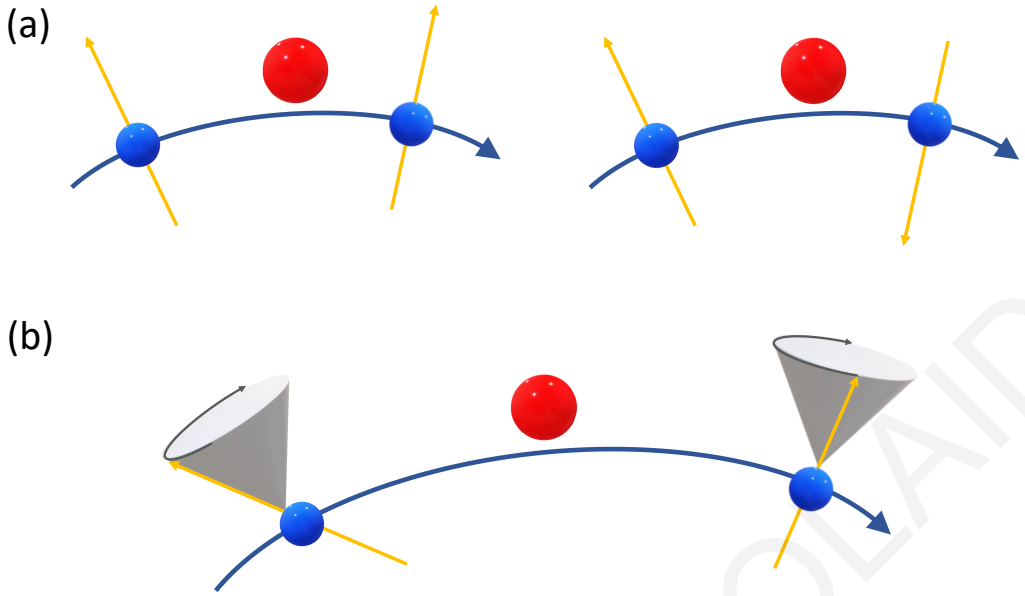

Figure 2.2: Schematic demonstration of (a) Elliott-Yafet and (b) Dyakonov-Perel spin relaxation mechanisms.

originating mainly from the spin-orbit coupling (SOC) combined with electron scattering due to impurities or lattice vibrations across different momentum states resulting in spin relaxation. The spins can also interact with intrinsic magnetic moments of the nuclei giving rise to an effective magnetic field from hyperfine interaction, while spin relaxation can also be caused by spin exchange and dipole interactions respectively.

SOC is a relativistic interaction which was first described by Dirac [23]. However, in order to understand its origin lets follow the classical approach. According to the classical interpretation of the SOC interaction if an observer moves with a velocity $\overrightarrow{u}$ in an external electric field $\overrightarrow{E}$, he will feel a magnetic field $\overrightarrow{B} = \frac{1}{c^2}\overrightarrow{E} \times \overrightarrow{u}$, where c is the velocity of light in vacuum. The electric field is related to the electric potential via $\overrightarrow{E} = -\overrightarrow{\nabla} V$ and the momentum is given by $\overrightarrow{p} = m_e \overrightarrow{u}$. If the observer is an electron the corresponding SOC effective magnetic field $B_{SOC} \sim \frac{1}{mc^2}\overrightarrow{\nabla} V \times \overrightarrow{p}$, originates from electron's motion under the influence of a nuclear potential. In turn, the magnetic field that the electron feels, interacts with its spin magnetic moment ($\overrightarrow{\mu_s}$) and tends to be aligned with it ($H_{SOC} \sim \overrightarrow{\mu_s} \cdot \overrightarrow{B_{SOC}}$). This is the physical origin of the SOC, the role of which strongly increases for heavy atoms [24] ($SOC \sim Z^4$).

There are several spin relaxation mechanisms. Most of them act at the same time in different systems, but in different materials and under different circumstances, one mechanism predominates over another [22], so it is necessary to study each material separately. Elliott-Yafet theory describes spin relaxation mainly in centrosymmetric crystals. In this type of crystals SOC arising from the lattice, providing an admixture of the spin-up and spin-down Bloch states [22] [25] [26], while momentum scattering is typically caused by impurities or lattice phonons. Combining SOC and momentum scattering, the spin-up and spin-down can couple resulting in a spin-flip. During scattering the direction and the magnitude of B_{SOC} depends on geometry of each collision separately. This field doesn't apply on electron for a certain amount of time, since it only exists during a collision and it is zero between collisions (Figure 2.2.a). For an ensemble of initially totally polarized spin electrons, after a number of scattering events the initial polarization is relaxed. Therefore, spin relaxation time due to the Elliott-Yafet mechanism is inversely analogous to the momentum scattering rate.

On the other hand, in lattices without inversion symmetry, SOC lifts the spin degeneracy. This splitting is equivalent to an effective magnetic field. As a result, the spin is depolarized by a series of random fractional rotations between collisions (Figure 2.2.b). When the momentum of the electron changes through scattering with a defect or a phonon, then precession starts again but along a different axis. These random fluctuations cause a net dephasing of the spin-polarization. This is the well known Dyakonov-Perel mechanism [27] and in contrast with Elliott-Yafet mechanism an enhanced rate of scattering events causes a weakened Dyakonov-Perel relaxation.

Another spin relaxation mechanism is hyperfine interaction, which is dominant in systems with weak SOC and where charge carriers are strongly localized in space and have no resultant momentum [28], the so-called quasi-static charge carriers. In this occasion, the spin relaxation is caused by the effective magnetic field [29] generated from the interaction between the electron and the nuclear spin.

The SOC and hyperfine interaction are considered to be the principal factors that cause spin relaxation also in organic semiconductors (OSCs) [28] [30]. As it has already been noted, the SOC strength is proportional to the fourth power of the atomic number, so the light-weight-element composition of OSCs (consisting mainly

of C, H, O) was expected to lead to a weak SOC strength. Indeed, extremely long spin relaxation time up to millisecond level has experimentally been measured [31]. However, not all organic materials follow this trend [32], with some materials like C_{60} [33] and Alq_3 [34] exhibiting surprisingly high SOC. The answer to this paradox was given by Yu's theoretical calculations [3,35] which reveal that the SOC strength in OSCs is not only related to the atomic number of materials but is also strongly affected by the molecular structure. This prediction subsequently was confirmed also experimentally [32,36]. An important difference between inorganic and organic semiconductors is that the charge transport for OSCs takes place via spatial charge transfer between donor-acceptor states driven by intra- and inter-molecular vibrations instead of momentum scattering between electronic states, resulting in different operation of Elliott-Yafet and Dyakonov-Perel mechanisms in OSCs. More specifically, in an OSC characterized by hopping charge transport, spatial scattering between mixed spin states works in direct analogy to Elliott-Yafet relaxation [37]. Spin mixing in these scattering states is usually weak allowing to treat the SOC operator ($\widehat{H}_{SOC}$) as a first order perturbative correction. The perturbation on the spin-carrying molecular orbital,$|\Psi_o \uparrow\rangle$, leads to the spin mixed eigenstates [3,35,37,38], $|\Psi_o+\rangle$,

$$|\Psi_o+\rangle = |\Psi_o \uparrow\rangle - \sum_{k\neq 0\sigma} \frac{\langle \Psi_k\sigma|\widehat{H}_{SOC}|\Psi_o \uparrow\rangle}{E_k - E_o}|\Psi_k\sigma\rangle \tag{2.8}$$

where $\widehat{H}_{SOC} = \sum_i \xi_i \overrightarrow{I_i} \cdot \overrightarrow{s_i}$. The spin-orbit constants ξ_i provide the nuclear Coulomb potential scaling of orbital angular momentum $\overrightarrow{I_i}$ relative to the atomic nuclei for electron i. Finally, the spin admixture (γ) can then be calculated as a change in the norm of equation 2.8 from the unperturbed state [3,35,37,38],

$$\langle \Psi_o + |\Psi_o+\rangle = \langle \Psi_o \uparrow |\Psi_o \uparrow\rangle + \gamma^2 = 1 + \gamma^2. \tag{2.9}$$

Therefore, γ^2 reflects the SOC strength, becoming a vital parameter and a central concept for current experimental [32, 36, 39–41] and theoretical [3, 35, 37, 38] organic spintronics. As has already been noted in organic solids, the spin admixture except of the chemical composition is also strongly influenced by the materials' structural conformation by altering the torsion angle between conjucated units. The relation between γ and the dihedral angle (θ) between two adjacent π orbitals is derived as [35,37]:

$$\gamma^2 = \gamma_o^2[1 + tan^2(\theta)] \tag{2.10}$$

where γ_o is the spin admixture of the planar structure. As θ approaches 90^o, and the π orbitals of the conjucated system are increasingly misaligned, γ^2 increases sharply. This structural conformational dependence of the SOC has been previously used to explain the abnormally large SOC in Alq_3 molecules despite its lack of heavy elements, due to the nearly orthogonal relationship between aromatic ligands in the molecule [32, 35].

SOC in organic materials is often very small, therefore SOC scattering frequency will be weakened. However, the presence of atoms with half-integer nuclear spins leads to random magnetic fields which can indirectly couple to the spins of the carbon π electrons through the exchange interaction of carbon s electrons [42, 43]. Therefore, an analogue of the Dyakonov-Perel mechanism in organics is driven by precession under the hyperfine fields instead of the spin-orbit fields [30]. The role of hyperfine interaction in spin transport was observed by Nguyen et al. [44] where they found a suppressed relaxation on deuteration of hydrogen atoms in DOO-PPV polymers.

Moreover, for organic materials the spin transport is also different compared to inorganic materials and this consequently affects the relaxation pathways. Two mechanisms have been proposed for spin transport, mediated by spin-orbit coupled carrier hopping [45, 46] and mediated by exchange coupling between localized carriers [39,47,48]. The latter is facilitated via a high carrier density where the average distance between polarons is reduced. Exchange interactions cause two neighboring spins to exchange their polarity. As a consequence, the overall polarization is conserved under exchange and contributes to spin transport. Exchange interactions depend on carrier density and the extent of delocalization of the spin on the molecule and tend to cause efficient spin transport [2]. Conclusively, both spin transport mechanisms could be present in an OSC and they should be taken into account.

2.3 Spin Hall effect

As a consequence of the microscopic scattering processes discussed in the previous section, two phenomena manifest themselves macroscopically, the anomalous Hall effect (AHE) and spin Hall effect (SHE). Spin Hall effect is maybe the most important discovery of recent years in the field of spintronics since it connects directly

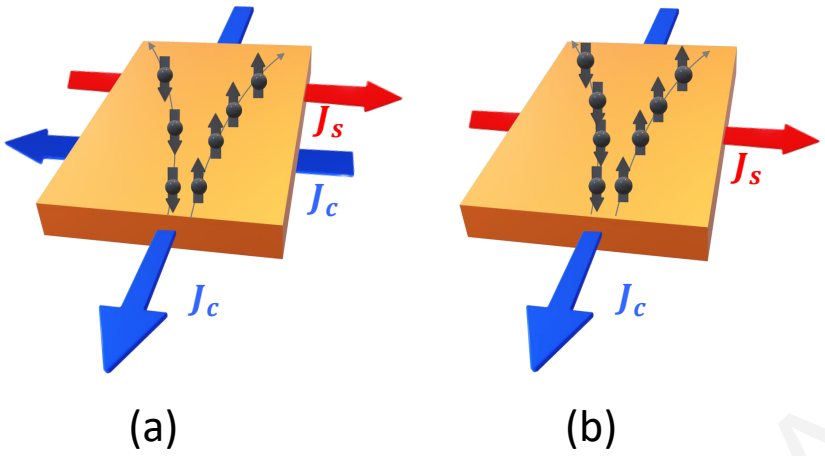

Figure 2.3: Schematic demonstration of (a) Anomalous Hall effect (AHE) and (b) Spin Hall effect(SHE)

charge current with spin current, thus providing the means for injection and detection of spin current. It is a generalization of the anomalous Hall effect (AHE) [49] which is observed in ferromagnets and originates from the spin orbit interaction. A ferromagnet is characterized by its remnant magnetization in zero external magnetic field. If magnetization has up direction usually the majority of free electrons are spin-up, and minority are spin-down, that is anti-parallel to magnetization vector. By applying an external electric field in a ferromagnet a spin polarized current can be created due to the imbalance of the spin populations. Spin-orbit coupling causes an asymmetric scattering on free electrons with respect to their spin. As a result, there is a greater probability spin-up electrons scatter in a direction transverse to their initial motion, while spin-down electrons are more likely to scatter at the opposite direction. Therefore, since the number of electrons with spin-up and spin down is not equal, an electromotive voltage is created in the direction perpendicular to the charge current(Figure 2.3.a). In contrast, SHE is observed in non-polarized systems like non-magnetic materials or semiconductors where the number of spin-up free electrons is equal with spin-down. By applying an external electric field in materials with high spin-orbit coupling, for example Pt and Pd, a spin-up free electron in the presence of impurity or boundary scatters preferentially in a certain transverse direction to the applied electric field, while a spin-down electron scatters at the opposite direction. As a result, SHE converts a charge current ($\overrightarrow{J_C}$) into a pure spin current ($\overrightarrow{J_S}$) via the spin-orbit interaction (Figure 2.3.b). The effect had been predicted by Dyakonov and

Perel in 1971 [50], rediscovered by Hirsch in 1999 [51] and was first observed experimentally by Kato et al in 2004 [52]. The relation among $\overrightarrow{J_S}$, $\overrightarrow{J_C}$ and the spin polarization vector ($\overrightarrow{\sigma}$) is given by [53]:

$$\overrightarrow{J_S} = \frac{\hbar}{2e}\theta_{SH}[\overrightarrow{J_C} \times \overrightarrow{\sigma}] \tag{2.11}$$

where θ_{SH}, corresponds to the spin Hall angle which quantifies the spin-charge conversion efficiency in the non-magnetic material. In the reverse process, the inverse spin Hall effect (ISHE), two electrons with opposite spin moving in opposite directions are scattered in the same direction, converting spin current into charge current.

Chapter 3

Ferromagnetic Resonance

Ferromagnetic resonance (FMR) is one of the most powerful experimental techniques for studying ultrathin film magnetic properties. By using this method, all the basic parameters which describe the magnetic properties of these materials can be measured such as magnetic anisotropy and magnetization relaxation mechanisms. The most important advantages of this experimental technique are the high sensitivity, since the FMR signal of $10^{10} - 10^{14}$ ferromagnetically ordered magnetic moments can be measured [54] and high resolution, since shifts in the resonance fields of a few Oersted are easily detected. Furthermore, there is a huge body of literature for the interpretation of resonance spectra and easy set-up, since all equipment is standard and readily available. At the following sections, firstly a phenomenological description of ferromagnetic resonance is given. Then, there is a brief introduction for magnetic anisotropy which is followed by a theoretical description of FMR condition and a calculation of FMR lineshape.

3.1 Phenomenological description of Ferromagnetic Resonance

Magnetic films whose thickness is of the order of ten nanometers are referred to as ultrathin. In ultrathin magnetic films with high exchange strength in saturated conditions the macrospin approximation can be used where all spins are assumed to

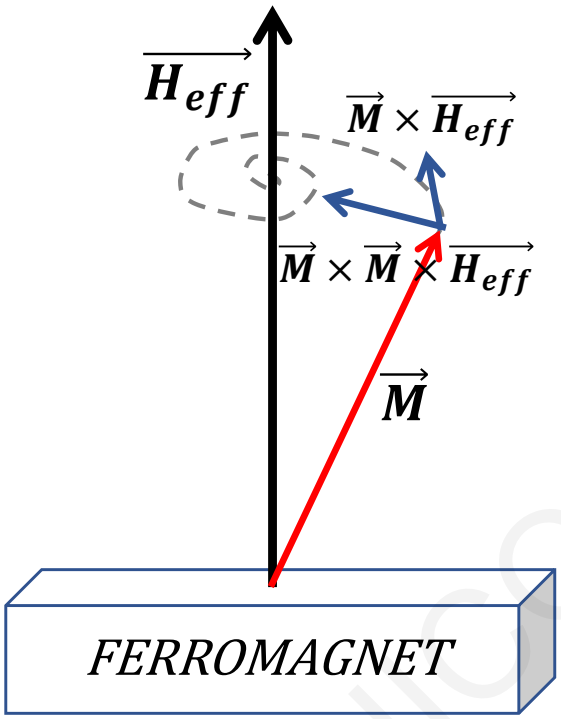

Figure 3.1: Schematic illustration of Landau-Lifhitz-Gilbert equation

precess with the same amplitude and phase. This approximation assumes that the magnitude of magnetization vector of a magnetic film is spatially uniform during its precession as a single macroscopic spin. Since there is no spatial variation of its magnitude, the investigation of magnetization vector motion is much more accessible.

In a ferromagnet whose magnetization vector space (macrospin), points in a random direction, by applying an external magnetic field the magnetization will start precessing around the effective magnetic field and simultaneously the angle between the magnetization and the effective magnetic field vectors will be decreasing slowly. The effective magnetic field corresponds to the vector sum of external magnetic field ($\overrightarrow{H}$), the magnetocrystalline anisotropy field ($\overrightarrow{H_{an}}$) and the magnetostatic anisotropy field ($\overrightarrow{H_M}$).

$$\overrightarrow{H_{eff}} = \overrightarrow{H} + \overrightarrow{H_{an}} + \overrightarrow{H_M} \tag{3.1}$$

Eventually, the magnetization vector is aligned with the external magnetic field and this is the lowest energy position of the system. The motion of the magnetization

vector (Figure 3.1) is given by the Landau-Lifhitz-Gilbert equation [55], [56].

$$\frac{d\overrightarrow{M}}{dt} = -\gamma_e \overrightarrow{M} \times \overrightarrow{H_{eff}} + \frac{\alpha_o}{M_s} \overrightarrow{M} \times (\overrightarrow{M} \times \overrightarrow{H_{eff}}) \tag{3.2}$$

The first part corresponds to the precession of the vector and the second is the damping term. In order to stop the descending motion of the magnetization, an alternating magnetic field is applied perpendicular to the external magnetic field. If its frequency is equal to the precession natural frequency the resonance condition is fulfilled and the magnetization precesses at maximum angle. This is called ferromagnetic resonance (FMR). The usual way to produce this alternating magnetic field is through microwave irradiation with the appropriate frequency. In order to set the ferromagnetic system in resonance, a frequency of the order of some Gigahertz is most often used.

3.2 Magnetic anisotropy

The magnetization in a ferromagnetic material is frequently not aligned in an arbitrary direction. It is not energetically equivalent to set the magnetization vector in any direction, so magnetization tends to align in certain energetically favorable directions, termed easy axes. The magnetic anisotropy of a ferromagnetic material depends mainly on two factors, the crystal structure of the ferromagnet, namely magnetocrystalline anisotropy and the shape of the material, which is called magnetostatic anisotropy or shape anisotropy [57].

In order to explain how a ferromagnet's shape affects the magnetic anisotropy, we have to understand first of all the concept of demagnetization field. A qualitative explanation will be given here by using the simplest example of a ferromagnetic ellipsoid. By applying an appropriate external magnetic field strength, a uniform magnetization can be created in a direction parallel to the external magnetic field. As a result, surface magnetic poles (or charges) appear, which in turn create a demagnetization field antiparallel with magnetization vector. The intensity of demagnetization field is proportional to the density of surface magnetic poles and inversely proportional with the distance between the surfaces. Therefore, the demagnetization field is stronger along the short axis of an ellipsoid rather than parallel to the long axis (Figure 3.2.a). Specifically, for a homogeneously magnetized

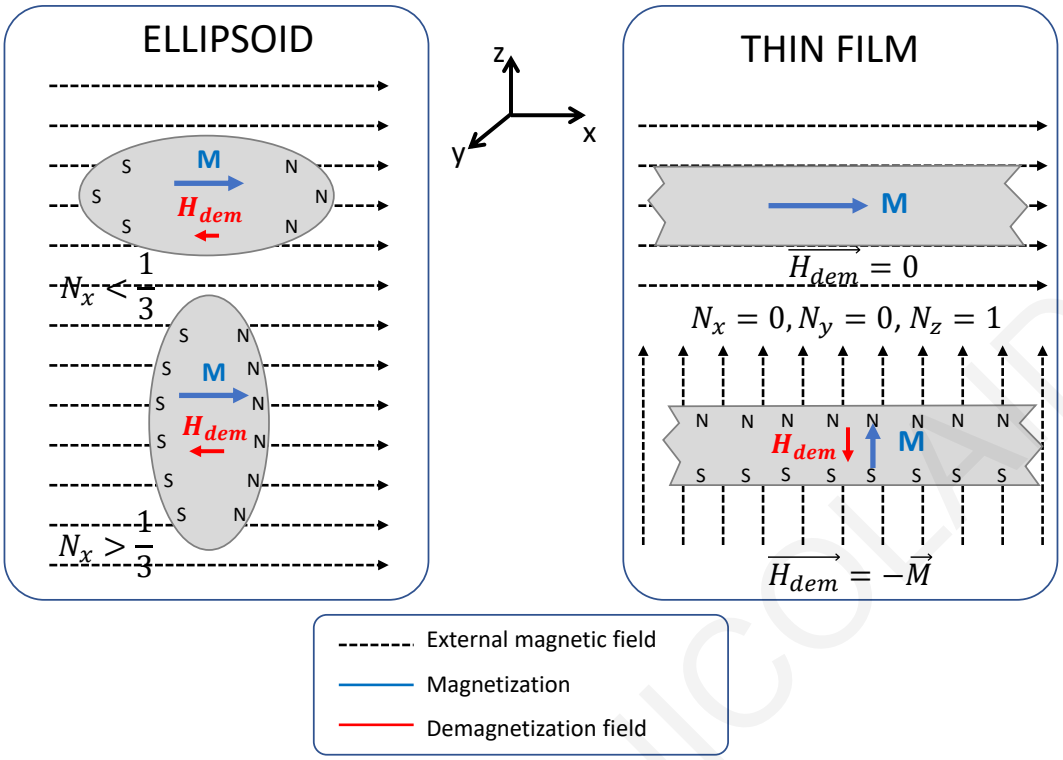

Figure 3.2: Schematic representation of shape anisotropy of (a) an ellipsoid, (b)a thin film

ellipsoid, the demagnetization field is given by [57],

$$\overrightarrow{H_{dem}} = -\hat{N} \cdot \vec{M} \tag{3.3}$$

where the dimensionless $\hat{N}$ tensor can be diagonalized, when magnetization vector is aligned with one of the basic axis of the ellipsoid $\hat{x}, \hat{y}, \hat{z}$. Moreover, the sum of diagonal elements of the $\hat{N}$ tensor has to fulfil the condition $N_x + N_y + N_z = 1$ and for the case of a sphere $N_x = N_y = N_z = \frac{1}{3}$. For an ellipsoid, if the direction of magnetization field is aligned along $\hat{x}$ axis, as well as ellipsoid's long axis $N_x < \frac{1}{3}$, while when it is aligned along the short axis $N_x > \frac{1}{3}$. Correspondingly, we can generalize the case of ellipsoid to calculate the demagnetization field in ultrathin films. In this case, we can suppose that $\hat{x}$ and $\hat{y}$ dimensions tend to infinity, while $\hat{z}$ dimension is finite. Then, the elements of demagnetization tensor N_x and N_y are zero and $N_z = 1$. As a result, if the external magnetic field is parallel to the film plane then demagnetization field doesn't exist and this case corresponds to the easy axis. When the external magnetic field is perpendicular to the film plane, then the maximum demagnetizating field is obtained equal with $\overrightarrow{H_d} = -\overrightarrow{M}$ and this is thin film's hard axis. (Figure 3.2.b).

Magnetocrystalline anisotropy originates from the interaction between electronic spin and neighbouring atoms in a ferromagnet (spin-orbit coupling). The ferromagnet's crystal structure symmetry affects the magnetocrystalline anisotropy, resulting in different energetically favourable directions inside the ferromagnet (easy axes). The simplest form of magnetic anisotropy is uniaxial anisotropy, when there is only a single easy axis. The uniaxial anisotropy energy density is given by $\varepsilon_u \propto K_u sin^2\theta$ where K_u is called the uniaxial magnetocrystalline anisotropy constant and θ is the angle between x-y plane and magnetization vector. Another important form of magnetocrystalline anisotropy is the cubic anisotropy. This corresponds to an anisotropy with three vertical easy axes and an energy density analogous to $\varepsilon_c \propto K_c sin^4\theta$ where K_c is the cubic magnetocrystalline constant.

3.3 Theoretical description of ferromagnetic resonance condition

By taking into consideration all the previous, we can calculate the ferromagnetic resonance condition for each ferromagnetic material case. There are two ways to achieve this. The first is by solving the Landau-Lifhitz-Gilbert equation by setting as a solution the appropriate ansatz [58], [59], [60] while the second is by determining the second derivative of the free energy with respect to the spherical angles of the magnetization [61], [62]:

$$\left(\frac{\omega}{\gamma}\right)^2 = \frac{1}{M^2 sin^2\theta_M}\left[\frac{\partial^2\epsilon}{\partial\theta_M^2}\frac{\partial^2\epsilon}{\partial\phi^2} - \left(\frac{\partial^2\epsilon}{\partial\phi\partial\theta_M}\right)\right] \tag{3.4}$$

In what follows, both of them will be used in order to find the ferromagnetic resonance condition for a uniform magnetized ultrathin magnetic film (i.e. NiFe) for an in-plane and out of plane orientation respectively.

If external bias magnetic field $\overrightarrow{H_o}$ is applied in plane along z-axis, then the magnetization vector is aligned in the same direction, while the driving radio frequency magnetic field $h_{rf}(t)$ is applied perpendicularly in the out of plane direction (figure 3.3). By assuming that the precession angle is small, then magnetization in the z-direction remains constant in time, equal with Ms. Consequently the time dependent vector of

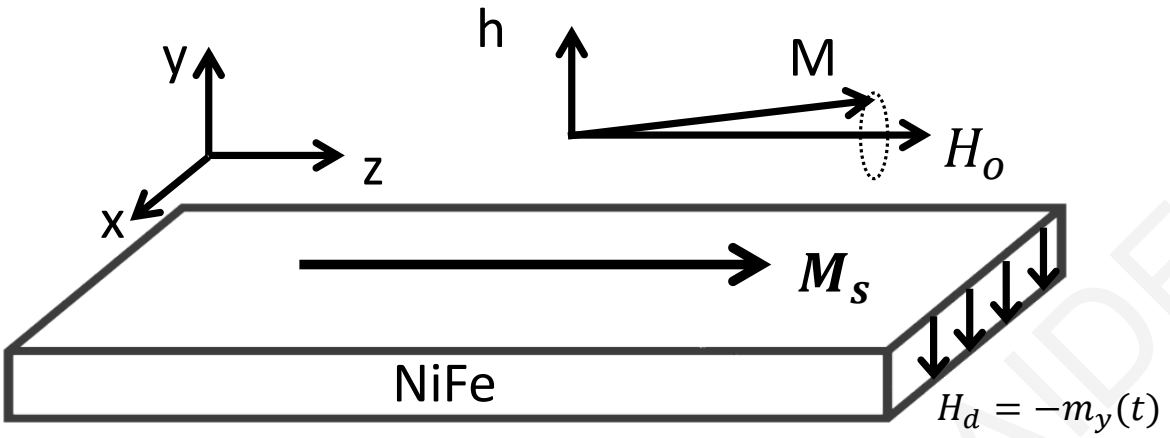

Figure 3.3: Schematic illustration of magnetization precession in a NiFe thin film. The demagnetizing field H_d exists only in the y direction and opposes m_y magnetization.

magnetization is expressed as:

$$\overrightarrow{M(t)} = \begin{pmatrix} m_x(t) \\ m_y(t) \\ Ms \end{pmatrix} \tag{3.5}$$

Since NiFe does not have magnetocrystalline anisotropy, then the only anisotropic field applied to the system is demagnetization field, which appears to the y direction due to the precessing magnetization vector. Then, by summing up external and alternating magnetic field and demagnetization field, the effective magnetic field appears to be equal with

$$\overrightarrow{H_{eff}}(t) = \begin{pmatrix} 0 \\ h_{rf}(t) - m_y(t) \\ H_o \end{pmatrix} \tag{3.6}$$

It is convenient to solve the LLG equation in terms of complex amplitudes. For those we assume the circular polarization of the driving radio frequency field $h_{rf}(t) = h_o e^{i\omega t}$ and the ansatz solution for the LLG equation (3.2) will be $m_{x,y}(t) = m_{x,y}(t)e^{i\omega t}$ resulting in:

$$\begin{pmatrix} \frac{d}{dt}m_x e^{i\omega t} \\ \frac{d}{dt}m_y e^{i\omega t} \\ 0 \end{pmatrix} = -\gamma \begin{pmatrix} 0 \\ h_{rf}e^{i\omega t} - m_y e^{i\omega t} \\ H_o \end{pmatrix} \times \begin{pmatrix} m_x e^{i\omega t} \\ m_y e^{i\omega t} \\ M_s \end{pmatrix} + \frac{\alpha_o}{M_s} \begin{pmatrix} m_x e^{i\omega t} \\ m_y e^{i\omega t} \\ M_s \end{pmatrix} \times \begin{pmatrix} \frac{d}{dt}m_x e^{i\omega t} \\ \frac{d}{dt}m_y e^{i\omega t} \\ 0 \end{pmatrix} \tag{3.7}$$

Afterwards, the cross product calculations are carried out leading to the following

system of algebraic linear equations:

$$i\omega m_x = -\gamma(H_o + M_s)m_y + \gamma M_s h_{rf} - i\alpha_o \omega m_y \tag{3.8}$$

$$i\omega m_y = \gamma H_o m_x + i\alpha_o \omega m_x \tag{3.9}$$

Finally, by ignoring the damping term and by finding the eigenvalue of ω the in-plane ferromagnetic resonance condition is given as:

$$\frac{\omega}{\gamma} = \sqrt{H_o(H_o + M_s)} \tag{3.10}$$

which is the famous Kittel's equation.

In order to extract the ferromagnetic resonance condition for the general out of plane case, the second way will be used. The free energy density for an ultrathin uniformly magnetized film includes the following terms:

$$\epsilon = -\overrightarrow{M} \cdot \overrightarrow{H} + 2\pi M_s^2 cos^2\theta_M + K_s sin^2\theta_M \tag{3.11}$$

Here, θ_M is the angle of the magnetization vector in spherical coordinates with respect to the film normal. The first term is the Zeemann energy, the second is the demagnetization energy, while the third term corresponds to the axial anisotropy energy. The out of plane ferromagnetic resonance condition is obtained by using equations 3.4 and 3.11.

$$\left(\frac{\omega}{\gamma}\right)^2 = [H_{FMR}cos(\theta_H - \theta_M) - 4\pi M_{eff} cos2\theta_M] \times [H_{FMR}cos(\theta_H - \theta_M) - 4\pi M_{eff} cos^2\theta_M] \tag{3.12}$$

where $4\pi M_{eff} = 4\pi M_s - \frac{2K_s}{M_s}$ and θ_H is the angle of external magnetic field with respect to the film normal.

3.4 Calculation of FMR lineshape

In this subsection FMR lineshape will be examined. The lineshape of the absorption curve is theoretically analogous to the imaginary part of the microwave magnetic susceptibility [59]. Microwave magnetic susceptibility (χ_y) is defined as the quotient of the magnetization component induced parallel to the microwave irradiation direction and the microwave alternating magnetic field [59]. By using equations 3.8 &

3.9 one obtains,

$$\chi_y \equiv \frac{m_y}{h_{rf}} = \frac{M_s(H_o + \frac{i\omega\alpha}{\gamma})}{((H_o + M_s) + \frac{i\omega\alpha}{\gamma})(H_o + \frac{i\omega\alpha}{\gamma}) - \frac{\omega^2}{\gamma^2}} \tag{3.13}$$

Then by setting the external magnetic field equal with the ferromagnetic resonance field plus the difference between external magnetic field and ferromagnetic resonance field ($H_o = H_{FMR} + \delta H$), neglecting the terms which are not analogous to ($\delta H + \frac{i\omega\alpha}{\gamma}$) and finally by multiplying and dividing with the complex conjugate, the imaginary part of microwave magnetic susceptibility can be expressed as,

$$Im\chi_y = \frac{M_s H_{FMR}}{H_{FMR}(H_{FMR} + M_s)} \frac{\frac{\omega\alpha}{\gamma}}{\delta H^2 + (\frac{\omega\alpha}{\gamma})^2}. \tag{3.14}$$

The Lorentzian function is given by

$$L(x) = A\frac{\Delta H_{HWHM}}{(x - x_o)^2 + (\Delta H_{HWHM})^2} \tag{3.15}$$

where A corresponds to the amplitude of Lorentzian curve and ΔH_{HWHM} is the half width at half maximum. Hence, by comparing the equations 3.14 & 3.15 we conclude that the expected FMR lineshape corresponds to the Lorentzian distribution with

$$A = \frac{M_s H_{FMR}}{H_{FMR}(H_{FMR} + M_s)} \ and \ \Delta_{HWHM} = \frac{\omega\alpha}{\gamma} \tag{3.16}$$

Chapter 4

Magnetic damping in thin ferromagnetics layers

As already mentioned above the tilting of the magnetization vector towards the equilibrium direction is given by the second part of LLG equation (eq.3.2), while the efficiency of that motion is determined by the magnetic damping parameter, which is in general sample dependent. The magnetization relaxation process is induced by a variety of factors, like the interaction with magnons, phonons, itinerant electrons, structural defects or sample impurities. Some damping mechanisms are inevitable and these are referred to as intrinsic, while interactions which are not inherent to the material are called extrinsic damping mechanisms.

4.1 Intrinsic damping mechanisms

The main representatives of intrinsic damping relaxation processes are itinerant electron-magnon interaction, magnon-phonon and eddy current mechanisms. In the following subsections they will be briefly examined with respect to their relevance to thin ferromagnetic layers.

4.1.1 Magnon-itinerant electron interaction mechanism

The most important intrinsic damping mechanism is based on the interaction between s-p like itinerant electrons with localized d-electron spins (magnon). There are two types of magnon-itinerant electron scattering, one involves spin-flips and the other involves no spin-flips but is associated with Fermi surface breathing.

The first model is introduced by Heinrich and he proposed that the s-d exchange interaction can be obtained by integrating the s-d exchange energy density functional [63, 64]

$$H_{sd} = \sum_j \int_V J(\overrightarrow{r}_j - \overrightarrow{r}) \overrightarrow{S_{j,d}} \cdot \overrightarrow{s_s}(\overrightarrow{r}) dr^3 \tag{4.1}$$

where $J(\overrightarrow{r} - \overrightarrow{r}')$ is the s-d exchange interaction between the spin density $\overrightarrow{s_s}$ of s-p like itinerant electrons and the localized spins of d-electrons $\overrightarrow{S_{j,d}}$, and j is the lattice site. The particle representation of the s-d exchange interaction Hamiltonian for the rf components of the magnetization is given by three particle collision terms [64].

$$H_{sd} = \sqrt{\frac{2S}{N}} \sum_k J(q) a_{k,\uparrow} a^+_{k+q,\downarrow} b_q + (h.c.) \tag{4.2}$$

where S is the spin, N is the number of atomic sites, a and a^+ respectively annihilate and create electrons and b and b^+ annihilate and create magnons. The $\uparrow$ and $\downarrow$ signs in the subscripts correspond to majority and minority spin electrons, respectively. Itinerant electrons and magnons are coherently scattered by the s-d exchange interaction resulting in the creation and annihilation of electron-hole pairs. Due to conservation of the angular momentum, the itinerant electron has to flip its spin when it is scattered by magnons. Nevertheless this scattering does not lead to magnetic damping for uniform mode magnons ($q \sim 0$). The s-d exchange interaction on its own only leads to a renormalized spectroscopic splitting factor, γ [63]. The coherent scattering of magnons with itinerant electrons has to be disrupted by incoherent scattering with thermally excited phonons or magnons. That results in a fast fluctuating torque resulting in magnetic relaxation. Finally the expression of the s-d interaction damping is given by [64]:

$$\alpha_{s-d} = \frac{\mu_B^2 N(E_F)}{M_s \gamma} \frac{1}{\tau_{sf}} \tag{4.3}$$

where $N(E_F)$ is the density of states at Fermi level and τ_{sf} corresponds to the spin-flip time of electron-hole pair. Therefore a reduced spin-flip time leads to a more

efficient magnetic relaxation. Someone can approach this process in a classical way. The s-d exchange interaction can be viewed as two precessing magnetic moments corresponding to the d-localized and itinerant electrons which are mutually coupled by the s-d exchange field. In the absence of damping the FMR excitation corresponds to a parallel alignment of the magnetic moments precessing together in phase. However, due to a finite spin free path of the itinerant electrons, the equation of motion for itinerant electrons has to include spin relaxation towards the instantaneous effective field. That results in a phase lag between the two precessing magnetic moments and consequently in magnetic damping.

Kambersky showed that the intrinsic damping in ferromagnets can be treated more generally by using the spin-orbit interaction [65–67]. As a consequence of spin-orbit coupling the energies of the Bloch states depend on the direction of magnetization. Hence, as the magnetization precess, the spin-orbit interaction changes the energy of the electronic states, pushing some occupied states above the Fermi level and unoccupied states below the Fermi level resulting in a generation of electron-hole pairs near the Fermi level. This is often referred to as a breathing Fermi surface. The effort of the electrons to repopulate the changing Fermi surface is delayed by a finite relaxation time of the electrons and this results in a phase lag between the Fermi surface distortions and the precessing magnetization. The phase lag for the breathing Fermi surface and the s-d exchange interaction is proportional to the microwave frequency ω. Clearly, in both cases one gets a typical situation for 'friction' like damping which is described in magnetism by the Gilbert relaxation term.

4.1.2 Phonon scattering mechanism

The second process of intrinsic damping is caused by magnon-phonon coupling. This mechanism describes the uniform precession mode (magnon with $q = 0$) degradation by scattering of those magnons with phonons (lattice vibration modes) resulting in spin decoherence and eventually causing damping of magnetization. This phenomenon is called phonon-drag [68]. Experiments have shown that although the phonon scattering mechanism occurs in most magnetic materials it is relative weak in comparison with the itinerant electron

mechanisms [64].

4.1.3 Eddy current mechanism

Another source of intrinsic damping can arise from eddy currents in the case of metallic ferromagnetic films. When a conductive material experiences a time-varying magnetic field, eddy currents are generated in the conductor [69]. Accordingly, in ferromagnetic materials under resonance conditions the interaction between the conduction electrons and the microwave excitation field can induce eddy currents resulting in an effective field which can cause damping of magnetization. Eddy current damping, α_{eddy}, is proportional to [70]:

$$\alpha_{eddy} \propto \gamma_e M_s \sigma t_{FM}^2 \tag{4.4}$$

where σ is the electrical conductivity and t_{FM} is the ferromagnetic film thickness. This mechanism is highly dependent on the material and becomes important for thick films ($\alpha_{eff} \propto t_{FM}^2$). The metallic ferromagnetic material that we are focusing on in this thesis is permalloy, where damping due to Eddy currents only need to be taken into account when the thickness surpasses 100nm [64]. Hence, in our case, the Eddy current mechanism contributes only a very small proportion of the total damping.

4.2 Extrinsic damping mechanisms

Until now, we have been examined relaxation processes that refer to phenomena due to intrinsic structural characteristics of magnetic crystals. These processes correspond to the magnetic relaxation of a perfect magnetic crystal. However, the presence of defects in the crystal, interface roughness, boundary grains and inhomogeneities can induce enhancement of magnetic relaxation or spectral width broadening. The main representatives of these non-Gilbert damping processes are two-magnon scattering and inhomogeneity.

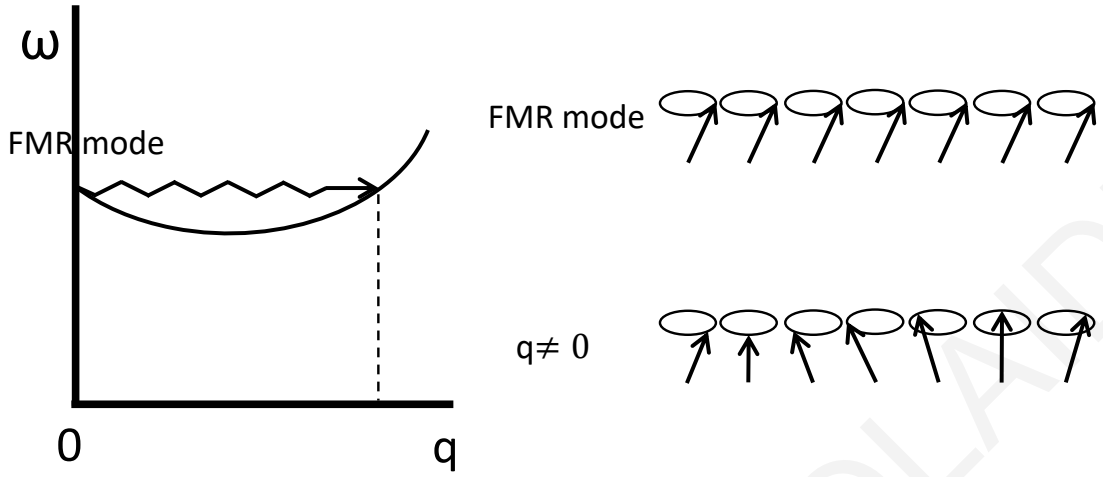

Figure 4.1: Graphical representation of the two-magnon scattering process from a uniform mode $q \sim 0$ to a mode degenerate with wavevector $q \neq 0$.

4.2.1 Two-magnon scattering

Two-magnon scattering (TMS) appears on magnetic systems characterized by strong exchange and dipolar interactions [71]. According to this process bulk or interface defects and imperfections on the surface of magnetic film can act as scattering centers and scatter uniform magnetization precession ($q \sim 0$ where q corresponds to the magnon's wavevector) into $q \neq 0$ magnons. Due to energy conservation the resonant mode ($q \sim 0$) can only scatter into spin waves oscillating at the same frequency i.e. $\omega(0) = \omega(q)$. Furthermore, due to the loss of translation invariance, momentum conservation is not required. During the last five decades the TMS mechanism has been extensively explored under different theoretical approaches [72–75]. The most widely used theory has been introduced by Arias and Mills and is applied to ultrathin ferromagnetic films with morphological surface inhomogeneities (islands and pits) [75]. For an in-plane magnetization oriented along the external field direction and neglecting

magnetocrystalline anisotropies, the spin wave dispersion can be written in the form:

$$\left(\frac{\omega}{\gamma}\right)^2 = \left(\frac{\omega_{FMR}}{\gamma}\right)^2 - 2\pi M_s\gamma^2 q t_{FM}\{[sin^2\theta_M - cos^2\theta_M cos^2\phi_q][H_o cos(\theta_H - \theta_M) \\ -4\pi M_{eff} sin^2\theta_M] - sin^2\phi_q[H_o cos(\theta_H - \theta_M) - 4\pi M_{eff} cos2\theta_M]\} \\ +Dq^2[2H_o cos(\theta_H - \theta_M) + 4\pi M_{eff}(1 - 3cos^2\theta_M)] \tag{4.5}$$

where q is the wavevector of the scattered magnon, ϕ_q is the angle between the magnon propagation direction and the in-plane projection of the static magnetization and $D = \frac{2A}{M_s}$ is the spin-wave stiffness. $\left(\frac{\omega_{FMR}}{\gamma}\right)^2$ corresponds to the homogeneous ferromagnetic resonance frequency of the magnetization precession (Eq.3.12).

The second term on the right side of eq.4.5 represents the dipolar interaction. It is negative and proportional to q resulting in a reduction of resonance frequency for magnons with $q > 0$. The third term is analogous to q^2 so it is positive and corresponds to exchange interaction. Therefore for small q, the magnon resonance frequency initially decreases with increasing q, while for further enhancement of q, the exchange interaction term begins to dominate, increasing the magnon resonance frequency. Eventually for a specific magnon $q_{(\phi_q)}$, the magnon resonance frequency will be equal to the FMR mode ($q \sim 0$) frequency and as a result the two modes are degenerate and two-magnon scattering can occur. The magnitude of $q_{(\phi_q)}$ reduces with increasing ϕ_q and m degenerate modes are available for an angle ϕ_q larger than

$$\phi_{q_{max}} = arcsin\left(\frac{H_{FMR}}{H_{FMR} + 4\pi M_{eff}}\right)^{1/2} \tag{4.6}$$

The main result of Arias and Mills theory is that by assuming the presence of rectangular -surface or interface- defects on ultrathin ferromagnetic films, a dephasing contribution to the linewidth and a frequency shift of the resonant field is produced. If a and c are the lateral defect's dimensions and b is the average defect height the two-magnon contribution to the FMR linewidth can be written as:

$$\Delta H^{TMS} = \frac{8H_s^2 b^2 p}{\pi D(2H_o + 4\pi M_{eff})^2} \times sin^{-1}\left(\frac{H_o^{1/2}}{(H_o + 4\pi M_{eff})^{1/2}}\right) \\ \left[H_o^2 + (2H_o + 4\pi M_{eff})^2 \times \left(\left\langle\frac{a}{c}\right\rangle - 1\right) + (H_o + 4\pi M_{eff})^2\left(\left\langle\frac{c}{a} - 1\right\rangle\right)\right] \tag{4.7}$$

where p is the fraction of the surface area covered by defects and H_s is the uniaxial out of plane anisotropy field. Correspondingly, the ferromagnetic resonance shift is given

by

$$\Delta H_R^{TMS} = \frac{8H_s^2 b^2 p}{\pi D(2H_o + 4\pi M_{eff})^2} \times \left\{ ln \left[\left(\frac{q_{||}^M}{q_o} - sin^2\phi_{\vec{q}_{max}} \right)^{1/2} + \left(\frac{q_{||}^M}{q_o} + cos^2\phi_{\vec{q}_{max}} \right)^{1/2} \right] \right\} \left[H_o^2 + (2H_o + 4\pi M_{eff})^2 \times \left(\left\langle \frac{a}{c} \right\rangle - 1 \right) + (H_o + 4\pi M_{ef})^2 \left(\left\langle \frac{c}{a} - 1 \right\rangle \right) \right] \tag{4.8}$$

where $q_o \equiv \frac{2\pi M_s t_{FM}(H_o + 4\pi M_{eff})}{(2H_o + 4\pi M_{eff})D}$ and $q_{||}^M = \frac{1}{<a>}$. Finally a more general theory which includes out of plane orientations of the magnetization can be found in references [76,77] and shows that there are no degenerate modes when the film magnetization is oriented with an angle larger than $\frac{\pi}{4}$ from the film plane. Therefore, the two-magnon scattering mechanism is absent in out-of-plane FMR geometry.

4.2.2 Inhomogeneity

Another source of spectral width enhancement is the sample's inhomogeneity. It arises from a wide variety of micro-structural film origins including the angular spread of the crystallographic axis between different magnetic grains, magnetocrystalline anisotropy in a polycrystalline sample and surface anisotropy with film thickness variations [78, 79]. At this regime the film's inhomogeneities dominate the exchange and dipolar interactions between different parts of the film [71] and the whole ferromagnetic sample behaves as multiple non-interacting nanomagnets. As a result, the measured FMR profile is the superposition of local FMR profiles generated by different sample regions. Normally each local FMR profile has Lorentzian shape, which contains intrinsic and two-magnon scattering contribution, resulting in a Gaussian shape for inhomogeneity linewidth broadening.

4.3 Spin Pumping

Another damping category is non-local damping, which is caused due to the contact of the ferromagnetic film with a non-magnetic layer and its main representative is spin pumping. In the following subsections, phenomenological and theoretical spin pumping approach will be given.

4.3.1 Phenomenological description of spin pumping

The injection and detection of spin current in solid state systems was, from the outset, the most important issue for the development of spintronics and for this purpose a number of methods such as non-local spin current injection [80], optical spin current injection [81] and spin pumping have been developed. By using spin pumping, the method primarily used in this study, spin current injection will be achieved when a non-magnetic material is in contact with a ferromagnetic material and the whole system is in FMR conditions. In FMR conditions, a ferromagnet absorbs the maximum energy and the vector of magnetization, $\mathbf{M}$, rotates at the maximum precession angle around the vector of the effective magnetic field $\mathbf{H_{eff}}$, so the projection of the magnetization vector to the equilibrium direction is decreased. Due to angular momentum conservation, this change of magnetization has to be balanced by spin motion. The magnetization of the material is due to the localized spins. The free electrons which move into the ferromagnet feel the other aligned spins through the exchange interaction, whose Hamiltonian is expressed by H=-J $\sum \overrightarrow{s_i} \cdot \overrightarrow{S_j}$, where $\overrightarrow{S_j}$ is the spin of each atom $\overrightarrow{s_i}$ is the spin of each free electron and J is a constant which parameterizes the strength of the interaction. The system, in order to minimize the energy, makes the two spins parallel and as a result the free carriers are polarized. Additionally, electrons that locate into the non-magnetic material near the interface feel this polarization also through the exchange interaction and a proportion of these electrons are polarized, in the direction of the external magnetic field. Moreover, the interface allows the flow of electrons which has as a consequence polarized electrons to be transferred from the ferromagnet into the non-magnetic material and non-polarized electrons entering into the ferromagnet. Finally, an excess of polarized electrons is observed at the non-magnetic layer near the interface with spin parallel to the precession axis. This process can be viewed as a source of pure spin current. The spin current is decreased into the non-magnetic material due to spin relaxation and diffusion, in a length scale associated with the spin diffusion length of the non-magnetic material. A schematic representation of this phenomenological description of spin pumping is depicted in Figure 4.2.

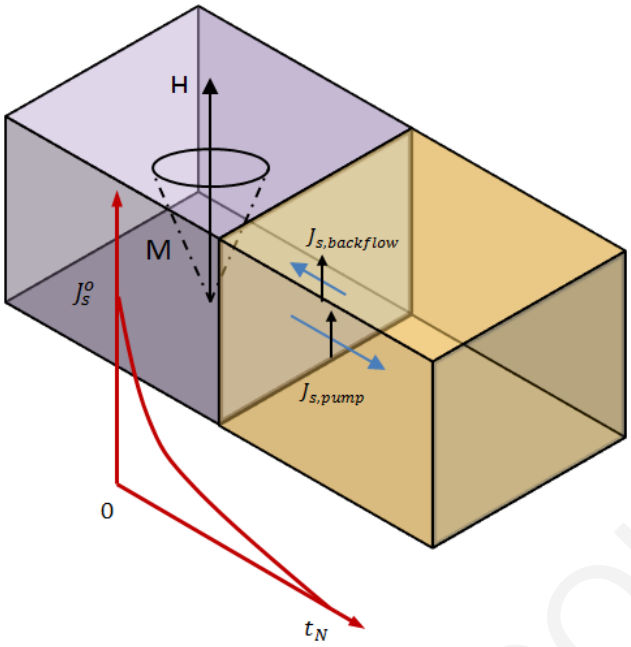

Figure 4.2: Schematic illustration of spin pumping model.

4.3.2 Theoretical description of spin pumping

In 2001, Mizukami et al observed an enhancement of Gilbert damping parameter of NiFe when in contact with a non-magnetic metal [82]. In order to explain this behaviour Tserkovnyak et al [83] showed that an interface enhancement in the Gilbert damping can be created when spin current flowing away from a ferromagnet into an adjacent normal metal reservoir. The spin-pumping theory is based on the peristaltic charge pumping theory developed by Brouwer et al [84] who derived a formula describing that a DC current can be pumped through a quantum dot by periodical varying two independent parameters X_1 and X_2. The general expression of current in spin space is given by,

$$\hat{I} = \hat{1}\frac{I_c}{2} - \hat{\overrightarrow{\sigma}} \cdot \overrightarrow{I_s}\frac{e}{\hbar} \tag{4.9}$$

where I_c and $\overrightarrow{I_s}$ correspond to the charge and spin flow from the ferromagnetic layer into the adjacent non-magnetic layer, and $\hat{1}$ and $\hat{\overrightarrow{\sigma}}$ correspond to the unit matrix and the unit vector of Pauli spin matrices. By following the Brouwer's notation [84, 233] the pumped current is given by

$$\hat{I}_{pump}(t) = e\frac{\partial \hat{n}(l)}{\partial X}\frac{dX(t)}{dt} \tag{4.10}$$

where $X(t)$ is a parameter that modulates the scattering matrix $\hat{s}$ and the matrix emissivity into the lead l is given by

$$\frac{\partial \hat{n}(l)}{\partial X} = \frac{1}{4\pi i} \sum_{mnl'} \frac{\partial \hat{s}_{mn,ll'}}{\partial X} \hat{s}^{\dagger}_{mn,ll'} + H.c. \tag{4.11}$$

where m and n label the transverse modes at the Fermi energy in the normal metal. For the case of spin pumping mechanism, the pumped current is obtained due to the magnetization precession therefore $X(t) = \phi(t)$, where ϕ is the azimuthal angle of the magnetization direction in the plane perpendicular to the precession axis. Finally, by following Tserkovnyak's reasoning [233] the resulting pumped current is

$$\hat{I}_{pump} = -\overrightarrow{\hat{\sigma}} \cdot \overrightarrow{I_s} \frac{e}{\hbar} \tag{4.12}$$

proving that the magnetization precession resulted in spin current without any charge current which was expected due to the absence of any applied voltage. In the following, only the basic principle of spin pumping theory will be given, so for a complete overview of the theory the reader is kindly recommended to follow references [83, 86, 87].

The spin current $\overrightarrow{I_s}$ pumped by the precession of the magnetization into the adjacent non-magnetic reservoir connected to the ferromagnet by a ballistic lead, with a fixed number of transport channels [86] and calculated in an adiabatic approximation, since the period of magnetization precession ($10^{-10}s$) is typically much larger than electronic transit time ($10^{-14}s$). The spin current, $\overrightarrow{I_s}$, flows from the magnetic layer into the non-magnetic layer, perpendicularly to the interface and is given by [83]:

$$\overrightarrow{I_s} = \frac{\hbar}{4\pi} \left(A_r \left(\overrightarrow{m} \times \frac{d\overrightarrow{m}}{dt} \right) - A_i \frac{d\overrightarrow{m}}{dt} \right) \tag{4.13}$$

where $\overrightarrow{m}$ is the unit vector of the magnetization and A_r, A_i are the interface scattering parameters defined by:

$$A_r = \frac{1}{2} \sum_{m,n} [\mid r^{\uparrow}_{mn} - r^{\downarrow}_{mn} \mid^2 + \mid t^{\uparrow}_{mn} - t^{\downarrow}_{mn} \mid^2] \tag{4.14}$$

and

$$A_i = Im \sum_{m,n} [r^{\uparrow}_{mn} (r^{\downarrow}_{mn})^* + t^{\uparrow}_{mn} (t^{\downarrow}_{mn})^*] \tag{4.15}$$

$r^{\uparrow}_{mn}$, $r^{\downarrow}_{mn}$, $t^{\uparrow}_{mn}$ and $t^{\downarrow}_{mn}$ are the reflection and transmission matrix elements of spin-up and spin-down electrons at the interface. Here, m and n, denote the transverse modes at the Fermi energy before and after the scattering process. By using eq.(4.14) and

eq.(4.15) can be obtained:

$$A_r - iA_i = \sum_{m,n}[\delta_{nm} - r^{\uparrow}_{mn}(r^{\downarrow}_{mn})^*] - \sum_{m,n} t^{\uparrow}_{mn}(t^{\downarrow}_{mn})^* = G^{\uparrow\downarrow} - T^{\uparrow\downarrow} \tag{4.16}$$

where $G^{\uparrow\downarrow}$ is the interface spin mixing conductance and $T^{\uparrow\downarrow}$ is the transmission coefficient. The transmission coefficient vanishes for ferromagnetic films which are thicker than the coherence length [86], while the imaginary part of interface spin mixing conductance ($Im(G^{\uparrow\downarrow})$) vanishes for diffusive and ballistic contacts [88]. Therefore, in the present work spin current induced by spin pumping is given by:

$$\overrightarrow{I}_s = \frac{\hbar}{4\pi} ReG^{\uparrow\downarrow} \left(\overrightarrow{m} \times \frac{d\overrightarrow{m}}{dt} \right) \tag{4.17}$$

As already mentioned the injection of spin current from the ferromagnetic layer to the non-magnetic material, provokes additional damping contribution to the magnetization precession. By comparing equation 4.17 and the damping term of LLG equation (3.2) one may notice that they have similar structure. Therefore, by requiring conservation of angular momentum the spin pumping damping term can be derived [89]. The temporal decay of the total spin $\overrightarrow{S}$ in the ferromagnetic layer equals with the pumped spin current $\overrightarrow{I_s}$:

$$\frac{d\overrightarrow{S}}{dt} = \overrightarrow{I_s} \tag{4.18}$$

Moreover the total spin $\overrightarrow{S}$ is related to the total magnetization $\overrightarrow{M}$ of the film via:

$$\overrightarrow{S} = \frac{\overrightarrow{M}_{tot}}{\gamma_e} = \frac{M_{tot}\overrightarrow{m}}{\gamma_e}, \ with \ \gamma_e = \frac{g\mu_B}{\hbar} \tag{4.19}$$

where g is the g-factor and μ_B the Bohr magneton. Hence,

$$\frac{d\overrightarrow{m}}{dt} = \frac{g\mu_B}{\hbar M_{tot}} \frac{d\overrightarrow{S}}{dt} = \frac{g\mu_B}{\hbar M_{tot}} \overrightarrow{I_s} \tag{4.20}$$

Using eq.4.17 and eq.4.20 yields:

$$\frac{d\overrightarrow{m}}{dt} = \frac{g\mu_B ReG^{\uparrow\downarrow}}{4\pi M_{tot}} \left(\overrightarrow{m} \times \frac{d\overrightarrow{m}}{dt} \right). \tag{4.21}$$

As a result, the spin pumping damping term is derived as,

$$\Delta\alpha = \frac{g\mu_B ReG^{\uparrow\downarrow}}{4\pi M_{tot}}. \tag{4.22}$$

By introducing $g^{\uparrow\downarrow} = \frac{G^{\uparrow\downarrow}}{Y}$, where Y is the interface area then yields:

$$\Delta\alpha = \frac{g\mu_B g^{\uparrow\downarrow}}{4\pi M_s t_{FM}}. \tag{4.23}$$

Therefore effective Gilbert damping parameter is given by:

$$\alpha_{eff} = \alpha_o + \frac{g\mu_B g^{\uparrow\downarrow}}{4\pi M_s t_{FM}} \tag{4.24}$$

and the spin mixing conductance is derived as:

$$g^{\uparrow\downarrow} = \frac{4\pi M_s t_{FM}}{g\mu_B}(\alpha_{eff} - \alpha_o) \tag{4.25}$$

which represents the number of spin transmission channels per unit surface area in the interface between ferromagnet and non-magnet. The second term of equation 4.24 can be viewed as an additional damping in the LLG equation.

4.4 Probing spin current transport through spin pumping under FMR conditions

Confirming experimentally the theoretical approach of spin pumping presented in the previous section and developing easily accessible experimental techniques for detecting the injected spin current was of great importance in order to have the ability to create a database of spin current "conductive" materials. Obviously, the first approach was to exploit the generative cause of spin pumping, the change of Gilbert damping constant, when the ferromagnetic layer is in contact with the non-magnetic layer ($\alpha_{FM/NM}$) in comparison with the pristine ferromagnet (α_{FM}). In a perfect spin sink situation, where there is no backflow of spin current, the enhanced Gilbert damping constant can be expressed in terms of FMR linewidth increment [90, 91]:

$$\Delta\alpha = \alpha_{FM/NM} - \alpha_{FM} = \frac{\sqrt{3}}{2}\frac{\gamma}{\omega}(\Delta H_{FM/NM} - \Delta H_{FM}) \tag{4.26}$$

which can reformulate eq.4.25 as [92]:

$$g^{\uparrow\downarrow} = \frac{2\sqrt{3}\pi M_s \gamma t_{FM}}{g\mu_B \omega}(\Delta H_{FM/NM} - \Delta H_{FM}) \tag{4.27}$$

Therefore, the linewidth enhancement can be an evidence of spin current injection due to spin pumping. Moreover, by recording precisely the linewidth broadening a straightforward estimation of the spin mixing conductance can be carried out, giving a simple and sensitive way to quantify the spin pumping efficiency across each

ferromagnet(FM)/non-magnet(NM) interface and it has been used in various studies in the literature to investigate spin injection from a FM into a NM [93–97]. However, as has already been mentioned in section 4.2, extrinsic damping mechanisms can provoke spectral width broadening, affecting the proper calculation of $g^{\uparrow\downarrow}$.

Saitoh et al [98] reported an alternative way to detect spin current due to spin pumping under FMR conditions using the ISHE. More precisely, in a NiFe/Pt bilayer when the NiFe is driven into FMR, a measurable electric voltage difference was detected, transverse to the spin current spatial direction and the spin polarization vector ($\overrightarrow{J}_{ISHE} \propto \overrightarrow{J}_S \times \overrightarrow{\sigma}$) providing clear evidence of spin pumped spin current detection. The combination of FMR and ISHE has opened up a new avenue to study spin transport and spin to charge conversion in a series of different material systems [99–102]. One of the most important advantages for using spin pumping as a spin injection method is that there is pure spin current injection with no net charge current flow. Thus, the spin current injected across FM/NM interfaces avoids the conductance mismatch problem making the spin pumping method in combination with ISHE a popular approach to study spin transport that would otherwise be challenging using conventional electrical spin injection techniques [103]. A thorough examination of the phenomenon was made some years later by Ando et al [92, 104], by examining different parameters that affect the ISHE voltage induced by spin pumping such as microwave power, magnetic field angle and film size, and they develop the phenomenological formalism of the spin pumping in a thin film system which is derived using the spin pumping model and the LLG equation. According to the spin pumping model (eq. 4.17) the dc component of the spin current density, j_s, can be expressed as,

$$j_s = \frac{\omega}{4\pi} \int_0^{\frac{2\pi}{\omega}} g^{\uparrow\downarrow} \frac{\hbar}{4\pi M_s^2} \left[\overrightarrow{m} \times \frac{d\overrightarrow{m}}{dt} \right]_z dt \tag{4.28}$$

where z indicates the direction of magnetization precession axis. Using eq. 4.28 and expressions for dynamic component of magnetization [92], an expression for the spin current density at the FM/NM interface, $j_s^{FM/NM}$, can be derived to be:

$$j_s^{FM/NM} = \frac{g^{\uparrow\downarrow} \gamma_e^2 h^2 \hbar \left[4\pi M_s \gamma_e \sin^2\theta_M + \sqrt{(4\pi M_s)^2 \gamma_e^2 sin^4\theta_M + 4\omega^2} \right]}{8\pi\alpha^2 \left[(4\pi M_s)^2 \gamma_e^2 sin^4\theta_M + 4\omega^2 \right]} \tag{4.29}$$

where h is the microwave magnetic field and α is the Gilbert damping constant. Moreover, the spin current injected into the NM layer will undergo exponential decay

as a result of spin relaxation, the magnitude of which is proportional to the materials spin orbit coupling and spin diffusion length. Thus, the fractional spin current density present at any point in the NM layer is a function of the layer thickness. If the spin current decays along the x-direction, the spin current density present in the NM layer can be expressed as:

$$j_c(x) = \frac{\sinh\left[\frac{d_N - x}{\lambda_N}\right]}{\sinh\left(\frac{d_N}{\lambda_N}\right)} j_s^o \tag{4.30}$$

where d_N is the NM layer thickness, λ_N is the spin diffusion length of the NM material and j_s^o is the spin current density at the interface where $x = 0$. The spin current is converted into a charge current via ISHE and the average charge current density, $\langle j_c \rangle$, can be obtained by considering eq.4.30 as,

$$\langle j_c \rangle = \left(\frac{1}{d_N}\right) \int_0^{d_N} j_c(x) dx = \theta_{SHE} \left(\frac{2e}{\hbar}\right) \left(\frac{\lambda_N}{d_N}\right) \tanh\left(\frac{d_N}{2\lambda_N}\right) j_s^o. \tag{4.31}$$

Furthermore, if the bilayer system is assumed to operate based on an equivalent parallel circuit model, the relation between charge current and ISHE voltage is simply expressed as $V_{ISHE} = [R_F R_N/(R_F + R_N)] I_C = w[\sigma_N + (d_F/d_N)\sigma_F]^{-1} \langle j_c \rangle$, where R_F and R_N are the electrical resistance of the respective ferromagnetic and non-magnetic layers, I_C is the generated charge current, w is the width of the ferromagnet, σ_F and σ_N are the electrical conductivities of the ferromagnetic and non-magnetic layers and d_F and d_N are the respective layer thicknesses. Combining this with eq. 4.31 the final relation between observed V_{ISHE} and film thickness can be derived as:

$$V_{ISHE} = \frac{w\theta_{SHE}\lambda_N \tanh\left(\frac{d_N}{2\lambda_N}\right)}{d_N\sigma_N + d_F\sigma_F} \left(\frac{2e}{\hbar}\right) j_s^o \tag{4.32}$$

enabling the extraction of the spin Hall angle (θ_{SHE}) and the spin diffusion length (λ_N) from measurements of the ISHE voltage as a function of NM film thickness using the spin pumping method [33, 105].

The validity of the spin pumping theory has also be tested in $FM_1/NM/FM_2$ trilayer systems in terms of dynamic exchange coupling [106]. In this case, the LLG equation in order to take into account the effect from the second magnetic film is expanded to [106]:

$$\frac{d\overrightarrow{m_1}}{dt} = -\gamma \overrightarrow{m_1} \times \overrightarrow{H_{eff}^1} + \alpha_o \overrightarrow{m_1} \times \frac{d\overrightarrow{m_1}}{dt} + \alpha_1' \left[\overrightarrow{m_1} \times \frac{d\overrightarrow{m_1}}{dt} - \overrightarrow{m_2} \times \frac{d\overrightarrow{m_2}}{dt}\right] \tag{4.33}$$

For well separated resonances of FM_1 and FM_2, only one layer will precess with large amplitude at a given frequency and spin current is pumped from a precessing FM_1 into a static FM_2 with a total spin pumping damping constant, $\alpha_{sp} = \alpha_1^{'}$. In contrast, if both layers precess symmetrically, with the same amplitude and phase, equal and opposite spin currents are pumped into and out of each layer, causing no net effect on damping, $\alpha_{sp} = 0$. However, if the magnetizations excited in antisymmetric precession, the coupled mode should be doubly damped, $\alpha_{sp} = 2\alpha_1^{'}$. Various studies in the literature investigated the dynamic exchange coupling spin pumping in trilayer systems through the in-plane angular dependence of the applied magnetic field of trilayers containing slightly modified FMs [106, 107] or by means of broadband ferromagnetic resonance for two identical FMs [108, 109] proving the validity of the spin pumping model.

Chapter 5

Electron Spin Resonance

5.1 Fundamental principle of ESR

ESR technique is used to study the properties of unpaired electrons in paramagnetic species. As already mentioned above (Section 2.1), a free electron is quantised into two electronic states spin-up, $m_s = \frac{1}{2}$, and spin-down, $m_s = -\frac{1}{2}$, which are degenerate in the absence of external stimuli. The degeneracy is lifted in the presence of an applied external magnetic field (B_o), due to the interaction with the electron's magnetic moment, $\overrightarrow{\mu}$. This is termed the Zeeman effect. The unpaired electron will have a state of lowest energy when the moment of the electron is aligned with the magnetic field ($m_s = -\frac{1}{2}$) and a highest energy state ($m_s = \frac{1}{2}$) when $\overrightarrow{\mu}$ is antiparallel with magnetic field, B_o . The energy of each orientation is the product of μ and B_o. For an electron $\mu = m_s g_e \mu_B$, where μ_B is the Bohr magneton and $g_e \approx 2.0023$ is the g-factor of the free electron. Therefore, the relative energy, E, of the two electronic m_s states, the Zeeman levels, is then given by: $E = m_s g_e \mu_B B_o$. Irradiation by microwave photons of energy hf_{MW} will result in absorption when the energy difference between states matches that of the photon which results in a transition between the electronic states: $\Delta E = hf_{MW} = g_e \mu_B B_o$ (Figure 5.1).

However, the description of an unpaired free electron almost always does not correspond to a realistic context, since a common sample includes a large ensemble of spins interacting among themselves and with their environment. Thus, the collective behavior becomes quite different. The electron spins are statistically distributed in

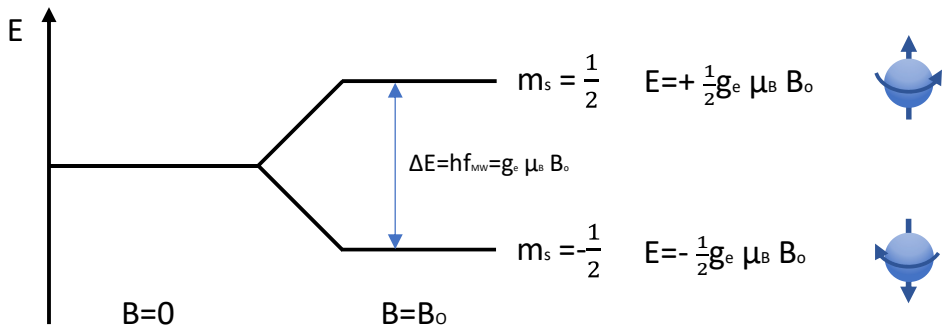

Figure 5.1: Removal of degeneracy for a simple S=1/2 system in the presence of an applied external magnetic field (B_o) due to the Zeeman effect.

the spin-up and spin-down states. At zero static magnetic field $B_o = 0$ these states are equally occupied. Once the magnetic field is applied $B_o \neq 0$ at high temperature approximation (room temperature) ,which is valid for the experiments described through this thesis, the relative populations of the two energy states spin-up and spin-down are given by the Boltzmann distribution: $\frac{n_\uparrow}{n_\downarrow} = exp(-\frac{\Delta E}{k_B T})$.

5.2 g-factor

An unpaired electron in a real system, except of the external magnetic field, feels additional effective magnetic fields which originate primarily from the effective SOC. By effective SOC, we mean the overlap between the orbital and spin angular momentum distributions, which respectively depend on the molecular composition and geometry and the spin density in the charged molecule [40] (Section 2.2). This has as a consequence a shift (Δg) for the g-factor from its free electron value, the magnitude of which depends on the effective SOC intensity [40, 110]. So the knowledge of the g-factor can be taken as a fingerprint of the molecule. Measurement of the g-factor is easily accessible and with high accuracy through the ESR technique, since the only experimental parameters we need to know are the microwave frequency and the exact magnetic resonance field.

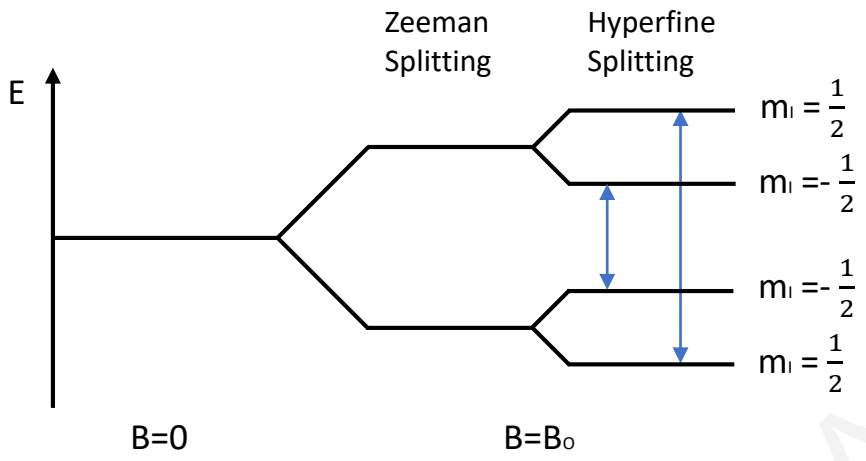

Figure 5.2: Energy level diagram for an unpaired electron interacting with a magnetic nucleus with nuclear spin $I = \frac{1}{2}$

5.3 Nuclear Hyperfine Interaction

An effective magnetic field can be induced also by the interaction between an unpaired electron spin and a nuclear spin, which is termed nuclear hyperfine interaction. Analogous to the case of an electron spin, nuclei of paramagnetic atoms with an odd number of protons and/or neutrons also have a magnetic moment (I) which produces an extra magnetic field in the vicinity of an unpaired electron. Nuclear hyperfine interaction usually prevails over other possible contributions in solution samples. In this case, the fast molecular motion causes an averaging over the anisotropic terms [40] so the resulting resonances arise from the Hamiltonian: $H = g\mu_B \overrightarrow{S} \cdot \overrightarrow{B} + \sum_n \alpha_n \overrightarrow{S} \cdot \overrightarrow{I_n}$ where the first term corresponds to the Zeeman splitting, $g = g_e + \Delta g$ and the latter to the hyperfine splitting for n neighboring nuclei where α_n corresponds to the hyperfine coupling constant of the n^{th} nucleus. The nuclear fields do not displace the spectrum but produce a further small splitting of the energy levels. For example, for the simple case of interaction of one unpaired electron ($S = \frac{1}{2}$) with one nucleus with $I = \frac{1}{2}$, the coupling between the electron and nuclear spin results in a splitting of each electron spin state into 2 levels ($2I + 1$) for $m_I = \frac{1}{2}$, $m_I = -\frac{1}{2}$ (Figure 5.2). The two allowed transitions are shown in the energy level diagram.

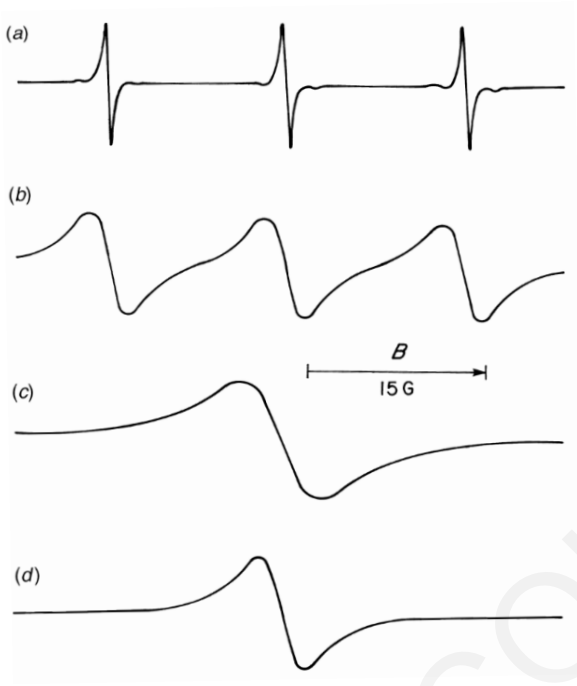

Figure 5.3: EPR spectra of the di-t-butyl nitroxide radical, in ethanol at room temperature at various radical concentrations: (a) 0.1 mM, (b) 10 mM, (c) 100 mM, and (d) pure liquid nitroxide. Spectra taken from ref [1] (p. 323, Figure 10.8)

5.4 Electron-Spin Exchange

According to the Pauli principle each molecular orbital can be occupied by two electrons with opposite magnetic spin quantum number, m_s, while the orbital occupied by the unpaired electron is called singly occupied molecular orbital (SOMO). If two unpaired electrons occupy SOMOs in the same molecule or in spatially close molecules, their wavefunctions may overlap, and interact via the exchange interaction defined by the following spin Hamiltonian: $H_{exc} = J\overrightarrow{S_i} \cdot \overrightarrow{S_j}$. J parameterizes the strength of the interaction and becomes significant only when the radicals approach to a van der Waals distance. At this situation exchange interaction strongly affects the final ESR spectrum obtained.

Figure 5.3 demonstrates the effect of the electron-spin exchange for the case of di-t-butyl nitroxide at various radical concentrations [1, 111]. The first ESR spectrum at Figure 5.3.a corresponds to the low concentration solution with a negligible effect of spin exchange and consists of three lines due to hyperfine interaction of unpaired electron with the nuclear magnetic moment of nitrogen ($I_n = 1$). An increase in the rate of spin exchange (ω_e) at larger radical concentration results in line broadening and

a small shift of the outer lines toward the center of the spectrum Figure 5.3.b. The line broadening, occurs as a result of decreasing of the spin lifetime due to the increase of spin exchange frequency [111]. Further, increase in radical concentration results in the spectrum coalescence in a single broad line Figure 5.3.c when exchange frequency is close to the difference in the ESR frequencies ($\omega_e \approx \gamma\alpha$) [111]. At even higher radical concentrations, the width of this single line becomes exchange-narrowed (Figure 5.3.d) since the electron spins are exchanging so rapidly that the time-averaged hyperfine field is close to zero [1].

5.5 Relaxation and Lineshape

The linewidth and lineshape are important sources of information in ESR spectroscopy. The knowledge of these spectrum characteristics can define the dynamic properties and distributions of sites for a variety of solution and solid-state systems, giving information about the spin relaxation pathways and relative magnitudes of the Hamiltonian terms. More specifically, basic characteristic values that correspond to the nature of the spin-lattice relaxation time (T_1) and spin-spin relaxation time (T_2) can be distinguished from the power saturation behavior of the ESR resonances and the unsaturated linewidth [112]. The spin-lattice relaxation process depends upon fluctuating magnetic fields close to the unpaired electron and corresponds to the decay of the sample magnetization parallel to external magnetic field $\overrightarrow{B}$. Such fields may, for example, be due to lattice vibrations causing the oscillation of local electrically charged particles. Such fluctuating fields can couple with the spin magnetic moment of the electron and hence induce transitions. On the other hand, the spin-spin relaxation process depends on local magnetic nuclei or unpaired electrons affecting the field at the unpaired electron and corresponds to the decay of the transverse magnetization with characteristic coherence time T_2. A random distribution of such fields will blur the energy levels of the unpaired electron resulting in spin dephasing. [40] A long T_2 enables the coherent manipulation of spins while a large T_1 is crucial to maintain a spin polarization along a preferred axis.

T_1 and T_2 spin lifetimes can be defined when the decay of spin polarization is an exponential process by using the continuous wave saturation method [112].

More precisely, when the ESR spectra can be fitted by a Lorentzian function, the coherence time T_2 can be determined by the linewidth using the equation [113] $T_2 = 2/(\gamma_e \Delta H_{FWHM})$ where $\gamma_e = g\mu_B/\hbar$ is the gyromagnetic ratio. Moreover, the intensity of the ESR signal should correspond to the absorption of microwaves caused by excitation of the electrons between the energy level split by the Zeeman effect. The number of electrons at each level obeys a Boltzmann distribution at equilibrium. When the microwave power is too high, there should be no population difference between the spin-up and spin-down states, which results in saturation of the ESR signal [114]. The double integral over the recorded derivative spectrum, scales with the microwave magnetic field B_1 as [115, 116], $DI(B_1) \propto \frac{B_1}{\sqrt{1+\gamma_e^2 T_1 T_2 B_1^2}}$. Therefore, T_1 can be estimated by using the above relationship and by finding the magnitude of the microwave magnetic field that the signal is saturated.

Chapter 6

Experimental Methods

6.1 Technique of Ferromagnetic Resonance (FMR) and Electron Spin Resonance (ESR) measurement

6.1.1 FMR and ESR experimental setup

A schematic representation of ADANI CMS-8400 set-up which is used for our FMR and ESR measurements, is depicted in Figure 6.1.a . In this experimental set-up, a Gunn diode produces microwave radiation with frequency equal with f=9.43 GHz and maximum power 200 mW [117]. Then, the radiation is transferred through waveguides and a circulator to a TE102 microwave cavity. At the center of this cavity, which is a closed system in which microwave standing waves are created, the sample is placed during the measurement. For a known microwave frequency, the wavelength is also known, so it is possible to fabricate a cavity in such dimensions that in the center of the cavity the maximum microwave magnetic field and the minimum electric field is applied. As a result, FMR and ESR measurement is achieved with maximum power, providing as much sensitivity as possible to the system. Another reason of high sensitivity for such systems, is the use of extremely monochromatic microwaves. This is achieved by using waveguides, which are designed to allow a specific frequency to pass through them. Moreover, there is an electronic system with feedback which measures

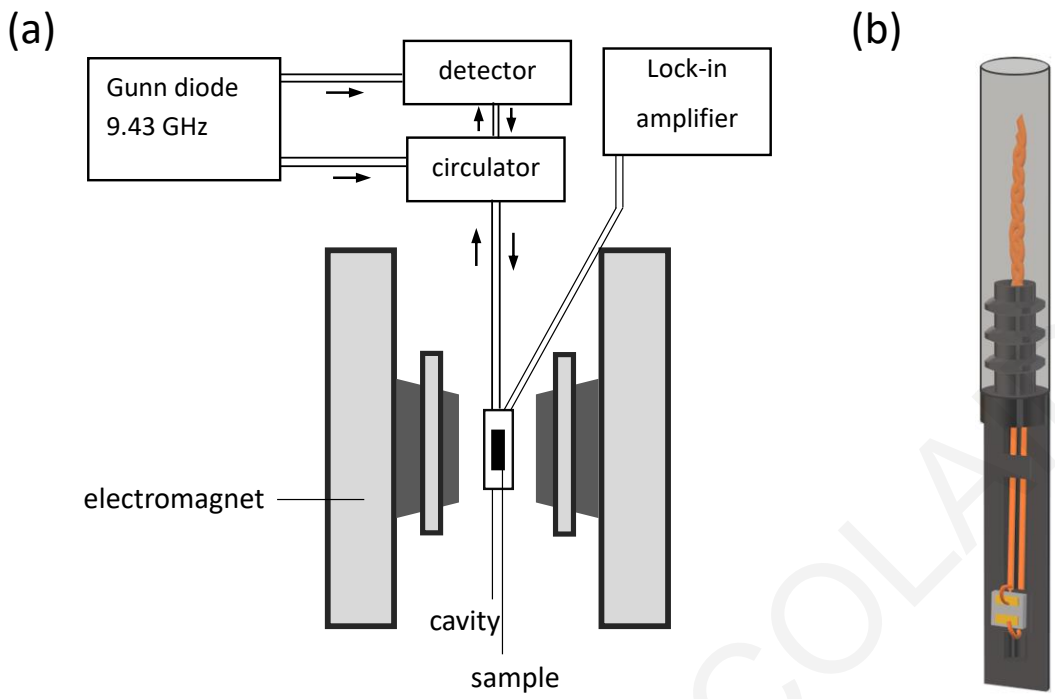

Figure 6.1: (a)Schematic representation of FMR and ESR measurement, (b) Representation of the sample holder for ISHE measurement

the frequency produced in the Gunn diode and at the waveguide near the cavity and controls it in order to maintain it constant.

It is possible to achieve a ferromagnetic resonance measurement by maintaining the external magnetic field constant and vary the electromagnetic radiation frequency which is applied to the sample linearly or maintaining the electromagnetic radiation frequency constant and vary the external magnetic field. In this case, however, the sample is placed in a cavity of specific dimensions for each frequency, so in order to change the frequency, cavity must be changed, that is impossible for a continuous frequency range. In contrast, it is much easier to control the magnetic field, that an electromagnet generates and so the second way is used. Therefore, by varying the external magnetic field and keeping constant a specific microwave frequency, the spectrum of the absorption signal is recorded and is expected to have the shape of a Lorentzian distribution. The signal, however, usually is weak and overlaid by noise. For this purpose, additional coils are used to modulate the external magnetic field at a frequency of 100KHz and by measuring the modulated signal using a lock-in amplifier the spectrum is represented by the first derivative of a Lorentzian distribution. The point that the spectrum is zero

corresponds to the exact resonance magnetic field and is called H_{FMR}, while the magnetic field difference between the maximum and the minimum of the spectrum corresponds to the linewidth, ΔH_{pp}. The relation between half width half maximum and linewidth is given as:

$$\Delta H_{pp} = \frac{2}{\sqrt{3}} \Delta H_{HWHM} \tag{6.1}$$

The linewidth, ΔH_{pp}, and resonance magnetic field, H_{FMR}, were extracted by fitting a Lorentzian derivative to the obtained data by using the following function:

$$\frac{dL}{dx} = A \frac{H - H_{FMR}}{(\Delta H_{pp})^3} \left[1 + \frac{4}{3} \left(\frac{H - H_{FMR}}{\Delta H_{pp}} \right)^2 \right]^{-2} \tag{6.2}$$

where A is a multiplying factor corresponding to the signal intensity and H corresponds to the external magnetic field.

6.1.2 Measurement of FMR and ESR spectra

For the purpose of this thesis, FMR measurements were carried out mainly for NiFe layers for different thicknesses as monolayers, or as bilayers in contact with organic semiconductor layers. In order to achieve this, the experimental setup was modified to accommodate substrates. We developed a 3D printed sample holder, giving special attention to its design to minimize microwave absorption and to allow easy wire installation for ISHE voltage measurement (Figure 6.1.b). The sample holder, in turn, was adjusted in a calibrated rotated ESR tube, allowing for measurements for different angle between the substrate plane and the external magnetic field (θ_H angle). A typical FMR spectra for a 7nm NiFe thin film at $\theta_H = 0^o$ (in-plane direction) is observed in Figure 6.2.a accompanied by its fitting curve used to obtain the fitting parameters H_{FMR} and ΔH_{pp} which are depicted at Figure 6.2.a. Furthermore, we carried out also ESR measurements for a series of Blatter derivatives diluted in dichloromethane (DCM) for identification purposes. The spectra was fitted using EasySpin software [118] in order to find the g-factor, the hyperfine interactions and spectral broadening of each Blatter derivative [119], [120] (Figure 6.2.b). The ESR technique was further used in this thesis for the estimation of spin concentration for different organic semiconductors [41], [121] and in order to confirm the successful synthesis of a Blatter triradical, by comparing the normalized integrated signal of a Blatter triradical and a common Blatter radical (normalized

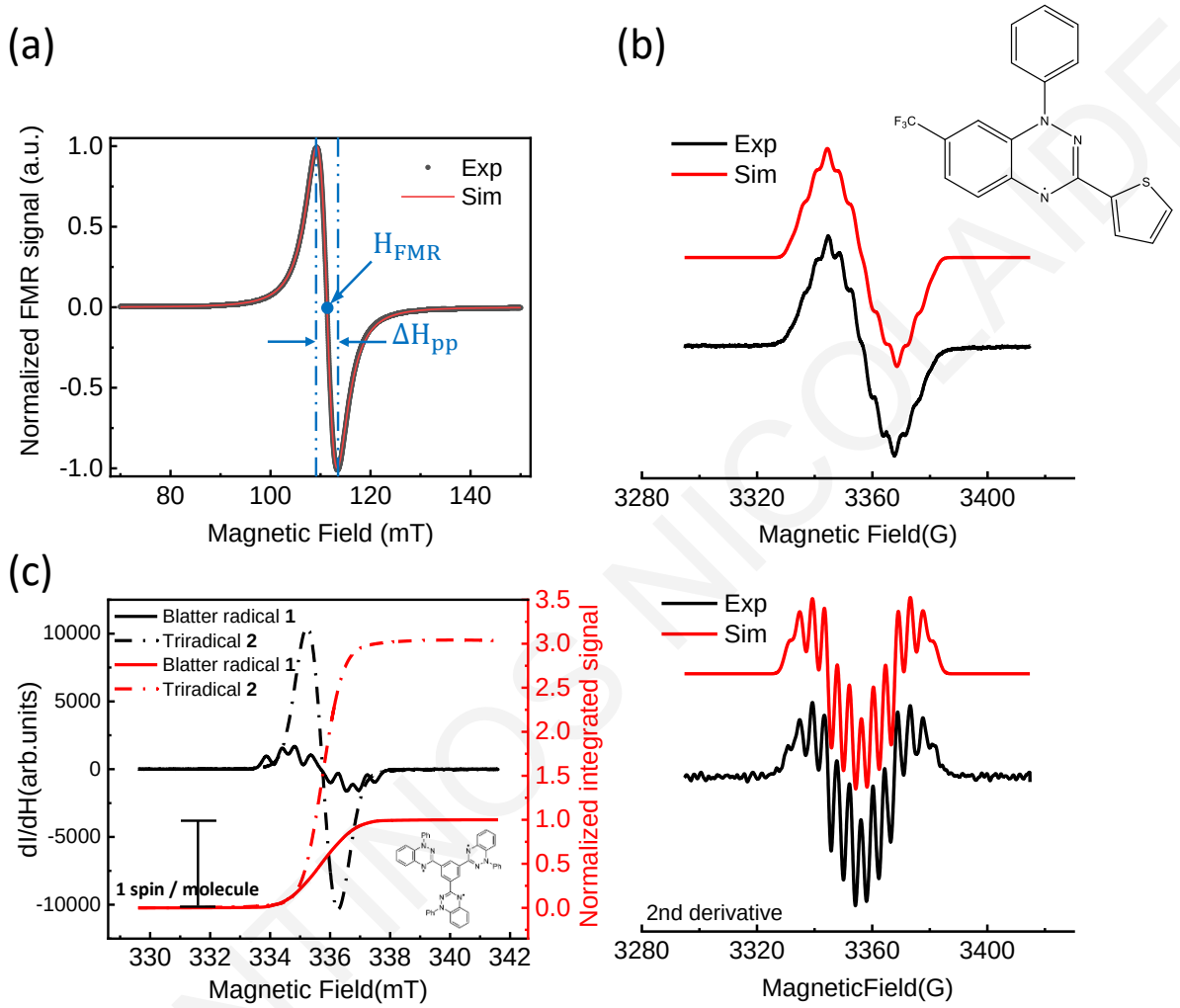

Figure 6.2: (a)A typical measurement of FMR spectra of 7nm NiFe thin film along the film plane, where H_{FMR} and ΔH_{pp} parameters are defined through the fitting. (b)Typical example of ESR measurement of a Blatter derivative diluted in DCM solution (CF_3 Blatter derivative) accompanied by its fitting curve which gives the fitting parameters: g-factor, hyperfine interactions and spectral broadening, confirmed by the 2nd derivative curve. (c)Blatter radical and triradical ESR spectra accompanied by the normalized integrated signal which confirm the triradical state.

with respect to the latter). The signal per molecule for the triradical Blatter is three times greater which corresponds to three spins per molecule supporting its triradical nature [122] (Figure 6.2.c).

6.1.3 Experimental setup of ISHE voltage V_{ISHE} measurement under ferromagnetic resonance

In order to carry out ISHE voltage measurements under FMR we prepared the experimental setup depicted at Figure 6.3.a. Our goal to perform this measurement is the simultaneous recording of the FMR spectra, given by the ferromagnetic layer, and the ISHE voltage V_{ISHE}, which is created at the non-magnetic layer, due to the injected spin current under FMR conditions. We applied contacts -Cu wires, by using silver dag- at the edges of the non-magnetic layer in a direction transverse to spin current spatial direction, $\overrightarrow{J_s}$, and the spin polarization vector $\overrightarrow{\sigma}$, $V_{ISHE} \propto \overrightarrow{J_s} \times \overrightarrow{\sigma}$. The voltage difference signal, which is of the order of hundreds of nanovolts is detected by using a Keithley 2182A Nanovoltmeter, it is amplificated and finally is tracked by using an oscilloscope. The FMR spectra can be converted also to a voltage signal which is provided directly from the CMS-8400 spectrometer and tracked simultaneously with the V_{ISHE} at the oscilloscope. By knowing the time duration of the FMR measurement, since we define it, it is easy to convert it to the magnetic field range of the measurement. An example of ISHE voltage measurement, that we carried out for a NiFe/p-Ge bilayer [123], is presented at Figure 6.3.b.

6.2 Molecular Beam Epitaxy (MBE)

The deposition of ferromagnetic thin films in our samples is performed by using molecular beam epitaxy (MBE). This technique is advantageous over others, as the deposition is made in ultra high vacuum conditions, offering uniformity in the development of heterostructures and precise control of the deposition rate, resulting in high quality epitaxial thin films without vacancies and impurities and with controllable thickness. Our MBE experimental setup consists of two chambers, the supporting chamber, where the substrate is introduced initially, and the growth chamber which

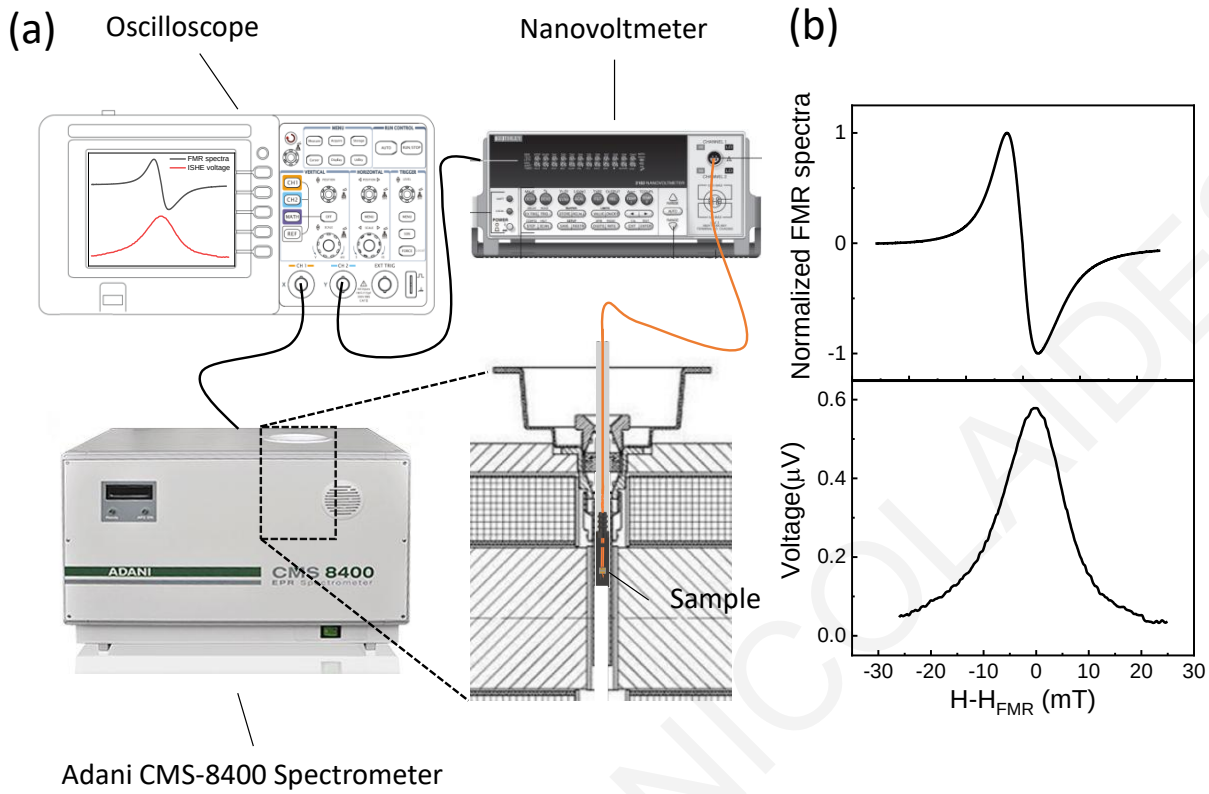

Figure 6.3: (a)Schematic representation of ISHE voltage measurement under FMR conditions. (b)Normalized FMR signal as a function of the in-plane external magnetic field for the NiFe/p-Ge bilayer and simultaneous measurement of ISHE voltage detected at the edges of p-Ge.

never come in contact with the environment, in order to maintain the high vacuum conditions. Four Knudsen effusion cells in which the products are placed in solid form, are located at the bottom of the growth chamber and aligned towards the center of the main chamber where a sample holder is located. They consist of a crucible where the material for sublimation is placed. Sublimation is achieved through e-beam heating by electrons ejected from a filament which is wrapped around the crucible. The beam of sublimated atoms are directed to a substrate which is placed at some distance above the e-beam cells so that it is not heated and affected the deposition process, while due to the prevailing vacuum conditions the scattering possibility is very small. Then the beams from the sublimated material interact onto the substrate resulting in the creation of the respective material. The composition of the developed thin film depends on the relative arrival rates of the product atoms on the substrate and on the relative sublimation rates of the sources. The deposition rate was monitored by a water-cooled

quartz micro-balance and was constant around 0.32Å/min, while the base and growth pressure was approximately $\sim 9 \times 10^{-9}$ mbar and 3×10^{-8} mbar, respectively.

6.3 Magneto-optic Kerr effect (MOKE)

In order to perform a qualitative investigation of the magnetic properties of our magnetic thin film samples, an optical characterization method called Magneto-optic Kerr effect (MOKE) was used. By using MOKE, the rotation of the light polarization direction and the introduction of ellipticity in the reflected beam is described, due to the reflection from the surface of a magnetic thin film. More specifically, the linearly polarized light can be defined as the superposition of equivalent intensity of a right- and a left-circularly polarized beam. A magnetic sample has different refractive index for right- and left-circularly polarized light. Consequently, the two components of linearly polarized light 'travel' with different velocity within the magnetic material and are also absorbed to varying degree. Therefore, a phase difference between right- and left-polarized beam appears, causing an ellipticity in the reflected beam and a small rotation in the polarization direction, which is called Kerr angle [124] [125]. By passing the reflected light through an analyser, the component that is perpendicular to the direction of the incident light can be isolated which is analogous to the sample's magnetization, making MOKE technique particularly useful in the study of surface magnetization.

The longitudinal MOKE geometry is used in order to perform our measurements, where the magnetization vector is parallel to the incident beam and its schematic representation is illustrated at Figure 6.4.a. A monochromatic light beam of 633nm wavelength is emitted by a He-Ne laser and then is polarized linearly in one direction by using a polariser. In the following, the light beam is reflected onto the sample, which is under the influence of a slowly changing magnetic field generated by a Helmholtz coil and then, the reflected light beam passes through an analyser. The reflected signal is analogous to sample's magnetization and is detected by using a photodiode as voltage. By recording this voltage signal (MOKE signal) as a function of the external magnetic field, the hysteresis loop diagram of the ferromagnetic sample is presented. A typical hysteresis loop diagram for a 20nm NiFe thin film by

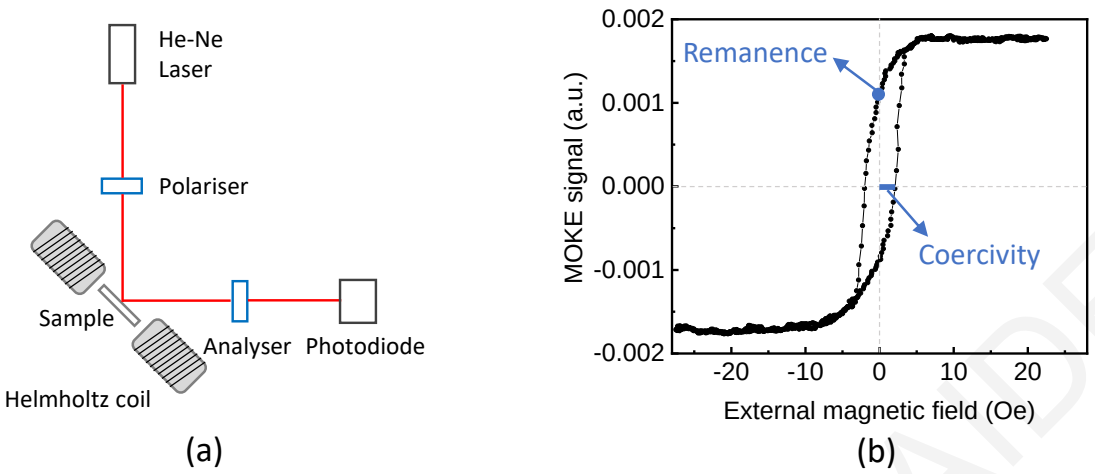

Figure 6.4: (a)Schematic representation of MOKE measurement. (b)Typical MOKE measurement for a 20nm NiFe thin film, where coercivity and remanence parameters are indicated.

using our longitudinal MOKE geometry is observed at Figure 6.4.b. The main experimental quantities that can be extracted from a MOKE measurement are coercivity, that refers to the magnetic field that needs to be applied to erase the magnetization or equivalently the MOKE signal and remanence, which corresponds to the remanent magnetization at zero external magnetic field.

6.4 Atomic Force Microscopy (AFM)

In order to visualize the topography of our samples atomic force microscopy (AFM) technique [126], [127] has been used. The main parts of the AFM device are a cantilever with a sharp tip mounted at its free end, a quadrant photodiode, a laser and piezoelectric ceramics Figure 6.5.a. In an AFM set-up, a laser beam is pointed onto the back side of the cantilever and reflected to a photodiode. As the sample's surface, which is controlled by a piezo scanner, is scanned over the cantilever, the presence of roughness on the surface bends the cantilever and simultaneously the light beam is moved on the quadrant photodiode. By knowing the relation between the torsional force of the cantilever and the position of the beam on the photodiode, the three-dimensional morphological representation of the sample is generated. There are two operation modes for the AFM devices. In contact mode, the cantilever is in full contact with the surface. Strong repulsive interaction force and friction are

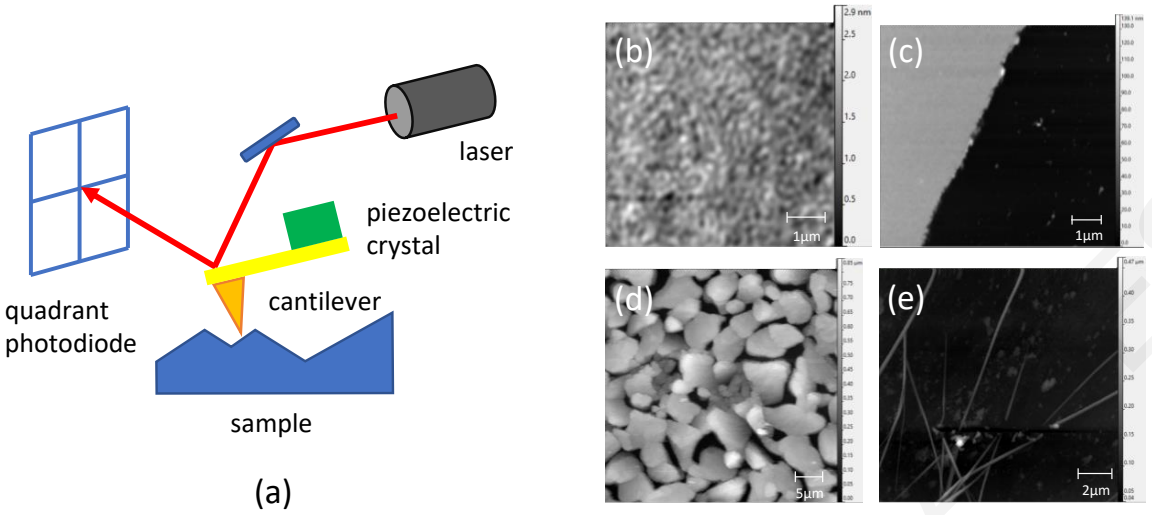

Figure 6.5: (a)Schematic representation of AFM measurement. (b-e)Examples of AFM images that we have carried out for different purposes

present between tip and surface and this technique is usually harsh for the sample. In contrast, by using vibrating mode the measurement can be more sensitive by vibrating the cantilever by using a small piezoelectric ceramic and modulating the light. When the vibrating mode interacts with the surface, the amplitude of vibration may be monitored and used to control the probe's force on the surface. By using the second method, we carried out a series of auxiliary measurements that supports the main findings of published articles, such as the roughness of Blatter radical derivative thin film [121] Figure 6.5.b, the thickness of PEDOT:PSS thin layer [41] Figure 6.5.c, the morphology of a $CH_3NH_2PbI_{3-x}Cl_x$ thin film [128] Figure 6.5.d and the certification of formation of nanowires in sintered formamidinium lead iodide perovskite ($FAPbI_3$) nanocrystal films [129] Figure 6.5.e.

6.5 Hall effect measurement

The estimation of spin diffusion length for organic semiconductors through the classical Einstein relation requires the calculation of mobility and the carrier concentration. These parameters were obtained through Hall effect measurements using the van der Pauw geometry. Conventional van der Pauw geometry has four contact points usually with distances in the millimeter scale. However, this method cannot be utilized for high resistivity materials such as organic semiconductors

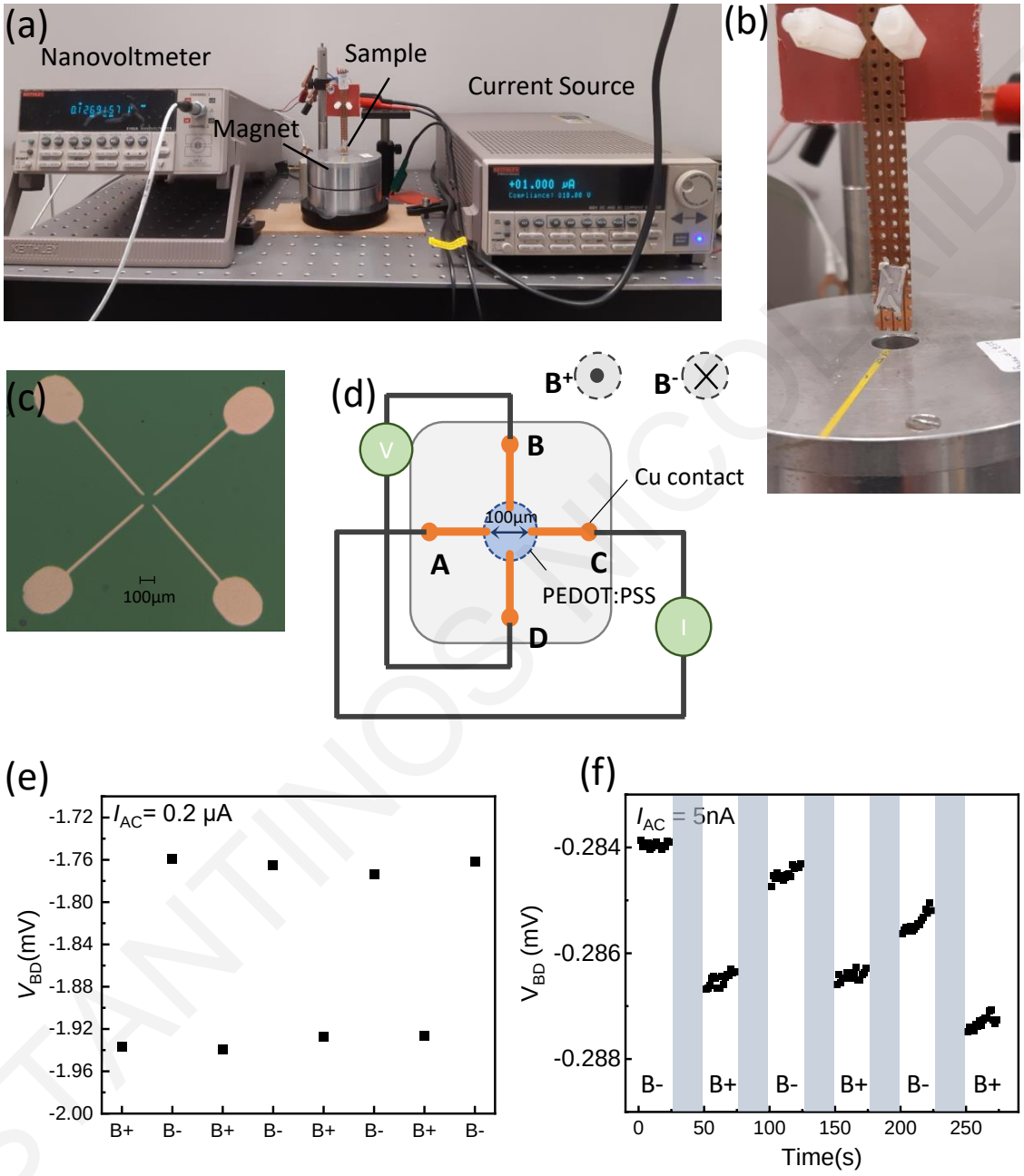

Figure 6.6: (a-b)Schematic illustration of Hall effect measurement. (c-d)Schematic illustration of the Van der Pauw geometry with microscale four-finger electrode gap patterns. (e-f)Voltage measurements against the polarity changes of the magnetic field (e) for AC current and (f) for DC current.

because of lower currents and lower detection sensitivity for the generated Hall voltages. Therefore, in order to maximize the sensitivity we built a homemade experimental setup (Figure 6.6.a, Figure 6.6.b) with microscale (100μm) four-finger electrode gap pattern [130] and high DC magnetic field (1.85 T) as shown in the schematic of Figure 6.6.c and the microscope figure of the device that we built to measure the PEDOT:PSS film's Hall effect Figure 6.6.d. More precisely, we have used two ways to carry out the Hall effect measurements, using AC or DC current (referred to as AC and DC method respectively). In the presence of a positive DC magnetic field (B^+) a sinusoidally modulated current (I_{AC}) (Keithley 6221 Current Source) with amplitude 0.2μA and +0.1μA offset is applied (AC method) (a constant current I_{AC}=5nA, is applied (DC method)) between opposite contacts, e.g. A and C and the voltage difference is measured between the other pair of contacts e.g. B and D (V_{BD}) using a Lock-in amplifier (Ametek 7230) (AC method) (using a Keithley 2182A Nanovoltmeter for DC method). In order to calculate the Hall voltage, the same procedure is repeated by reversing the magnetic field and the current flow in order to subtract undesirable extrinsic effects like thermoelectric and magnetoresistance effect [130]. Therefore, the mean Hall voltage between contacts B and D is given by, $V_{BD} = \frac{V_{BD}(B^+,I^+)-V_{BD}(B^-,I^+)+V_{BD}(B^+,I^-)-V_{BD}(B^-,I^-)}{4}$. The whole process is repeated after interchanging the voltage and current pairs of contacts and the average Hall coefficient can be calculated as $R_H = \frac{t_s(V_{BD}+V_{AC})}{2BI}$ where t_s is the sample's thickness. Finally, the carrier concentration is given by $N = \frac{1}{R_H * e}$, where e is the elementary charge and the carrier mobility can be calculated as, $\mu = R_H * \sigma$, where σ is the conductivity. An example of our Hall voltage measurements is presented in Figure 6.6.e and Figure 6.6.f for PEDOT:PSS [41].

6.6 Substrate cleaning procedure

Three types of substrates have been used to complete the research contained in this thesis: Si/SiO_2, Quartz and microscope slide-glass. It is important to properly clean the substrate's surface before spin-coating the organic material or deposition of the magnetic layer to allow coupling across the interface and ensure full and even coverage and simultaneously good quality of the prepared film. The common cleaning procedure that we followed was:

1. 10 minutes sonication in hot Hellmanex III with concentration 1% by volume.
2. Rinse twice in hot de-ionised water.
3. 10 minutes sonication in IPA.
4. Rinse twice in hot de-ionised water.
5. Dry with N_2.
6. 10 minutes in UV-ozone cleaner.

6.7 Materials

This section is devoted to the main materials used in the development of the bilayers used in our projects: the ferromagnetic permalloy, in contact with the non-magnetic organics PEDOT:PSS or Blatter radical derivative or the hybrid organic-inorganic $CH_3NH_3PbI_{3-x}Cl_x$.

6.7.1 Permalloy(NiFe)

There are several magnetic materials, that are widely used in spin pumping experiments. However, in organic spin pumping measurements permalloy (NiFe) as the spin injection layer is very commonly used [39] [33] [31]. The vanishingly small magnetocrystalline anisotropy [131] and the small intrinsic damping are some key features that give an advantage over other ferromagnets, and as a consequence spin pumping from NiFe has proven to be more efficient [94]. The SOC for organic materials is expected to be small due to their chemical structure which mainly consist of H, C and O, so is crucial to use the most efficient ferromagnet. Nevertheless, it should be noted that at the first ever measurement of FMR spin pumping into an organic material the insulating Yttrium Iron Garnet (YIG) has been used [132], but then a series of articles questioned the validity of the measurement [133] [134] [135]. It has been shown, that YIG in contact with an organic material in FMR conditions can produce thermovoltages whose symmetry is indistinguishable from that of the

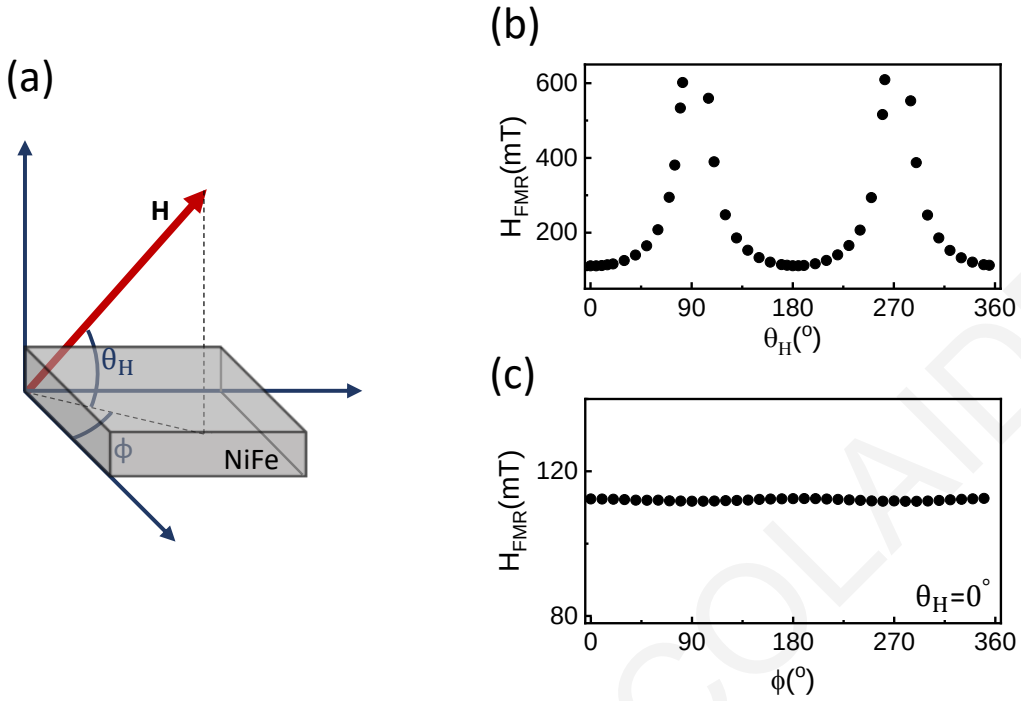

Figure 6.7: (a)A schematic illustration of the measurement setup for the out-of-plane and in-plane magnetic field angle dependence of the FMR signal. (b)The out-of-plane magnetic field angle θ_H dependence of the ferromagnetic resonance field, H_{FMR}, measured for the NiFe film. (c) The in-plane magnetic field angle, ϕ, dependence of the H_{FMR} (for $\theta_H = 0^o$) measured for the NiFe film.

ISHE voltage, due to the spin wave heat conveyor effect [136], making YIG inappropriate ferromagnetic material for organic spin pumping measurements.

For all the above reasons, we decided to use NiFe (Ni 80%, Fe 20%) as the spin injector material in our spin pumping studies. In order to have reproducible and comparable magnetic properties for different samples and batches of deposition, we used Molecular Beam Epitaxy as the evaporation technique, while the lateral dimensions were determined by using metal shadow masks (3.00mm × 1.50mm) and the thickness was monitored by a calibrated quartz thin film controller. A full detailed angular examination of the ferromagnetic resonance field, H_{FMR}, for out of plane and in-plane direction has been carried out for a 7nm NiFe thin film layer and the results are depicted at Figure 6.7.b and Figure 6.7.c, respectively. The out of plane angular dependent characterization of the NiFe film, allows us to extract the saturation magnetization [92], M_s a crucial parameter useful to calculate a variety of spintronic quantities, while the nearly invariant H_{FMR} at the in-plane direction

(Figure 6.7.c) confirming the vanishingly small magnetocrystalline anisotropy of our NiFe film.

6.7.2 PEDOT:PSS

We aim to elucidate how the structural conformation of a conjucated polymer affects the spin transport through it, Chapter 7 by using poly(3,4-ethylenedioxythiophene):polystyrenesulfonate, most commonly refer to as PEDOT:PSS as a testbed material to carry out our investigations. PEDOT:PSS is the most usual choice among different conducting polymers due to its excellent optical, mechanical and electrical properties, outstanding stability at environmental conditions, well established low-cost synthesis process and excellent thermoelectric abilities [137] [138] [139]. Because of these properties, PEDOT:PSS is the choice for many proposed applications such as wearable supercapacitors [140] and sensors [141], electrochemical transistors [142], electrode materials in photovoltaics [143], neutral probes [144] and many others. Although the most properties are due to the PEDOT almost always is blended with PSS counter-ion. PSS functions both as a dispersant to form a stable dispersion in an aqueous solution in the presence of the hydrophobic PEDOT [138] [145] and as dopant to compensate charges of the PEDOT cations [138] [145], allowing for wide tunability of carrier concentration through electrochemical or chemical doping. However, as for other organic semiconductors, a common problem is the small ionization fraction of the PSS, requiring a large amount of the dopant to generate a high carrier concentration. As a result, there is a large amount of non-ionized dopants that can significantly increase the tunneling distance between PEDOT chains and hence reduce the rate of carrier hopping and the overall conductivity of pristine PEDOT:PSS [146]. This obstacle can be overcome by introducing an organic solvent with high solubility in water and high hydrophilicity, such as DMSO, which isolates uncoupled PSS, changes the film morphology and improves the crystallinity resulting in a significant increase of carrier concentration and conductivity [146] [147] [148]. The opposite outcome is achieved by the insertion of a dedopant, such as NaOH, that neutralizes PEDOT:PSS and disrupts the π-conjugation of the PEDOT structure [149] [150]. In order to have different degrees of doping for PEDOT:PSS we employed different amounts of DMSO or NaOH to

Sample ID	P1	P2	P3	P4	P5	P6
Additive	DMSO	-	NaOH	NaOH	NaOH	NaOH
Conc.(Vol%)	1	-	0.5	0.5	0.5	1
[NaOH] (M)	-	-	0.5	4	5	4

Table 6.1: Labeling of the PEDOT:PSS samples in descending doping order with additive concentrations.

respectively adjust the doping or dedoping of the polymer. The series of samples with different doping levels, labelled P1 to P6 is presented in Table 6.1.

Experiments were carried out at room temperature using solution-processed PEDOT:PSS (PH1000, PEDOT:PSS ratio=1:2.5) filtered using a 0.45 μm PVDF syringe filter as the starting material. The substrates were cleaned with deionized water and isopropanol in an ultrasonic bath and dried with nitrogen gas followed by UV-ozone treatment for 10 minutes before use. For Hall, spin pumping, conductivity, optical absorbance and Seebeck measurements a volume of 20 μL of PEDOT:PSS solution was spin coated at 4000 rpm in ambient conditions and the resulting films were then annealed at 120^{o}C for 15 minutes. For ESR and Raman measurements the samples were prepared by drop-casting 5 μL and 20 μL of PEDOT:PSS solution, respectively, and dried at 120^{o}C for 20 minutes.

6.7.3 Blatter (derivative) radicals

Chapter 8 is focused on investigating the possibility of spin current emission from an organic paramagnet in order to achieve a fully organic spintronic device. By exploiting the inherent property of organic radicals, as open shell systems that contains one unpaired electron, in combination with the excellent chemical stability of Blatter radical types compared with other organic radical structures, guides us to the ideal choice of a metal-free organic radical spin source candidate material. The basic structure of Blatter radical (Figure 6.8), the 1,2,4-benzotriazin-4-yl radical was first reported in 1968 [151] and consists of a triazine core and three functional aromatic sites. The unpaired electron mainly locates at the triazine core and the aromatic site 2, while aromatic site 3 characterized as spin isolated [152]. By changing the

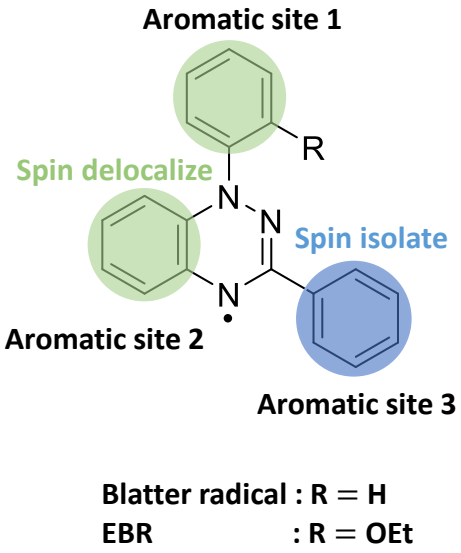

Figure 6.8: Structures of the parent Blatter radical along with the 1-(2-ethoxyphenyl) analogues (EBR).

substituents at the aromatic sites a variety of properties can be provided. Modification of the substituents will significantly affect the molecular packing in the solid state [152], leading to a change in the magnetic [153] [154], electrical and thermoelectrical [155] properties and the stability [156]. This easy transformability of Blatter radical, makes it a candidate material for a number of applications as rechargeable batteries [157], pH sensors [158], anti-cancer activity [159], dynamic nuclear polarization (DNP) reagent [120] and most important for us it is exceptionally promising in spintronic applications, ranging from quantum computing [160] to organic spintronics [161].

Koutentis's group, has pioneered the synthesis of high quality Blatter radical derivatives [162] [163] [119]. They have provided us with 1-(2-thoxyphenyl)-3-phenyl-1,4-dihydro-1,2,4-benzotriazin-4yl radical (EBR) which has great stability, as a suitable candidate to form thin radical films. The EBR thin film was fabricated by spin coating a toluene solution of EBR (5mg/mL) on a Si/SiO_x substrate at 2000rpm in ambient conditions, after a 10 minutes UV-ozone treatment of the substrate forming finally compact thin films with high uniformity and low roughness.

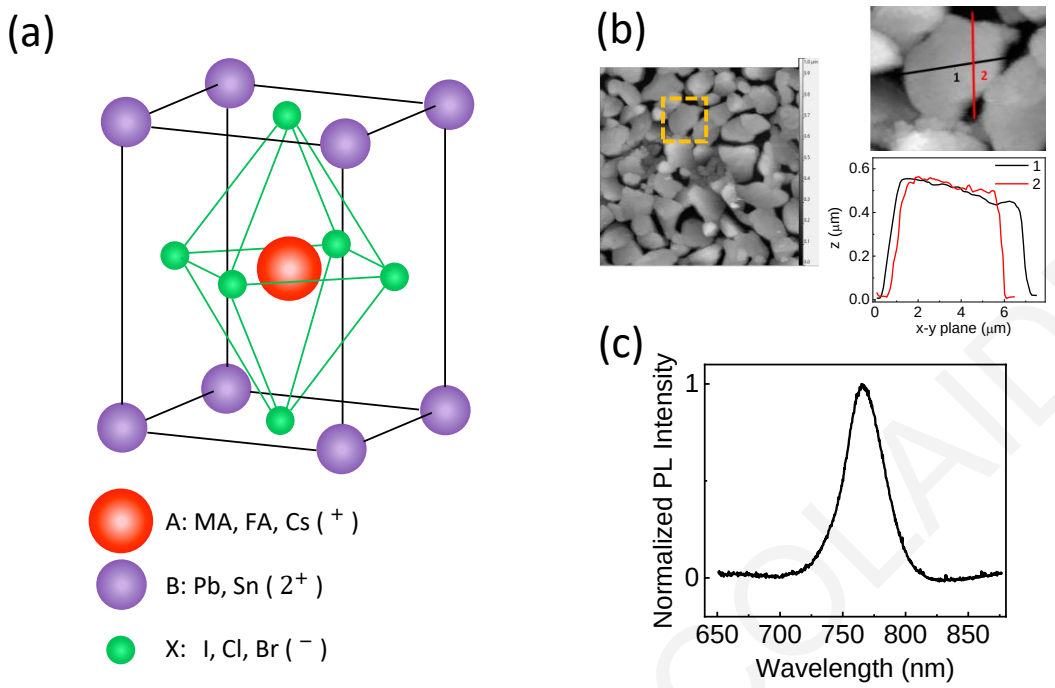

Figure 6.9: (a)Perovskite structure (generic form ABX_3). (b)AFM image of perovskite's surface morphology for an area of 40μm $\times$ 40μm. (c)Normalized intensity of PL spectrum focused at 760nm.

6.7.4 Perovskite

Perovskite is a type of mineral named after the mineralogist Lev Perovski and composed of calcium, titanium and oxygen (chemical formula $CaTiO_3$). However, this name is also applied for any type of crystal structure which has the generic form, ABX_3, depicted in Figure 6.9.a. Depending on which atoms are used in this structure, perovskites demonstrate physical properties ranging from magnetoresistance [164], ferroelectrism [165] and superconductivity [166]. In recent years a form of hybrid organic-inorganic halide perovskite has been attracting particular interest [167] [168], as an exceptional next generation solar cell material , due to a tremendous increase in the power conversion efficiency within few years, reaching a certified value of 25.7% [169] until today. A controllable band gap near 1.6 eV, broad absorption range, high absorption coefficient and long carrier diffusion lengths are some of the organic-inorganic hybrid perovskite's (OIHP's) unique properties, which are responsible for this incredibly high solar cell efficiency [170–173]. OIHPs are typically made using an organic/inorganic cation (A=methylammonium (MA) $CH_3NH_3^+$, formamidinium (FA) $CH(NH_2)_2^+$ or cesium), a divalent cation

(B=Pb^{2+} or Sn^{2+}), and an anion (X=Cl^{-}, Br^{-}, or I^{-}) [144].

Recently, OIHPs have also attracted great interest in the field of spintronics. The presence of heavy elements in the chemical composition of these compounds, suggests possible existence of large SOC and a number of theoretical and experimental articles prove this hypothesis [174] [175]. Therefore, OIHP in combination with other exceptional properties becomes a candidate material for spintronic applications [28] such as spin-optoelectronic devices [176], spin polarized light-emitting diodes at room temperature [177] and perovskite based spin-FET [178]. In this context, in Chapter 9 we demonstrate spin pumping measurements in OIHP in contact with different thicknesses of NiFe layers. More specifically, we used a perovskite with chemical type $CH_3NH_3PbI_{3-x}Cl_x$. The perovskite film was fabricated on a glass substrate using a solution of MAI : $PbCl_2$ (3:1 molar ratio) which was purchased from Ossila. The $CH_3NH_3PbI_{3-x}Cl_x$ layer was spin coated using 40 μL perovskite solution at 3000rpm for 30 s followed by annealing at 90 ^{o}C for 90 minutes. A film with average grain size diameter 5 μm and average height 300 nm was obtained (Figure 6.9.b) with a photo-luminescence (PL) spectrum having a peak at 760 nm (Figure 6.9.c) indicating the desired $CH_3NH_3PbI_{3-x}Cl_x$ formation [179].

Chapter 7

Effect of structural conformation of conjucated polymers on spin transport

7.1 Introduction

In this chapter, which is based on ref [41], we aim to elucidate the link between a polymer's backbone conformation and SOC using poly(3,4-ethylenedioxythiophene): poly(4-styrenesulfonate), most commonly referred to as PEDOT:PSS, as a model material and using chemical doping or dedoping, to alter the polymer's structural conformation. Recently, there has been an emergence of organic spintronic studies, aiming to understand the spin relaxation and spin transport mechanisms in organic materials and to exploit their particular properties to invent new spintronic functionalities and devices [30, 180].

The spin relaxation time, spin diffusion length (SDL) and spin Hall angle (θ_{SHE}) are interconnected crucial figures of merit which determine the spin 'conductivity' of a material and whether it is more suitable as a conveyor or detector of spin. The spin relaxation time is controlled by two principal factors, the spin-orbit coupling (SOC) and the hyperfine interaction [30], as already discussed in section 2.2. Since organic materials mainly consist of elements with small atomic numbers (e.g. H, C, O), very long spin diffusion lengths and spin relaxation times are expected, with associated small spin-Hall angles [39, 114]. Many experimental reports, however, demonstrated spin diffusion lengths ranging from about 1 nm to approximately 1 μm

in organic structures with similar light elements, which implies that in some cases the SOC strength is higher than expected [31–33, 39].

The origin of such unexpected results is still under investigation and a detailed understanding of the mechanism of spin transport in these systems remains a very active research area both theoretically and experimentally [30, 45, 47]. The prominent candidate mechanisms proposed are spin transport mediated by spin-orbit coupled carrier hopping [45, 46], or, at higher concentrations, exchange coupling between localized carriers (polarons) [47, 48]. There may not be a single valid mechanism for a specific OSC or even for the same OSC under different conditions, but rather a combination of the different mechanisms with one prevailing over the other in different circumstances [2, 39].

Understanding a closely related property, the relaxation of spin in OSCs, is also crucial to enable spintronic applications of these materials. Recently, it has been proposed that at room (high) temperature in systems with incoherent charge transport, spin relaxation is governed by an Elliot-Yafet like mechanism [181]. The main characteristic is that instead of taking place during momentum scattering as in inorganic materials, the spin decay is caused by spatial scattering during charge hopping between mixed spin states with the admixture induced by the SOC [37,38,181]. The strength of the SOC is reflected in the spin-admixture parameter, γ, (eq.2.9) which is a measure of the spin-flip probability during a hopping event. Theoretical calculations of γ have been performed by Yu [3,35] and more recently an accurate and more general formalism was introduced by Chopra et al [37, 38]. The conformation of the polymer structure is believed to affect γ since it depends on the relative orientation of neighboring π-orbitals. More specifically, higher SOC is obtained for greater torsional angles along the polymer backbone of an OSC [32].

Based on this framework, we estimate the spin diffusion length of PEDOT:PSS for various degrees of doping by combining electron spin resonance (ESR) and Hall techniques and these results are compared via independent inverse spin Hall effect (ISHE) measurements induced by spin pumping from which θ_{SHE} is determined at corresponding doping levels. The observed trends are attributed to the variation of the degree of torsion between conjugated units along the polymer backbone of PEDOT, with the structural conformation and associated change in planarity monitored via

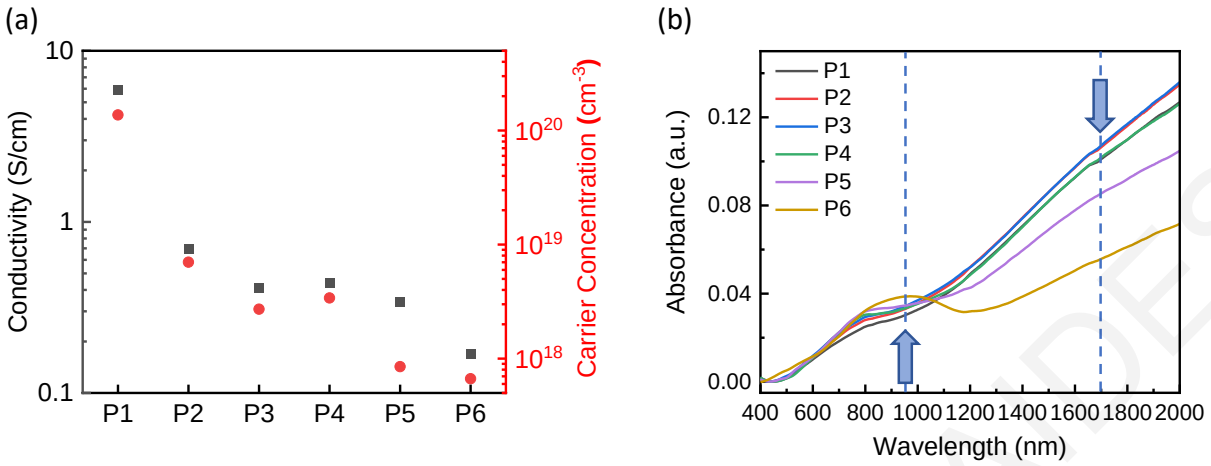

Figure 7.1: (a)Conductivity and carrier concentration for studied samples. Data arranged in increasing degree of dedoping. (b)Optical absorption spectra, recorded for all studied samples.

Raman spectroscopy.

7.2 Experimental Details

A detailed description of PEDOT:PSS properties and PEDOT:PSS's film development procedure has already been discussed at section 6.7.2. The ability to tune the doping level is achieved by using different amounts of DMSO or NaOH in order to dope or dedope the polymer, respectively and the labeling of the PEDOT:PSS samples in descending doping order with additive concentrations is presented in Table 6.1. The doping order is confirmed via conductivity and carrier concentration measurements presented in Figure 7.1.a since both quantities decreased from P1 to P6 and further supported by optical absorbance measurements performed over a wide spectral range in UV-vis-NIR displayed in Figure 7.1.b. The distinct band at $\sim$ 950nm, more prominent in the sample with the lower doping, i.e. P6, is related to polymer polaronic states [182–184]. The spectra contain also a weaker feature at $\sim$ 800nm and a broad band extended to infrared with an apparent peak at $\sim$ 1700nm, that are both attributed to bipolaron absorption [182]. It can be observed that as the concentration of NaOH increases, the bipolaron features quench at the expense of the polaron absorption at $\sim$ 950nm, evidencing the doping reduction [149, 150, 185].

Additionally, for spin pumping and ESR measurements the samples were placed at the center of a TE_{102} rectangular cavity with an operational frequency of 9.43 GHz, while conductivity measurements were carried out through a four-probe method. Optical absorption data were recorded by employing a Perkin Elmer Lamda 1050 spectrophotometer equipped with a three-detector module covering the 300-3000nm spectral range. Finally, the detailed experimental procedures for the Seebeck and Raman measurements can be found in the Appendix A.5 and A.7, respectively.

7.3 Estimation of spin diffusion length

Spin transport in organic materials differs from inorganic structures, since spin carriers in an organic disordered film (polarons), although mobile, are usually localized, while transport in inorganic structures proceeds via delocalized Bloch waves. Consequently, in a regime with a large localized polaron concentration, exchange coupling is favored and as a result spin transport can be realized without charge transfer [47, 48]. This exchange induced spin flow is not the only possible mechanism of spin transport. Polarons can also move through hopping which results in simultaneous spin and charge transport. Both of the above mechanisms influence the spin diffusion length (SDL) λ_N of an OSC and the spin relaxation time (T_1) can be related via the spin diffusion coefficient (D) through the classical Einstein relation $\lambda_N = \sqrt{DT_1}$, the validity of which has already been investigated in disordered OSCs theoretically [35] and experimentally [186]. The spin diffusion coefficient has two major contributions given by the relation,

$$D = D_{hop} + D_{exc} = \mu k_B T/e + 1.6J(R)R^2/\hbar \tag{7.1}$$

The first term corresponds to the hopping contribution, where μ is the mobility, k_B is the Boltzmann constant and e the elementary charge. The second is the exchange-mediated contribution and is a function of the exchange interaction between neighboring polarons, $J(R)$, and the average interpolaron distance, R, which is related to polaron density (n) as $R = 1/\sqrt[3]{n}$. The exchange coupling can be estimated by a hydrogenic exchange interaction expression [2, 39]

$$J(R) = 0.821\frac{1}{4\pi\epsilon\epsilon o}\left(\frac{e^2}{\xi}\right)\left(\frac{R}{\xi}\right)^{5/2} e^{-\frac{2R}{\xi}} \tag{7.2}$$

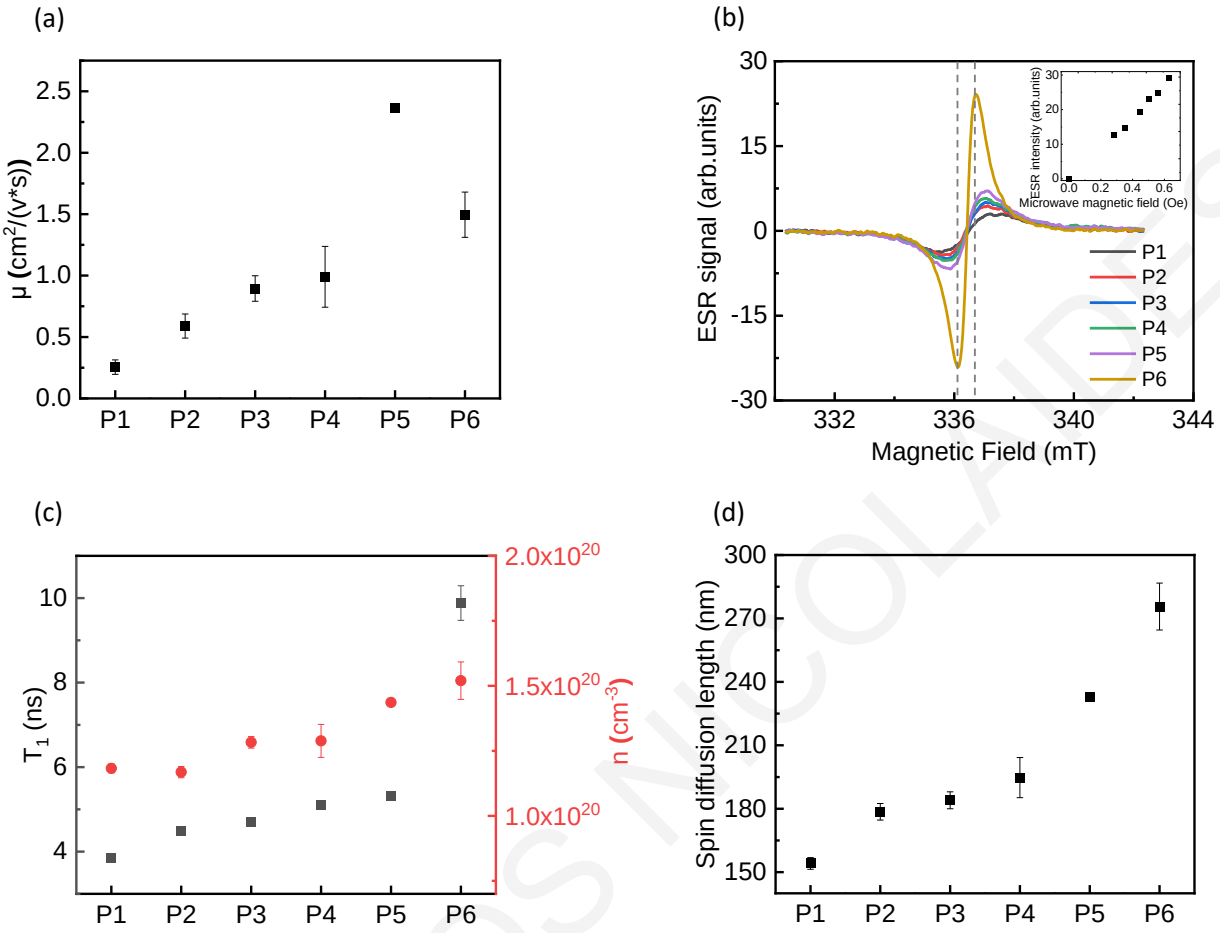

Figure 7.2: (a)Mobility (μ) measurements plotted in increasing degree of dedoping from P1-P6. (b)ESR spectra of the PEDOT:PSS samples at different levels of chemical doping. The inset shows the microwave magnetic field dependence of the ESR intensity of the drop-casted pristine PEDOT:PSS film (P2) at room temperature. (c)Extracted spin relaxation time (T_1) and polaron concentration (n). (d)Estimated spin diffusion length (λ_N) for each sample obtained from ESR, Hall, and conductivity data.

where $\epsilon = 2$ is the dielectric constant, and ξ is the polaron localization length along the $\pi - \pi$ stacking direction, which was experimentally obtained in a previous report to be equal to 11nm for PEDOT:PSS [46]. Evaluating the SDL for every doping level, the mobility (μ), spin relaxation time (T_1) and polaron density (n) have to be experimentally estimated.

The usage of the conventional Hall-effect measurement method to obtain mobility and carrier concentration is often very challenging, since PEDOT:PSS is a disordered organic material with amorphous microstructure and high doping level

and it is expected to produce small Hall voltage [187, 188]. We surpassed this obstacle by utilizing a van den Pauw geometry with microscale four-finger electrode gap patterns and high DC magnetic field [130] by using AC method (further details for the experimental procedure can be found in section 6.5 and a typical example of our Hall voltage measurements is presented in Appendix.A.1 for sample P5). The carrier concentration and mobility results are depicted in figures 7.1.a and 7.2.a, respectively. During dedoping the carrier concentration is gradually decreased by approximately two orders of magnitude from 1.4×10^{20} to $6.7 \times 10^{17} cm^{-3}$. The mobility presents the opposite behavior, decreasing for DMSO-treated PEDOT:PSS film and increasing for the NaOH-treated samples, in agreement with previous experimental reports [189, 190].

The spin nature of charge carriers in PEDOT and other polythiophene-based organic materials under variable doping level can be determined through continuous wave ESR spectroscopy [181, 191–193]. The ESR signal allows investigation of the spin dynamics of polarons, while at the same time acting as a spin counter for the determination of the polaron concentration in the sample under investigation. Figure 7.2.b shows the ESR spectra for all samples at room temperature at constant microwave power. Every spectrum can be fitted by a single Lorentzian indicating that all the spins are in a homogeneous magnetic situation [46, 114]. This fact means that the spin-spin relaxation (dephasing) time, T_2, can be experimentally determined from the linewidth (ΔH_{FWHM}) by $T_2 = 2/\gamma_e \Delta H_{FWHM}$, where γ_e is the gyromagnetic ratio [113]. Furthermore, the doubly integrated spectra give the relative number of spins and by calibrating with the standard DPPH spin-1/2 radical we can obtain the polaron density (n) (Figure 7.2.c). A considerable enhancement of the linewidth is observed as the doping increases and this broadening of the ESR linewidth is in agreement with previous experimental studies with electrochemical doping in thiophene-based organic materials [192, 193]. In contrast, for dedoped PEDOT:PSS, polarons are more localized resulting in a narrowed ESR spectrum. There is also a gradual decrease of polaron concentration as a function of doping (Figure 7.2.c) which contradicts the behavior observed in charge carrier concentration obtained via electrical measurements in Figure 7.1.a. The polaron concentration is 1-2 orders greater than the charge concentration for the sample treated with DMSO. The difference between

polaron and charge concentration can be interpreted by the presence of a 'trapped polaron' population [194, 195], which does contribute to the ESR intensity signal but not to the electrical measurements. Addition of DMSO causes a significant reduction of trapped polaron population while simultaneously leading to spinless bipolaron formation [192, 193]. Consequently, trapped polarons, polarons and bipolarons coexist in PEDOT:PSS, the populations of which are modified during doping.

As already mentioned, by calculating the ΔH_{FWHM} from the ESR lineshape, the transverse spin relaxation or spin dephasing time T_2 can be estimated; however, for the calculation of the SDL the parameter of interest is the longitudinal spin relaxation or spin lattice relaxation time, T_1. This can be determined by measuring the saturation behavior of the ESR intensity as the microwave magnetic field is varied [40, 114] (section 5.5). The inset of Figure 7.2.b shows the ESR intensity dependence as a function of microwave magnetic field for sample P2. A linear dependence is observed even for the highest microwave magnetic field used and this corresponds to the case where $T_1 \approx T_2$ [46, 114]. Similar behavior is observed for all studied samples that indicates a universal relationship of $T_1 \approx T_2$ across all the doping range probed (see Appendix.A.2). The estimated spin lattice relaxation time is plotted in Figure 7.2.c. With all relevant parameters determined, the spin diffusion length can be estimated(Figure 7.2.d). A gradual increase of SDL is observed from higher to lower doping level, varying from $\sim$ 154 nm to $\sim$ 275 nm. The obtained values are in good agreement with previously reported measurements for PEDOT:PSS [46, 135].

7.4 Estimation of spin Hall angle through ISHE measurements

In order to further probe the influence of doping on spin transport we have performed ISHE measurements, induced by spin pumping driven by ferromagnetic resonance (FMR) in a microwave cavity. We used a series of NiFe/PEDOT:PSS heterostructures with the same PEDOT:PSS doping levels, P1 - P6. Figure 7.3.a shows a schematic illustration of the device structure used for the ISHE experiments. A NiFe layer (7nm) was deposited onto a $Si/Si0_x$ substrate by MBE followed by a spin coated thin layer of PEDOT:PSS of approximately 80-90 nm (Appendix.A.3)

The deposition sequence (NiFe and then spin coated PEDOT:PSS) was chosen in order to avoid the deposition of NiFe on the rough surface of PEDOT:PSS and therefore the increment of the damping term by extrinsic factors like inhomogeneity. The effect of inhomogeneity can nevertheless be determined from microwave frequency dependence measurements of linewidth for NiFe/PEDOT:PSS samples. Figure 7.3.b shows a typical measurement for a NiFe/P2 bilayer. The linewidth follows the expected linear behavior as a function of microwave frequency with negligible vertical intercept, indicating that it is independent from other extrinsic damping factors like inhomogeneity. Therefore, we can proceed with the spin pumping damping through the change in the linewidth calculated from one microwave frequency (cavity). During FMR, strong spin accumulation is induced by the precessing ferromagnet at the interface with the OSC and a pure spin current can be efficiently injected into the PEDOT:PSS layer. This excess of aligned spin-1/2 polarons along the magnetic field direction, which can be interpreted equivalently as spin angular momentum transfer from the ferromagnetic to the organic layer, can be detected as an electrical voltage utilizing the ISHE [132](section 4.4). More specifically, in an organic material environment, the ISHE arises when (in the presence of SOC) in addition to hopping between pairs of sites, the hopping in triad via an intermediate site gives rise to a nonzero phase shift for non-aligned molecular orientations of organic materials. This results in a charge imbalance in the direction perpendicular to the spin current and a corresponding induced electric field $\overrightarrow{E_{ISHE}}$ that can be detected electrically [135, 196]. This process is phenomenologically described by the relation $\overrightarrow{E_{ISHE}} \propto \theta_{SHE} \overrightarrow{J_S} \times \overrightarrow{\sigma}$, where $\overrightarrow{J_S}$ and $\overrightarrow{\sigma}$ are the spin current density and spin polarization, respectively. The parameter θ_{SHE}, termed the spin Hall angle, describes the efficiency of the spin- to charge-current conversion process.

Figure 7.3.c shows the voltage signal measured in the NiFe/P2 bilayer device under 62.8 mW microwave excitation power. The detected voltage can be fitted using the relation [98]:

$$V(H) = V_{Sym} \frac{\Delta H_{FWHM}^2}{(H - H_{FMR})^2 + \Delta H_{FWHM}^2} + V_{Asym} \frac{-2\Delta H_{FWHM}(H - H_{FMR})}{(H - H_{FMR})^2 + \Delta H_{FWHM}^2} \quad (7.3)$$

The first term describes the symmetric contribution to the voltage signal from the ISHE, while the second term corresponds to the asymmetric contribution, which is the result of different effects including the anomalous Hall effect and the anisotropic magnetoresistance [197, 198]. The ISHE voltage exhibits a polarity change when

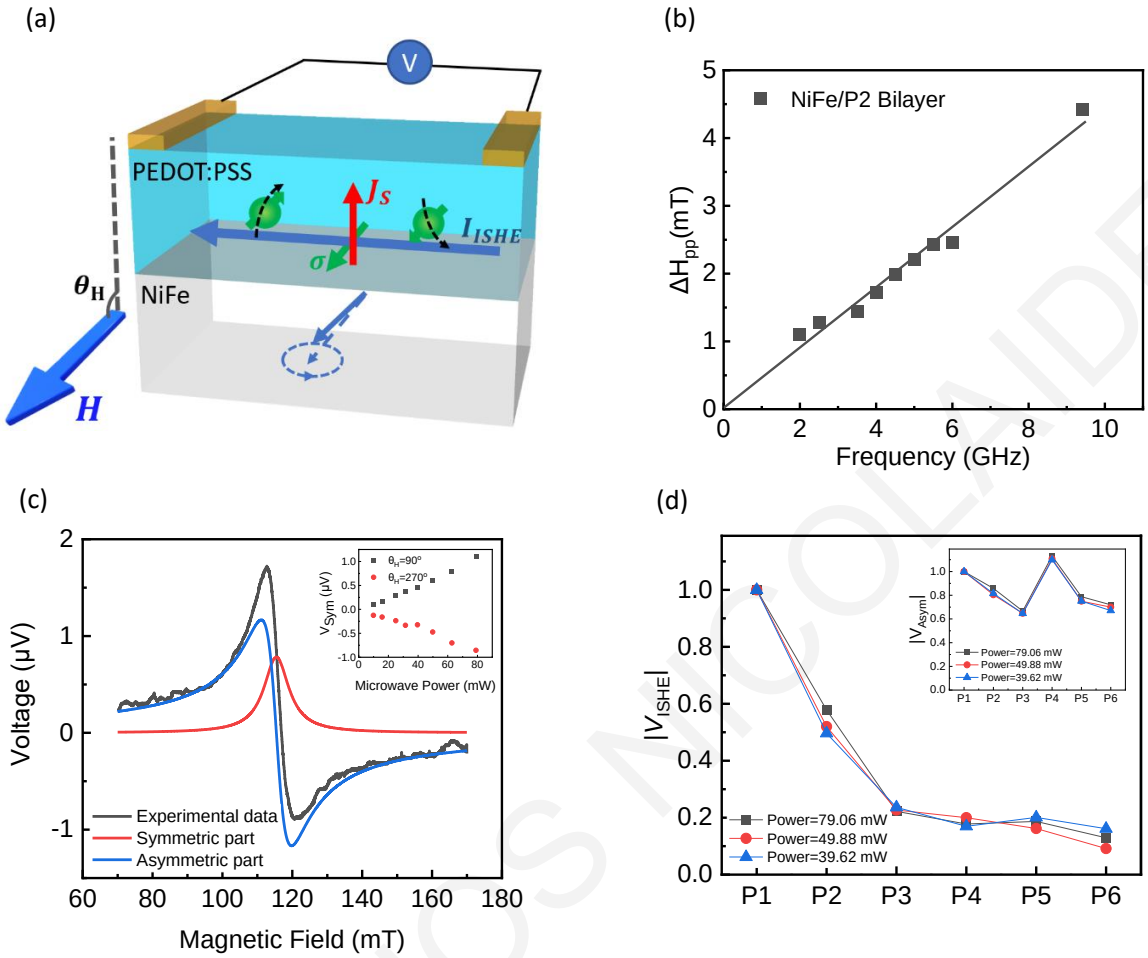

Figure 7.3: (a)Schematic of the inverse spin-Hall effect induced by the spin pumping in a NiFe/PEDOT:PSS bilayer device. H and θ_H denote the external magnetic field and the angle of H from sample plane, respectively. I_{ISHE}, j_s, σ denote the ISHE current due to spin-charge conversion, the flow direction of the spin current and the spin-polarization vector, respectively.(b)Broadband frequency dependence of the peak-to-peak FMR linewidth of the NiFe/P2 sample. (c)Voltage signal detected in the NiFe/P2 bilayer, at $\theta_H = 90^o$ (black line) and the fitted symmetric (red line) and asymmetric part (blue line). The inset shows the microwave power dependence of the peak height of the symmetric voltage for opposing in-plane orientations of the external magnetic field, $\theta_H = 90^o$ and $\theta_H = 270^o$. (d)$|V_{ISHE}|$ measurements for each sample, for three different microwave powers, where $|V_{ISHE}|$ stands for the average of the symmetric voltage for opposing in-plane orientations of the external magnetic field, divided by the absorbed microwave intensity at FMR and normalized by the magnitude of P1. The inset shows the corresponding measurements for the asymmetric part of the voltage.

measured at two opposite in-plane magnetic field directions, $\theta_H = 90^o$ and $\theta_H = 270^o$, in combination with a linear dependence of its magnitude on microwave power (inset of Figure 7.3.c), indicating the successful creation of ISHE voltage induced by spin pumping [92]. The results of the above SHE analysis for all samples are shown in Figure 7.3.d, while the raw data voltage data detected at different microwave power, for the two in-plane external magnetic field directions $\theta_H = 90^o$ and $\theta_H = 270^o$ are shown in Appendix.A.4. $|V_{ISHE}|$ stands for the average of V_{ISHE} for opposing in-plane orientations of the external magnetic field, divided by the absorbed microwave intensity at FMR, P_{abs}, and normalized by the magnitude of P1. There is a clear gradual reduction of the $|V_{ISHE}|$ from the higher doped level P1 to the lower doped level P6. This tendency concerns only the symmetric part of voltage since the asymmetric part presents a different trend for the same doping levels (inset of Figure 7.3.d).

As has been discussed widely in the literature the symmetric voltage can be affected by thermoelectric effects [135, 198]. In order to exclude this contribution to $|V_{ISHE}|$ we measured the Seebeck coefficient (see Appendix.A.5 for results and experimental details). The introduction of NaOH results in an increase of the Seebeck coefficient (Figure A.5.b) in agreement with other experimental studies [190, 199] whereas the change in the symmetric contribution of the voltage decreases monotonically. After clarifying that the symmetric contribution of the voltage corresponds to the V_{ISHE} induced by the spin pumping process, we can estimate the spin Hall angle (θ_{SHE}) for every doping level of PEDOT:PSS layer by equation 4.28 [92]. By following the model presented in section 4.4 θ_{SHE} can be estimated (see detailed description in Appendix.A.6) for every doping level and the results are presented in Figure 7.4.a. A gradual enhancement of spin Hall angle by one order ($10^{-7} - 10^{-6}$) is observed during doping. The magnitude of the θ_{SHE} is comparable with other reported work for PEDOT:PSS [132, 135, 196]. The change in θ_{SHE} with doping is consistent with the variation of the SDL measured in Figure 7.4.a as the θ_{SHE} should be inversely proportional to SDL [92].

Furthermore, spin pumping method can give us an alternative approach to derive the spin relaxation time (T_1), through the angular dependence of $V_{ISHE}(\theta_H)$ [31, 100, 200]. Figure 7.4.b shows a typical measurement for V_{ISHE} as a function of

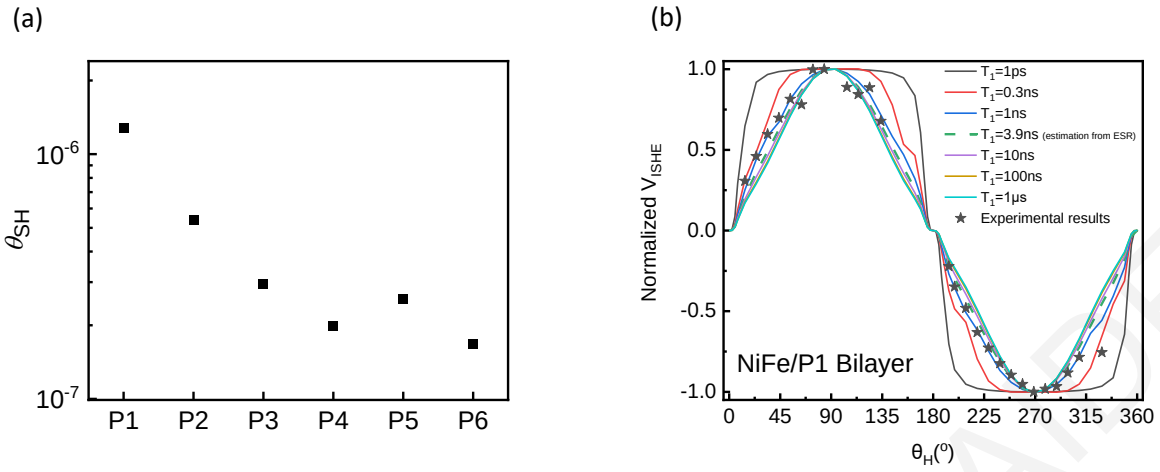

Figure 7.4: (a)Estimation of spin Hall angle (θ_{SH}) from ISHE measurements. (b)V_{ISHE} plotted as a function of θ_H. Fit curves with seven different spin relaxation times (T_1) are shown using equation 7.4 and the solid stars represent the experimental data.

θ_H for a NiFe/P1 sample. In the presence of Hanle spin precession, ISHE voltage is analogous to [100]:

$$V_{ISHE} \propto j_s\Big[sin\theta_H cos(\theta_H-\theta_M)\int_0^{d_N} e^{-x/\lambda_N}dx - cos\theta_H sin(\theta_H-\theta_M)\int_0^{d_N} Re[e^{-x/\lambda_\omega}]dx\Big] \tag{7.4}$$

where $\lambda_\omega = \frac{\lambda_N}{\sqrt{1+i\omega_L T_1}}$, and ω_L is the Larmor frequency and θ_M the out of plane angle of the magnetization. The above equation is plotted in Figure 7.4.b for a series of values of T_1 spanning six orders of magnitudes (solid lines). If $\omega_L T_1 << 1$, the above expression is simplified to $V_{ISHE} \propto j_s sin\theta_M \int_0^{d_N} e^{-x/\lambda_N}dx$ which is valid for materials with short SDL or equivalently small spin relaxation time, in the order of ps (plotted as black solid line in Figure 7.4.b). However, for organic materials with long SDL, as is the case for PEDOT:PSS, this assumption is not valid. We can see from the theoretical solid curves of Figure 7.4.b that the alteration of T_1 from $\sim$ $1ns$ to $\sim$ $1\mu s$ results in very small changes in $V_{ISHE}(\theta_H)$. Nevertheless, our experimental results for the NiFe/P1 bilayer (starred dots in Figure 7.4.b) reproduce this model well, proving the validation of spin pumping model and the Hanle spin precession of polarons into PEDOT:PSS. Furthermore, the value of T_1 is determined to be a few ns which agrees very closely to the value determined using the power dependence ESR method.

7.5 Estimation of γ^2 and qualitative confirmation of PEDOT:PSS backbone conformation through resonance Raman measurements

There are two key findings from the above results from ESR and ISHE measurements; the increase of SDL during chemical dedoping of PEDOT:PSS and the associated reduction of θ_{SHE}, both indicating, that the degree of doping is associated with changes in the SOC strength. Since the doping procedure does not affect the atomic composition we expect that the variation of the SOC originates in a possible alteration of the PEDOT's structural conformation upon doping. Indeed, the interplay between changes of the polymer's backbone conformation and chemical doping has been widely reported for OSCs [201–203]. In such situations, the strength of the SOC can be conveniently parameterized via the spin-admixture parameter, which is directly proportional to the ratio of spin flipping to spin-conserving hopping events [35, 37, 38]. The magnitude of γ^2 is expected to be maximized for large thiophene-thiophene dihedral angles (orthogonal π-orbitals) and minimized for a planar backbone PEDOT [3]. We can estimate γ^2 for every PEDOT:PSS doping level by using the theory proposed by Wang et al [39]. The spin-lattice relaxation time, T_1, that is already obtained is affected by two principal contributions, SOC and hyperfine interaction (HFI), and is given by the relation

$$T_1 = (\omega_{HFI} + \omega_{SOC})^{-1} = (2\Omega_{HFI}^2\tau/3 + 8\gamma^2/3\tau)^{-1}. \tag{7.5}$$

The spin relaxation rate due to the local HFI corresponds to the first term and $\Omega_{HFI} = 2\times10^8 Hz$ is the Larmor frequency of the local hyperfine magnetic field, while the second corresponds to the spin relaxation rate due to the SOC. The dwell time, τ, of a spin on a molecule is given by $\tau = (2D_{hop}/\alpha^2 + 2D_{exc}/R^2)^{-1}$ where $\alpha = 0.37nm$ [148] is the average hopping distance between polarons along the $\pi - \pi$ stacking direction. Figure 7.5.a shows the estimation of γ^2 for every sample. A clear gradual reduction of the spin admixture is observed during dedoping with an overall decline of approximately one order of magnitude $(10^{-6} - 10^{-5})$, indicating that the PEDOT backbone becomes more planar with the insertion of NaOH. Furthermore, the absolute values of γ^2 obtained, are in good agreement with the theoretical estimation for sexithiophene (T_6), shown in Figure 7.5.a as a blue dashed line for comparison, whose structure is similar with

PEDOT:PSS [3, 196].

We experimentally verify the above conclusion via resonance Raman spectroscopy since the backbone conformation in these systems can be conveniently and directly monitored via resonant Raman (RR) spectroscopy. This kind of measurements were carried out by Prof. Hayes group. In Raman spectroscopy, the sample is irradiated by intense laser beams in the UV-visible region (E_o), and the scattered light consists of two types: Rayleigh scattering (elastic), which is strong and has the same energy as the incident beam (E_o) and Raman scattering (inelastic), which is very weak and it is due to the light interaction with vibrating molecules [204]. The difference in energy between the incident photons and the scattered photons is called Raman shift. RR spectroscopy in contrast to the off-resonance technique, which excites a molecule to a virtual state, exploits an excitation energy that coincides with an electronic transition of the investigated molecule, in order to selectively enhance the vibrational Raman signatures that are coupled to the specific electronic transition which results in the high sensitivity of RR spectroscopy. It has been extensively used by the organic semiconductor community for the establishment of structure correlations in π-conjucated molecules [205]. Therefore, one can obtain structural information for example for the neutral polymer or the charged species depending on the selection of excitation wavelength [206].

In a typical RR spectrum of PEDOT:PSS, four main peaks are distinguished [189, 207, 208]. Two of them are ascribed to the stretching modes of inter and intra-ring C−C single bonds of thiophene, centered at $\sim$ 1250 and $\sim 1360\, cm^{-1}$, and the other two to the symmetric and asymmetric stretches of C=C double bonds at ~ 1430 and $\sim 1520\, cm^{-1}$, respectively. The most significant changes observed during the dedoping process are identified in the Raman band between 1400 and 1500 cm^{-1}, which is mainly due to C=C symmetric stretching. This band includes contributions from the symmetric stretching modes of C_α− C_β(-O) bond in the quinoid structure and $C_\alpha = C_\beta$(-O) bond in the benzoid structure at ~ 1430 and $\sim$ 1450 cm^{-1}, respectively, and the asymmetric $C_\alpha = C_\beta$(-O) stretching at $\sim 1400\, cm^{-1}$ [189]. The quinoid structure represents a more linear backbone with enhanced planarity, stemming from the double bond $C_\alpha = C_{\alpha'}$ between the thiophene units, which locks the backbone dihedral angle to 180^o, while the benzoid structure

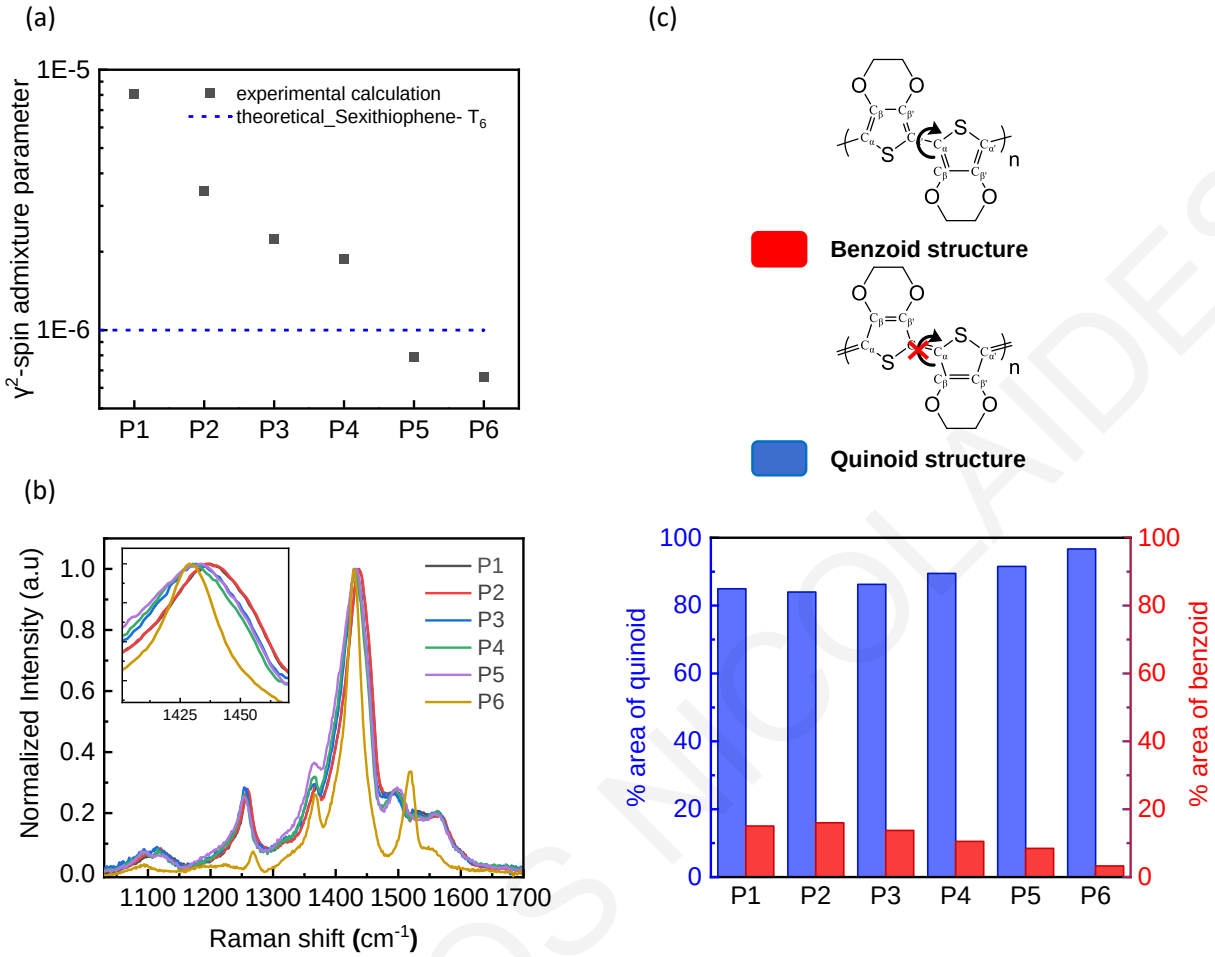

Figure 7.5: (a)Estimation of the spin admixture parameter, γ^2, for P1 to P6. For comparison, we plot the theoretical value of sexithiophene (T_6) (blue dashed line) a material with linear conformation and very similar structure with PEDOT [2, 3]. (b) Normalized RR spectra of the PEDOT:PSS samples at different doping levels with excitation at 532nm. (c)Percentage of the quinoid and benzoid band within our different samples obtained from Raman data deconvolution together with the corresponding structures.

has a favored coil conformation, as the single bond $C_\alpha - C_{\alpha'}$ facilitates inter-ring twisting (Figure7.5.c) [201]. Consequently, Raman spectroscopy gives the opportunity for an in-depth understanding of PEDOT's structural change during chemical doping, by tracking the quinoid/benzoid ratio for every sample. Figure 7.5.b shows the Raman spectra with 532 nm excitation for every doping level. At high doping levels the C=C symmetric stretch band is broader, reflecting the conformational disorder of the polymer in mixed charge states (neutral, polaron and bipolaron). The shorter conjugation length of the neutral benzoid segments at these doping levels shifts the

benzoid bands to higher wavenumbers with enhanced contribution [209, 210] (see Appendix A.7). A clear shift of the position of the C=C symmetric stretch band to lower wavenumbers is observed upon dedoping. This is more prominent in the Raman spectrum of P6, with a downshift of 7 cm^{-1} of the quinoid C=C stretch band, which in combination with the pronounced narrowing of the C=C linewidth (FWHM), constitutes a distinct signature of the increased planarity of PEDOT's backbone expected for the quinoid conformation [209, 211]. This tendency of the resonance Raman spectra is in agreement with the corresponding behavior of Raman spectra during electrochemical and chemical doping or dedoping reported previously [185, 209]. Moreover, the appropriate deconvolution of the C=C symmetric stretch peak shown in Figure 7.5.c (see Appendix A.7 for analysis) further confirms the gradual enhancement of the quinoid, more planar, structure when dedoped and especially its predominance in the case of P6, which along with its narrower linewidth indicates a smaller distribution of PEDOT structural conformations (Figure 7.5.c) [209].

To sum up, the spin admixture parameter, γ^2, was obtained after taking into consideration the effect of the doping/dedoping process on all relevant parameters affecting it, i.e. spin relaxation time, mobility and polaron concentrations. A decrease by one order of magnitude in γ^2 during dedoping suggests weaker SOC strength. This is consistent with the experimental confirmation of increased planarity for lower doping through Raman measurements. The resulting reduction in SOC and therefore, lower probability for spin-flip during hopping is consistent with the longer spin diffusion length or smaller spin Hall angle observed. Consequently, chemical doping becomes a control factor of spin diffusion length, while Raman spectroscopy can be a sensitive detection tool to trace it indirectly.

Chapter 8

Metal-free Organic Radical Spin Source

8.1 Introduction

In the previous chapter we study the regulation of the SOC strength via the manipulation of the PEDOT's structural conformation. In that case, PEDOT layer operates as a spin sink material and the inorganic ferromagnetic layer NiFe, as an emitter of spin. It is a common practice for organic spintronic device concepts to use inorganic ferromagnets as an emitter or detector of spin [31, 33, 212, 213]. Therefore, a major shift in the field of organic spintronics will take place if the ferromagnets (FMs) can be replaced by metal-free organic equivalents, since organic synthesis can enable easy spintronic device design at the molecular level, e.g., via integration with semiconducting polymers. The search for such organic magnetic materials at room temperature has been the focus of various investigations [214–216] and recently the existence of room temperature ferromagnetism in oxidized perylene diimide powder was reported [217]. Despite the recent rapid progress in this field, the question whether a radical can act as a spin source in an organic spintronic device remains unanswered. In this chapter, which is based to ref [121], we show that such a radical film can fulfill the role of a source of spin current in a way that is analogous to spin pumping from a ferromagnet.

The ability to create pure spin currents via spin pumping [87] from a

paramagnet was recently reported, demonstrating that long-range magnetic order is not a prerequisite for a spin emitter material [218]. The double-perovskite oxide paramagnetic insulator, La_2NiMnO_6, provides paramagnetic spin pumping of a pure spin current at room temperature with comparable efficiency to that of typical spin pumping devices involving ferromagnets [218]. Even though paramagnets are relatively understudied spintronic materials, initial studies show that they can support spin current injection, transport [219–221] and spin Seebeck effect [222, 223], setting the basis for future paramagnetic spintronic applications.

The use of an organic paramagnet as a spin current source is a promising route to achieve a fully organic spintronic device. Stable organic radicals, a class of molecules containing one or more unpaired electrons, are an obvious choice for such a paramagnet. Since every radical molecule contains at least one free electron, a solid-state radical layer ensures high spin concentration. The shortest intermolecular interactions between organic radicals, often offer the pathways to propagate the magnetic exchange interactions between the unpaired electrons located on the SOMOs of the nearest neighbor molecules. This could be the cause of short range magnetic correlation in radical layers [214]. A particular class of organic radicals, 1,2,4-benzotriazinyls, named after Blatter who first reported them [151], has remarkable stability in ambient conditions but was underexplored owing to limited availability. Recent improvements in the synthesis of Blatter radicals [119, 162, 163, 224] enabled access to structurally diverse analogues tailored to different applications and increased the general interest for these molecules [152]. For example, a pyrene-Blatter type radical derivative has been proposed as a potential quantum bit [225], while a polymeric Blatter radical was investigated as a cathode material in organic batteries [157]. Moreover, a F_3C substituent Blatter type radical showed an important Seebeck enhancement in comparison to an analogous closed-shell molecule making it a candidate organic thermoelectric material [155] while a high-spin diradical, comprised of two Blatter-type radical moieties, displayed electrical conductivity and remarkable metal-like behavior at low temperatures [226].

The nature of the unpaired electron, combined with their inherent stability, makes Blatter-type radicals ideal candidates on which to develop spintronics and recently, their use as building blocks for organic magnets was widely

suggested [152, 154]. It would be beneficial, for both spintronic studies and future devices, to be able to fabricate robust thin radical layers, ideally in contact with other materials with known properties, e.g., metallic films, without alteration of the radical characteristics. The stability of Blatter-type radical monolayers or thin layers under ambient conditions is still a challenge and is the focus of several studies [160, 161] with some initial steps towards successful fabrication of radical thin layers with robust stability already realized. Of particular importance to spintronics is the possibility of engineering Blatter-type radical materials with strong magnetic exchange interactions to reveal, and subsequently harness, the correlation between structure and magnetism in these systems [153, 156, 227, 228].

In this context, we present the synthesis and the thin film preparation of a Blatter-type radical with outstanding stability and low roughness. These features enable the fabrication of a Blatter-type radical/NiFe bilayer in which the spin current emission from the organic radical layer can be reversibly reduced when the ferromagnetic film is brought into simultaneous resonance with the radical. The results provide an experimental demonstration of a metal-free organic radical layer operating as a spin source indicating the potential of radicals as an alternative to conventional metallic ferromagnets in spintronics.

8.2 Development of Blatter-type radical thin film

We carefully selected a Blatter-type radical, 1-(2-ethoxyphenyl)-3-phenyl-1,4-dihydro-1,2,4-benzotriazin-4-yl (EBR) to enable easy formation of thin films. In a recent study, we reported a 1-(2-methoxyphenyl) (MBR) equivalent radical (Figure 8.1.a) the orthogonal structure of which suppresses the known propensity of the radical to crystallize in 1D columns [228]. In this study, to encourage the formation of uniform thin films, we introduced a subtle structural modification by exchanging the 1-(2-methoxyphenyl) with a more lipophilic and solubilizing 1-(2-ethoxyphenyl) substituent. The 2-ethoxyphenyl Blatter-type radical thin film was fabricated by spin coating a toluene solution of EBR (5 mg/mL) on a Si/Si0x substrate at 2000 rpm in ambient conditions. A uniform radical film was obtained with a noteworthily low roughness, 250 $\pm$ 30 pm, measured by atomic force microscopy (AFM) (details in Figure B.4.a) which

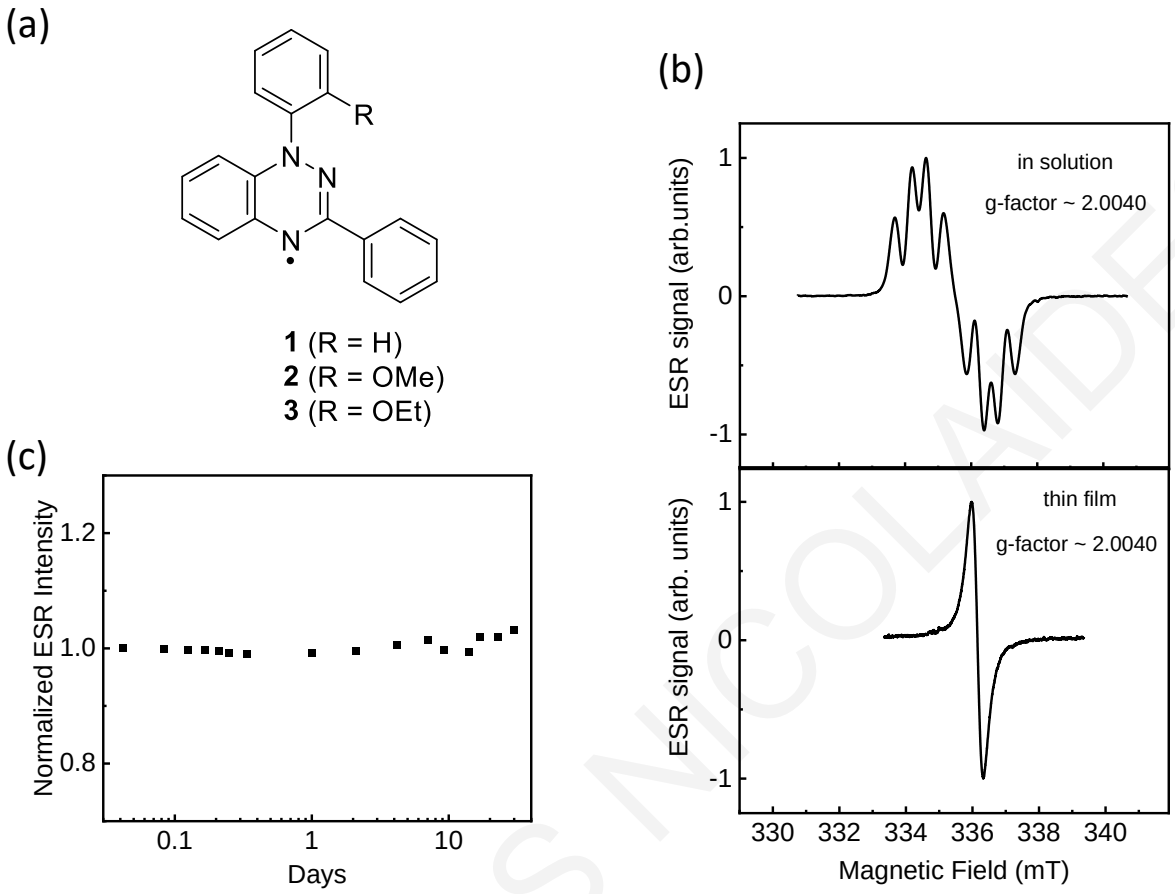

Figure 8.1: (a) Structures of the parent Blatter radical (BR) along with the 1-(2-methoxyphenyl) (MBR) and the 1-(2-ethoxyphenyl) (EBR) analogues. (b) Electron spin resonance (ESR) spectrum of the EBR in solution and in a thin film form with application of the magnetic field in the film plane. (c) Normalized ESR intensity as a function of time for a period of one month.

is at least one order of magnitude lower compared to a previous report [160] and much better than the corresponding MBR film (see Figure B.4.b). The ESR spectrum of the EBR in solution (Figure 8.1.b) shows hyperfine coupling of the unpaired electron with three neighboring nitrogen nuclei, with a measured g-factor 2.0040 (see Figure B.1). The ESR spectra of the solution and the thin film is presented in Figure 8.1.b. The g-factor remains unaffected in the thin film and the hyperfine interaction splitting pattern disappears as expected in the solid state [1, 111], since at high spin concentration the spin-spin exchange dominates the hyperfine interaction. The ESR spectra of the film resemble a single Lorentzian function (see Figure B.6), demonstrating that the EBR molecules in the film behave as a homogeneous broadening system [229] without any

inhomogeneous contribution arising by their possible alteration at the interface. The EBR film, was subsequently monitored by ESR spectroscopy over a period of one month in ambient conditions at room temperature. Figure 8.1.c shows the normalized ESR intensity as a function of time in logarithmic scale from day 0 to day 30 which practically remains constant, indicating outstanding stability under ambient conditions.

8.3 Results

Following the creation of a stable Blatter-type radical film with low roughness, we fabricated a Blatter-type radical film/ferromagnetic bilayer to investigate spin current transport and spin interactions through the interface between the two layers. A NiFe ferromagnetic thin film (7 nm) was deposited onto a Si/SiOx substrate by molecular beam epitaxy followed by a spin coated EBR thin layer of $\sim$ 25 nm (measured by AFM). This bilayer as well as the previous ESR samples were placed at the centre of a TE_{102} rectangular microwave cavity with an operational frequency of 9.43 GHz in which the angle θ_H of the external magnetic field with respect to the sample normal can be controlled. Figure 8.2.a presents typical ESR/FMR spectra of the EBR/NiFe bilayer at $\theta_H = 0^o$ (external applied magnetic field in the sample's plane). The observation of FMR and ESR spectra indicates the successful deposition of the EBR onto the NiFe layer without alteration of the spin or magnetic dynamics, respectively [230]. This is further confirmed by comparing the g-factor of the radical for all three sample cases, in solution, as a single-layer and as a bilayer which are approximately the same $g \approx 2.004$ (Figures 8.1.b and 8.3.b). Similarly, the ESR spectrum is a single Lorentzian distribution indicating a homogeneous system (see Figure B.6).

The change in the applied magnetic field angle, θ_H, during the resonance measurements, causes a variation in the FMR resonance field, H_{FMR}, (Figure 8.2.b) which is typical for an ultra-thin ferromagnetic film [92]. In contrast, there is no measurable influence on the radical resonance field, H_{ESR}, as a function of θ_H (Figure 8.2.b) ruling out the possibility of long-range spontaneous magnetization in the EBR film [231]. By setting $\theta_H = 0^o$ as the in-plane direction, we focus on a range of θ_H, around $\pm 68^o$, where the resonance of the FMR and the ESR spectra coincide, that is,

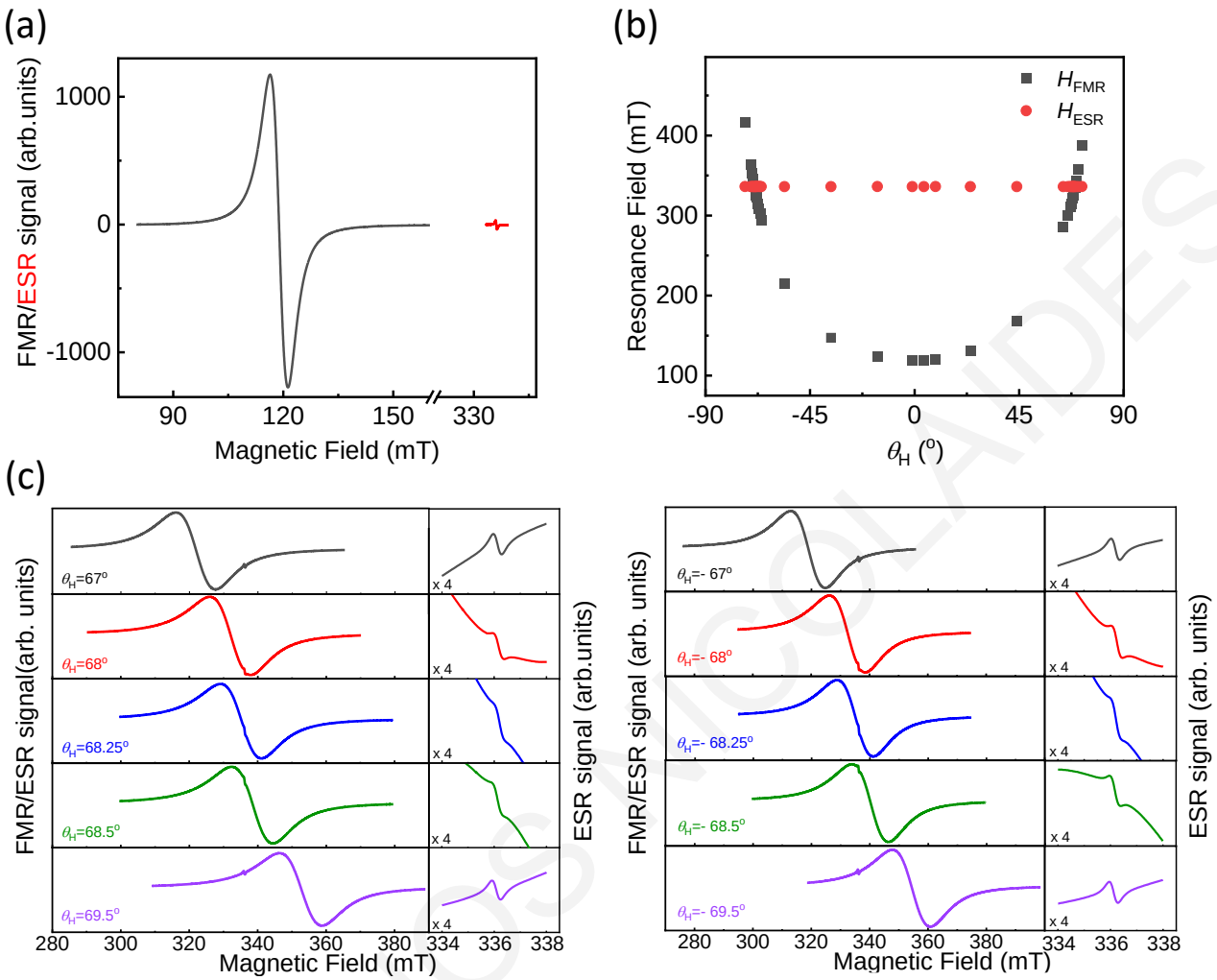

Figure 8.2: (a) Typical ESR/FMR spectra for an EBR/NiFe bilayer for $\theta_H = 0^o$. (b) The magnetic field angle, θ_H, dependence of the resonance fields H_{FMR} and H_{ESR} for the EBR/NiFe bilayer. (c) Detailed measurements of the ESR/FMR spectra close to the coincidence angle.

the two systems can be driven in resonance simultaneously. Detailed measurements of the ESR/FMR spectra close to this coincidence angle are presented in Figure 8.2.c. The g-factor and ESR linewidth, ΔH_{pp}, were determined from the spectra at different θ_H and are plotted in Figures 8.3.a and 8.3.b, respectively. A clear reduction of the g-factor and the linewidth was observed around the angle where the NiFe and the EBR films were driven in resonance simultaneously. This is more pronounced in an alternative representation of the same data, in Figure B.2.b and B.3, where the g-factor and ΔH_{pp} are plotted as a function of the field separation of the two resonances and a decrease was observed in both when $H_{ESR} - H_{FMR} \approx 0$. A comparison of the ESR linewidth of the bilayer with the single EBR film (Figure 8.4.a), shows an increase

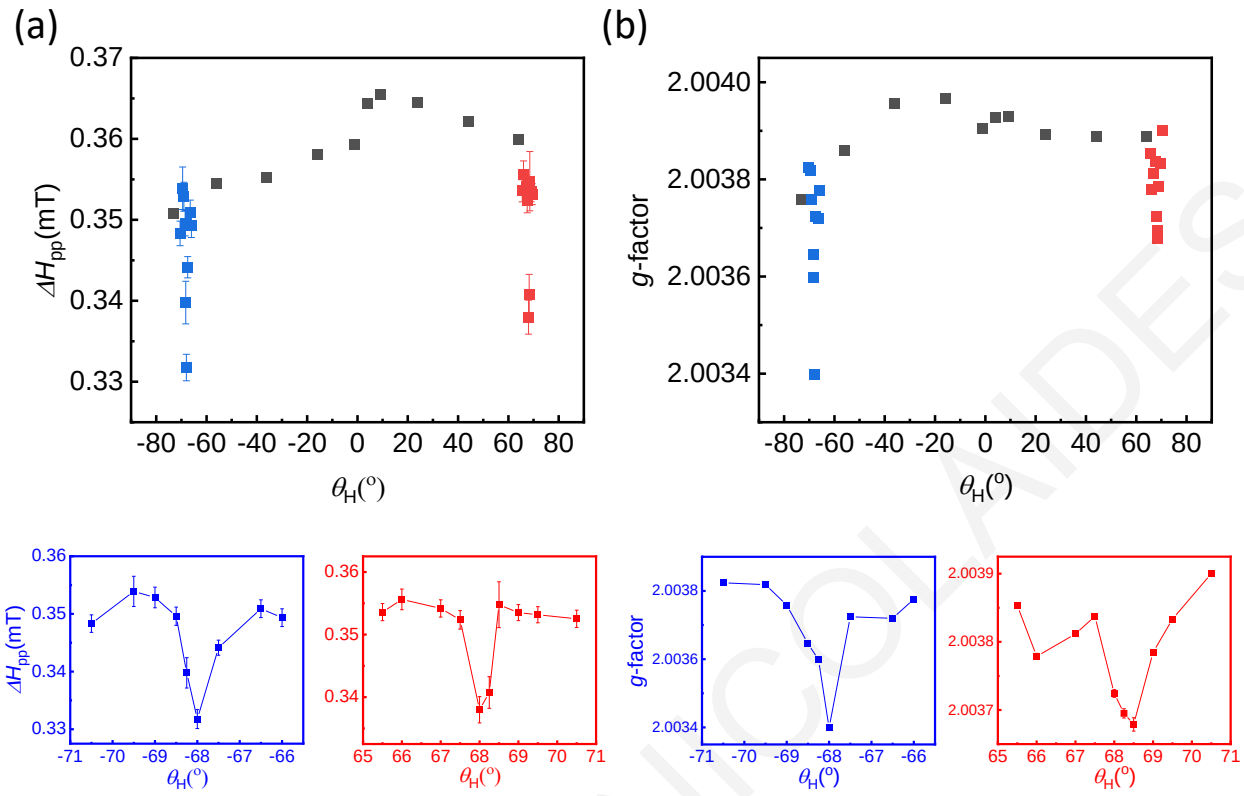

Figure 8.3: The radical ESR linewidth ΔH_{pp} (a) and g-factor (b) in the EBR/NiFe bilayer. The bottom row presents the same data for the cases of simultaneous ESR and FMR resonance ($\theta_H \approx \pm 68^o$).

in ΔH_{pp} for the former for all θ_H angles except in the regions of simultaneous FMR and ESR ($\theta_H \approx \pm 68^o$). In this angle range, ΔH_{pp} decreases down to the value of the single radical film. This observation is the most important result of the present study. It clearly demonstrates that the effect observed was dynamic, only occurring when the two resonances were brought together and that it was reversible. This excluded any possibility of a "permanent" increase of the ESR linewidth in the bilayer due to alteration of the radical nature through interaction with the NiFe layer, for example a linewidth increase which could result from a higher intermolecular distance [230, 232].

8.4 Discussion

We attribute the ESR linewidth increase in the bilayer to spin pumping [87, 233] from the radical into the FM which acts as a perfect spin sink. In general, the term spin pumping refers to the transport of spin angular momentum from a material which

experiences magnetic resonance to an adjacent spin sink layer [233]. Such spin angular momentum transfer causes an increase in magnetization damping, attributed to angular momentum conservation, which is reflected in practice as a broadening of the absorption spectrum, expressed as a linewidth increase [92, 233]. The mechanism of spin pumping has been proposed by Tserkovnyak et al. [83, 86, 233] and is widely used in conducting, e.g., NiFe, Fe, [92, 98, 234] and insulating, e.g., YIG [235], ferromagnetic materials. More recently, it has been demonstrated also in the absence of ferromagnetic order, from the paramagnetic insulator La_2NiMnO_6 [218]. Conventionally spin pumping from ferromagnetic metals and insulators is described through a macrospin approach using a Landau-Lifshitz-Gilbert (LLG) equation. However, such an approach cannot be applied to paramagnets, such as organic radicals at room temperature [218, 219, 221] since the so called spin mixing conductance, controlling the spin current through an interface, cannot be defined in the absence of magnetization. A macrospin description can, however, offer a qualitative understanding of the linewidth increase as spin pumping from the radical layer into the FM which acts as a perfect spin sink. Such a description has previously been useful to describe the spin dynamics for systems with high spin concentration [236].

The realization of spin angular momentum transfer from the radical film to NiFe requires interaction of radical's localized interface spins with the corresponding neighboring NiFe free electrons which could proceed via interface exchange between the two materials [218, 219, 223]. When a magnetic field, B, is applied the energy levels of up- and down- spin states are non-degenerate, differing by the Zeeman energy of $g\mu_B B$, where μ_B is the Bohr magneton. In the presence of interfacial exchange coupling an up (down) spin itinerant electron in NiFe interacts with a localized down (up) spin in the radical film causing a spin-flip equivalent to a transfer of spin angular momentum of $\pm\hbar$ and energy of $\pm g\mu_B B$ [219, 223]. As a result, the spin relaxation time during ESR is decreased with a corresponding broadening of the spectral linewidth, in a manner that is analogous to the broadening of FMR linewidth in conventional spin pumping from ferromagnets [92, 233]. This increase in the linewidth applies for the whole EBR film since no deviation from a uniform Lorentzian is observed indicating a homogeneous broadening system. Spin transport enabling the transfer of angular momentum throughout the EBR could proceed via two mechanisms as in other organic materials. It can be mediated through carrier hopping, which results in simultaneous

spin and charge transport [45,46], and in an environment with a large spin concentration via exchange coupling between localized spins [39, 47]. In our case, the EBR film exhibits remarkable conductivity $\sigma \approx 5 \times 10^{-4}\ Scm^{-1}$ (measurement details in the Figure B.5), of the same order with the highest conductivity Blatter radical derivative measured to date, indicating the possibility of hopping transport. This is in contrast to most neutral π radicals which are insulators or poorly conducting semiconductors with $\sigma < 10^{-10}\ Scm^{-1}$ [237]. Furthermore, using the doubly integrated ESR spectra of the EBR calibrated against the standard DPPH $S = 1/2$ radical we obtain the spin density in the EBR film and consequently a mean distance between the radical spin centers of $\sim 0.4nm$ for which a strong exchange interaction is expected [153,228]. This is consistent with the ESR spectrum having a single Lorentzian shape, a feature characteristic of high spin density radical systems with strong exchange between neighboring molecules [238,239]. Therefore, a contribution to spin transport within the radical film from both mechanisms cannot be rule out.

A contribution to the observed increase of ΔH_{pp} can also arise from factors unrelated to spin pumping, for example, due to a permanent alteration of the nature of the radical molecule itself when deposited on a metallic surface, resulting in the increase of ΔH_{pp} [161, 232]. This possibility, however, can be ruled out by careful consideration of the linewidth measurements of Figure 8.4.a for simultaneous FMR and ESR, where the increase of the linewidth is quenched and ΔH_{pp} reduces to the value of the single radical layer. This observation is inextricably linked with spin pumping. Analogous linewidth reduction due to spin pumping, was previously observed for $FM_1/normal\ metal(NM)/FM_2$ trilayers when the resonant fields of two ferromagnetic layers coincide [106] (Section 4.4). More thorough investigations of this effect followed, both theoretically [240] and experimentally for trilayers $FM_1/NM/FM_2$ or bilayers FM_1/FM_2 for the same [108, 109] and for different FMs [241–243]. More recently, the magnetization coupling in a paramagnetic/FM bilayer has also been reported [244]. The simultaneous resonance of the two FM layers results in coherent precession and simultaneous pumping of spin currents in opposite directions from one layer into the other. The case where the precession of the two layers is in-phase results in no linewidth increase, effectively the spin current emitted by one layer is matched by equivalent absorption of spin current received from the other FM layer [106, 240]. The observed vanishing of the increase in ΔH_{pp}

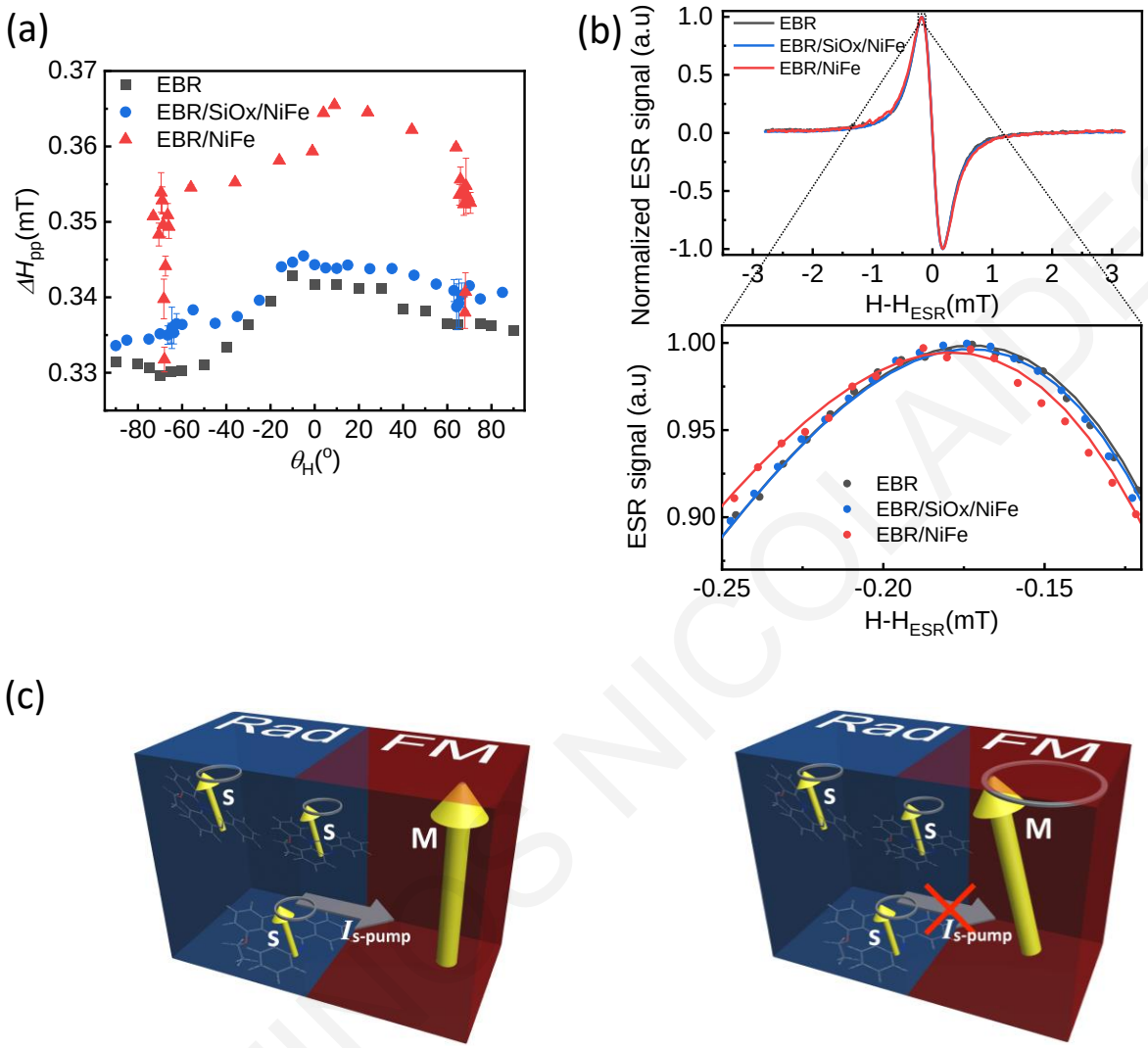

Figure 8.4: (a) The magnetic field angle, θ_H, dependence of the ESR linewidth, ΔH_{pp}, for the EBR thin film the EBR/SiOx/NiFe trilayer and the EBR/NiFe bilayer. (b) Normalized ESR spectra at $\theta_H = 0^o$, of the pristine EBR film, the EBR/SiOx/NiFe trilayer and the EBR/NiFe bilayer. The figure below shows the magnified region of the experimental results around the peak clarifying the shift due to the increase in linewidth while the solid lines are fits to the data, given by a Lorentzian function.(c) Schematic of spin pumping procedure in a radical/ferromagnet (Rad/FM) bilayer. When the EBR layer is at resonance it pumps a spin current, I_{s-pump}, into the NiFe layer which is detuned from its FMR (left). For simultaneous resonance of the radical and the ferromagnet the magnitude of I_{s-pump} is cancelled by an opposite spin current from the FM layer(right).

can be attributed to an in-phase coherent precession of the radical and the NiFe (Figure 8.4.c) and a consequent emission of counter-propagating in-phase spin currents. When the EBR film is in resonance alone it emits a spin current via spin pumping into the NiFe and its linewidth is enhanced (Figure 8.4.c, left). For simultaneous resonance the EBR film emits and simultaneously receives the spin current emitted by the NiFe layer through their interface. The former is causing an increase of ΔH_{pp} while the latter a decrease, eliminating the enhancement in the linewidth due to spin pumping (Figure 8.4.c, right). In order to support the explanation of spin pumping a control measurement was carried out by inserting a SiOx layer between the EBR and the NiFe layer, to act as a spin blocker. The results in Fig.8.4.c, show no enhancement in the linewidth when the ESR and FMR resonances do not coincide. Furthermore, there is no linewidth decrease when the two resonances coincide. Figure 8.4.b shows typical ESR spectra of the EBR spectra of the EBR, EBR/SiOx/NiFe and EBR/NiFe samples. The linewidth of the latter is clearly different from the others as expected for the organic radical acting as spin source into the NiFe spin sink.

Another consequence of the simultaneous ESR and FMR resonance is the observed decrease of the g-factor (Figure B.2) associated with a corresponding shift of the resonance field in the ESR spectra. A similar shift in the resonance field near simultaneous resonance is reported for coupled ferromagnetic bilayers [241, 243] due to a fieldlike torque acting along or against the Larmor precession, with possible contributions from both interfacial exchange coupling [241, 243] and spin current transport [243]. Accordingly, the g-factor decrease at $\theta_H \approx \pm 68^o$ can be qualitatively understood in the context of a similar macrospin model where the incoming spin current from the NiFe layer, can cause the resulting fieldlike term which acts as an effective field or equivalently a shift in the g-factor.

The successful emission of spin current from the EBR indicates the possibility of realizing spin pumping even in the absence of long range ferromagnetic order.Further evidence towards this possibility is the successful observation of spin pumping from a crystalline inorganic paramagnet, showing the same relative change in linewidth ($\sim 10\%$) as in the present study [218], together with a theoretical description for spin pumping from a fluctuating ferromagnet near Tc [221]. A generalization of the spin

pumping theory is required beyond systems with long range ferromagnetic order and in particular for the case of organic radicals.

In conclusion, we have demonstrated spin current creation via spin pumping from a purely organic radical following the successful fabrication of stable radical films at room temperature. The spin resonance linewidth and the g-factor can be dynamically controlled via absorption by the radical film of a spin current emitted from a nearby ferromagnet. The present study illustrates the potential of organic radicals to act as spin sources in future spintronic devices.

Chapter 9

Spin pumping across hybrid organic-inorganic perovskite / ferromagnet interface: the effect of ferromagnet morphology

9.1 Introduction

In this chapter, which is based to ref [128] , we aim to elucidate the influence of the morphology of a ferromagnetic film on the spin pumping process. By preparing a series of $CH_3NH_3PbI_{3-x}Cl_x/NiFe$ heterostructure where the NiFe is grown at various thickness directly on the perovskite material we observe differentiation of the morphology which affect the ability of spin transfer to the $CH_3NH_3PbI_{3-x}Cl_x$ layer.

Organic-inorganic hybrid perovskites (OIHPs), such as $CH_3NH_3PbI_{3-x}Cl_x$, have been heavily studied recently as exceptional next generation solar cell candidate materials, reaching certified power conversion efficiency above 25 % in only a few years [169]. Recently, OIHPs have drawn great attention also from the field of spintronics. The presence of heavy elements (Pb, I) in the chemical composition of these compounds, suggests possible existence of large spin-orbit coupling (SOC). Indeed, this assumption was examined through theoretical calculations which predicted the dramatic change of

the band structure for OIHPs due to strong SOC [174,245]. This prediction was verified through circular pump-probe measurements which demonstrate highly spin polarized electrons with an initial degree of polarization $\sim 90\%$ [175]. As a semiconductor with excellent optoelectronic and spin dependent optical selection rules comparable with the most famous direct gap inorganic semiconductor, $GaAs$, OIHPs are very promising materials for future spintronics applications.

One of the most prominent method to study spin dependent phenomena in OIHPs, as well as solution processed organic materials has been via their contact with a ferromagnet, e.g. in OIHP/ferromagnet interfaces. The presence of the ferromagnetic material enables the efficient injection of spin currents through FMR spin pumping [92, 200]. Orbital hybridization at an interface of a ferromagnet and a non-magnetic semiconductor [246], forming the so-called spinterface, plays a decisive role in spin dependent measurements in OIHP/ferromagnet bilayers [246]. The formation of spinterfaces in $CH_3NH_3PbI_{3-x}Cl_x/Ni$ and $CH_3NH_3PbI_{3-x}Cl_x/Co$ heterostructures were shown to greatly influence magnetoresistance [247, 248] and magnetodielectric response [249], respectively. In addition, the presence of strong SOC in OIHPs coupled with inversion symmetry breaking in these materials, leads to other interface effects such as Rashba coupling [178, 250, 251], which affects the spin properties of OIHPs by causing outstanding spin transport [252], enhanced spin current to charge current conversion efficiency [253] and long spin relaxation time at room temperature [200]. Hence, the presence of a ferromagnetic layer together with an OIHP layer is of great interest, in terms of understanding spin dependent phenomena and the interaction between the two and the effect of interface properties remains elusive and needs further investigation.

A common way to inject spin current into a non-magnetic layer is through spin pumping under ferromagnetic resonance (FMR) which requires the presence of a ferromagnetic film. The efficiency of the process is determined through the spin mixing parameter, $g^{\uparrow\downarrow}$, and it is quite sensitive on the interface quality. Especially, when a ferromagnet is evaporated onto an OIHP layer, the ferromagnet morphology could have an influence on the spin pumping process. In this context, we present an experimental demonstration of spin transport at room temperature in solution processed $CH_3NH_3PbI_{3-x}Cl_x$ films by spin pumping in a microwave cavity for a

series of $CH_3NH_3PbI_{3-x}Cl_x/NiFe$ heterostructures with varying NiFe thicknesses. By systematically increasing its thickness, the deposited NiFe layer transitions from island growth to percolation and finally to the formation of a uniform film of lower roughness. By taking into account the different contributions to the observed linewidth broadening due to the evolution of the magnetic film morphology we isolate the spin absorption contribution, which is parameterized by the $g^{\uparrow\downarrow}$, which shows a significant increase as the NiFe tends to a continuous film. This result demonstrates the importance of interface properties on spin dependent phenomena and could have wider implications in the field of spintronics in solution processed materials.

9.2 Experimental procedure

The experiments presented in this study were performed on a series of $SiO_x/CH_3NH_3PbI_{3-x}Cl_x/NiFe$ bilayer samples. The perovskite film was fabricated on a glass substrate using a solution of $MAI : PbCl_2$ (3:1 molar ratio) by using a procedure which is already described at section 6.7.4. A $Ni_{81}Fe_{19}$ layer was subsequently deposited using e-beam evaporation in a molecular beam epitaxy system with a base pressure of $8 \times 10^{-8} mbar$ and a deposition rate of $0.3 \mathring{A}/min$ at room temperature. A series of NiFe layers was created with nominal deposition thicknesses of 4, 5, 6, 8, 10, 13, 20 nm (labeled as PN1, PN2, PN3, PN4, PN5, PN6 and PN7, respectively) in a single growth run. The layers were patterned using metal shadow masks to result in $3.0 \times 1.5 mm^2$ samples for each NiFe thickness. For comparison, we fabricated identical NiFe samples without the OIHP on SiO_x substrates.

9.3 Spin pumping in a $CH_3NH_3PbI_{3-x}Cl_x/NiFe$ heterostructure

As already has been noted, $CH_3NH_3PbI_{3-x}Cl_x$ is a material characterized by strong SOC which makes it a good candidate for spintronic applications. The creation of pure spin currents in such materials in order to study spin dependent phenomena can be achieved via different methods [28, 175, 176, 252]. In the present study we have

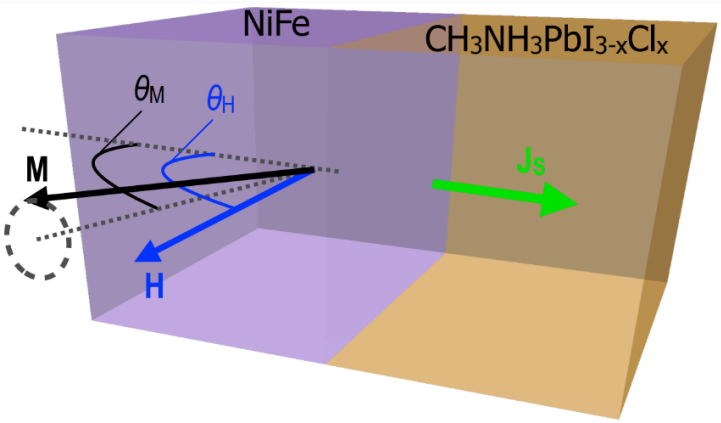

Figure 9.1: Schematic representation of spin pumping method for the $CH_3NH_3PbI_{3-x}Cl_x/NiFe$ interface.

used spin pumping via FMR, which enables creation of spin currents by a precessing magnetization at resonance (for more info see Section 4.3). It can be viewed as a source of pure spin current which decreases away from the interface into the non-magnetic material due to spin relaxation and diffusion. In the scattering theory of spin pumping [86, 233] the magnetization precession causes a spin current flowing through the interface to a nearby material given by

$$\overrightarrow{J_{s,pump}} = \frac{\hbar}{4\pi} g^{\uparrow\downarrow} \overrightarrow{m} \times \frac{d\overrightarrow{m}}{dt}, \tag{9.1}$$

where $\hbar$, $g^{\uparrow\downarrow}$, $\overrightarrow{m}$ are the Planck constant, the real part of the spin mixing conductance and the unit vector of the magnetization. The ability to transmit spin angular momentum through an interface is expressed by the spin mixing conductance and its value depends on the materials and is sensitive to interface properties. It represents the number of spin transmission channels per unit surface area in the interface between ferromagnet and non-magnet and is given by the expression [86, 254]

$$g^{\uparrow\downarrow} = \frac{4\pi M_{eff} t_F}{g\mu_B} (\alpha_{NM/FM} - \alpha_{FM}). \tag{9.2}$$

Here g corresponds to the g-factor, μ_B to the Bohr magneton, M_{eff} to the saturation magnetization, t_F to the ferromagnet's thickness and $\alpha_{NM/FM}$, α_{FM} are the damping terms for the nonmagnet (NM)/ ferromagnet(FM) bilayer and the single FM layer, respectively.

The FMR measurements are carried out by placing each of the $CH_3NH_3PbI_{3-x}Cl_x/NiFe$ heterostructures at the center of a rectangular TE_{102}

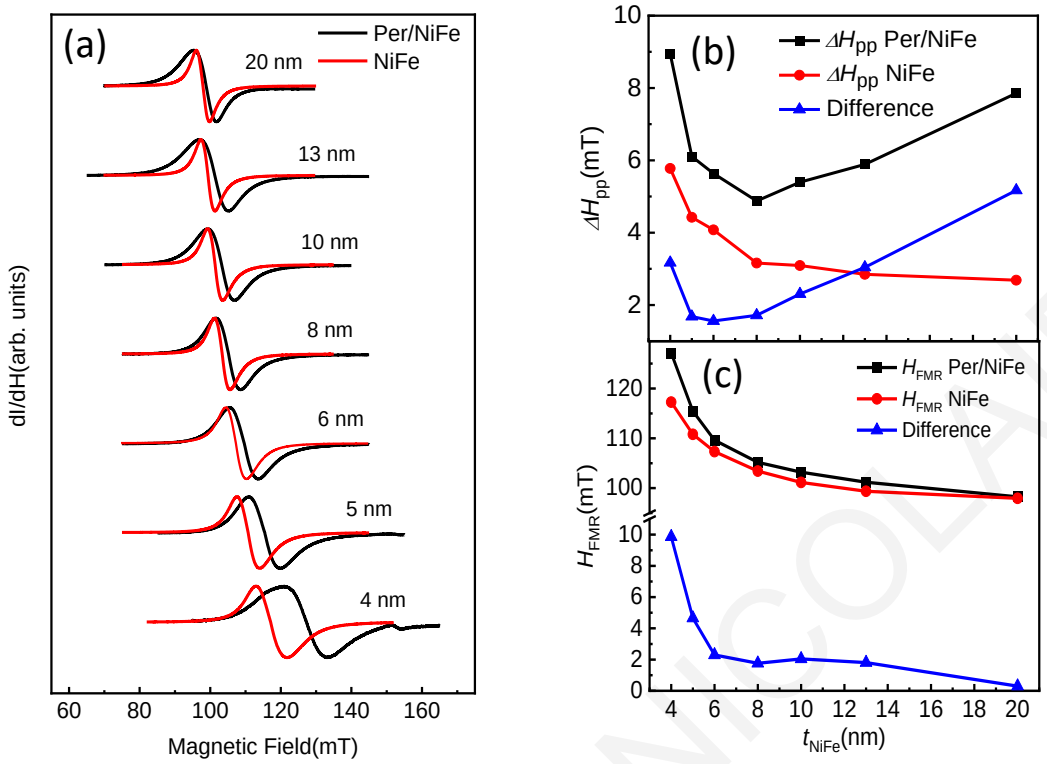

Figure 9.2: (a)FMR spectra of $CH_3NH_3PbI_{3-x}Cl_x/NiFe$ and $NiFe$ single layer films spectra at $\theta_H = 90^o$ for seven different NiFe deposition thicknesses ($t_{NiFe} = 4nm, 5nm, 6nm, 8nm, 10nm, 13nm, 20nm$). (b) Linewidth ($\Delta H_{pp}$) as a function of NiFe thickness. (c) Ferromagnetic resonance magnetic field (H_{FMR}) as a function of NiFe thickness.

microwave cavity with a frequency $f = 9.43\ GHz$ (Section 6.1.1). An external magnetic field, H, is applied at an angle θ_H to the normal of the ferromagnetic film plane (Figure 9.1). θ_M denotes the angle between the magnetization of the NiFe layer and the film normal. When H and f fulfill the FMR condition a pure spin current with a spin-polarization $\overrightarrow{\sigma}$ parallel to θ_M is injected into the perovskite layer by spin pumping, which results in an additional broadening of the spectral width of the ferromagnet [82].

Figure 9.2.a shows a comparison of the in plane ($\theta_H = 90^o$) FMR spectra for $CH_3NH_3PbI_{3-x}Cl_x/NiFe$ and single $NiFe$ structures for seven different $NiFe$ deposition thicknesses ($t_{NiFe} = 4, 5, 6, 8, 10, 13, 20nm$). It is clear that the spectral width, ΔH_{pp}, is enhanced in the bilayers for all ferromagnet deposition thicknesses.

As illustrated in Figure 9.2.b , the linewidth of $CH_3NH_3PbI_{3-x}Cl_x/NiFe$ heterostructures decreases with $NiFe$ thickness up to $8nm$ and then it increases for higher thicknesses. On the contrary, ΔH_{pp} corresponding to $NiFe$ layer shows a monotonic reduction as a function of ferromagnetic deposition thickness. As a result, the linewidth enhancement between the bilayer and the single layer structures is seen to decrease for small thicknesses and then follows a three-fold increment up to $20nm$ (Figure 9.2.b). Furthermore, a rapid monotonic reduction is observed in the ferromagnetic resonance field (H_{FMR}) as a function of t_{NiFe} for both bilayers and single layers (Figure 9.2.c). Note that the resonance field difference is also decreasing, effectively approaching zero for large thicknesses where the resonance fields tend to the same value.

9.4 AFM and MOKE measurements

In order to understand the above behavior in the FMR spectra and its implications on spin pumping, we have further investigated possible contributions to the linewidth due to morphology and interfacial effects by carrying out atomic force microscopy (AFM) (Section 6.4) and magneto-optical Kerr effect (MOKE) measurements (Section 6.3). Figures 9.3a-9.3g display AFM images of the evolution of the NiFe film morphology, as a function of the nominal film thickness, taken at the top of a typical perovskite's grain. We can identify three distinguishable regimes. Initially, for $4nm \leq t_{NiFe} < 8nm$ (Figures 9.3a, 9.3b), an island growth regime, where the film morphology consists of compact isolated islands. Then, for $8nm \leq t_{NiFe} \leq 13nm$ (Figures 9.3c-9.3f) the island coalescence regime, where islands merge, resulting in elongated structures. As the t_{NiFe} increases the lateral dimensions of these structures are getting bigger and some them are linked, forming worm-like grains. Eventually a thin continuous film is formed at the island's base while the island's height is reduced (Figure 9.3h). Finally, for $t_{NiFe} \leq 20nm$ (Figure 9.3g) a continuous film regime is obtained, where the island structure is shrank and perovskite layer is completely covered by NiFe film with thickness almost equal with the expected NiFe deposition thickness (Figure 9.3h).

The MOKE measurements for each sample are shown in Figure 9.4a with

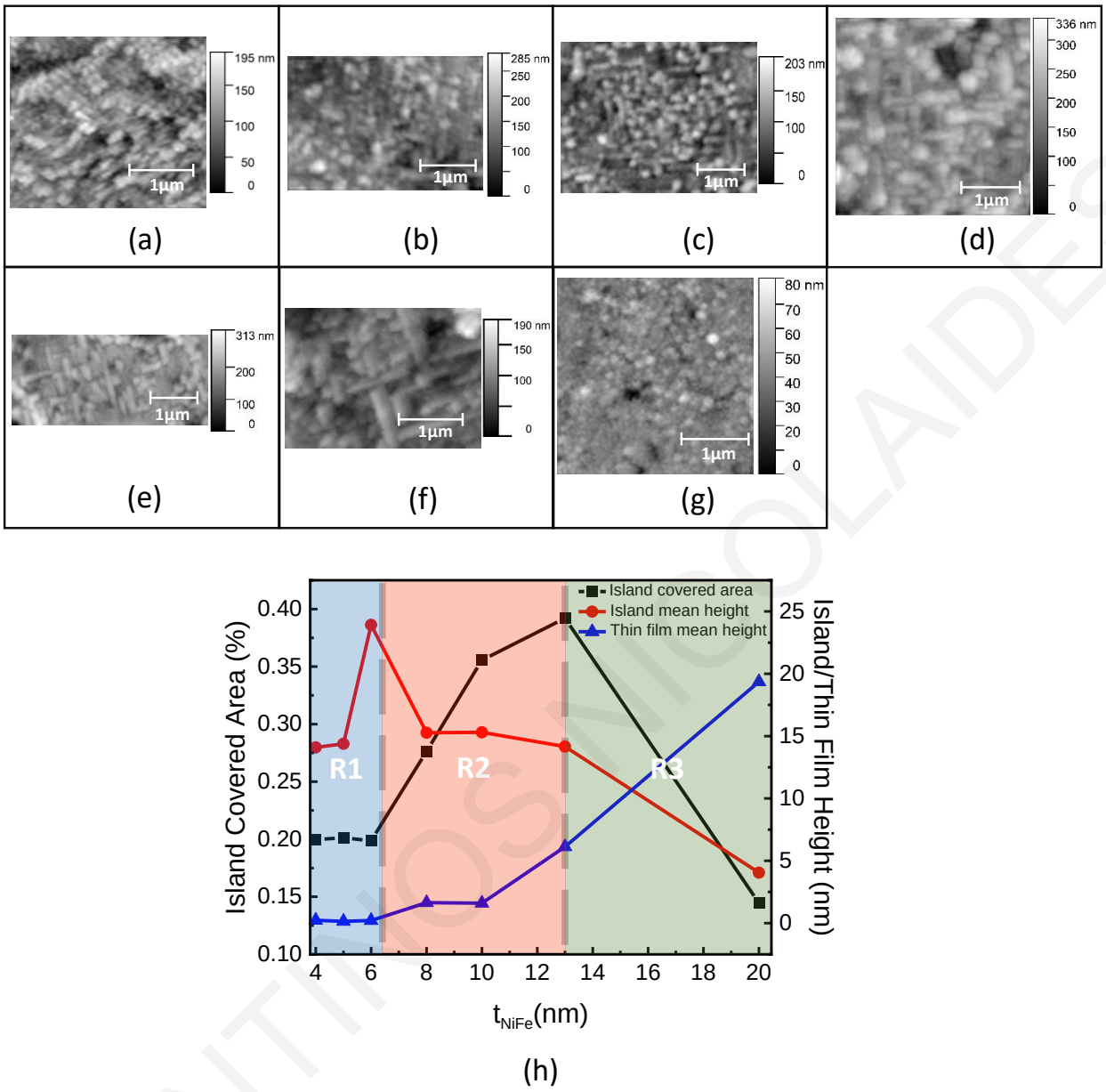

Figure 9.3: AFM images of the evolution of NiFe film morphology as a function of the film thickness (a) $t_{NiFe} = 4nm$, (b) $t_{NiFe} = 5nm$, (c) $t_{NiFe} = 6nm$, (d) $t_{NiFe} = 8nm$, (e) $t_{NiFe} = 10nm$, (f) $t_{NiFe} = 13nm$, (g) $t_{NiFe} = 20nm$. (h) Calculation of island covered area, island mean height and thin film mean height as a function of t_{NiFe} through which the evolution of NiFe film morphology has been divided into three regimes, island growth (R1), island coalescence (R2) and the continuous film regime (R3).

the extracted coercivity, H_c, in Figure 9.4b. A sharp increase is observed in the coercivity for $4nm \leq t_{NiFe} \leq 10nm$ followed by a gradual reduction above $10nm$. These results are consistent with the topography information obtained by

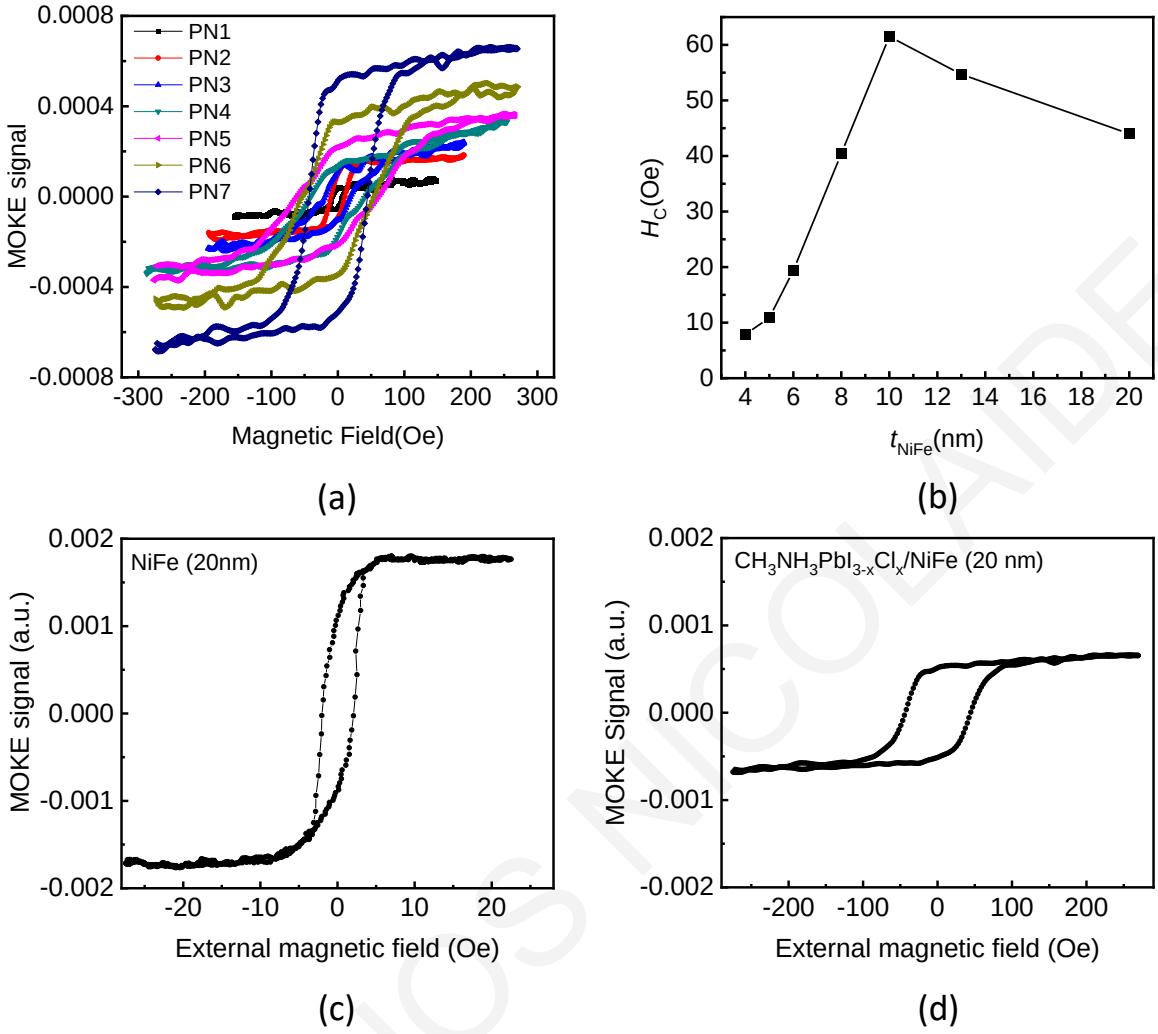

Figure 9.4: (a) MOKE measurement of $CH_3NH_3PbI_{3-x}Cl_x/NiFe$ interface for every t_{NiFe}, (b) Coercivity (H_c) as a function of t_{NiFe}.(c-d) MOKE hysteresis loops measured at room temperature for 20 nm thick (c) pristine NiFe thin film and (d) $CH_3NH_3PbI_{3-x}Cl_x/NiFe$ bilayer.

AFM [255, 256]. We suggest that compact and elongated islands ($4nm \leq t_{NiFe} \leq 8nm$) of sizes in the range $70 - 100nm$ behave as single domain particles and their coercivity depends on the single domain island's diameter, D, and follows a power law, $H_c \propto D^n$, where n depends on the mechanism of magnetization reversal [257] ($n \sim 3 - 6$). This explains the sharp increase of the coercivity for small thicknesses. For larger elongated islands ($8nm \leq t_{NiFe} \leq 13nm$) we expect te formation of domain walls. Their movement by the applied external magnetic field is impeded by pinning at the contact points between the elongated islands resulting in a further increase in coercivity as we can see at $t_{NiFe} = 10nm$. When $t_{NiFe} = 13nm$ the contact area between islands increases effectively presenting weaker pinning sites for

domain walls and therefore a small reduction of coercivity [258]. Finally, in the continuous film regime ($t_{NiFe} = 20nm$), a multidomain film is formed and the coercivity is expected to decrease rapidly as t_{NiFe} increases [255, 256, 259] as seen in our measurement. It is worth noting the remarkable enhancement in coercivity of the $CH_3NH_3PbI_{3-x}Cl_x/NiFe(20nm)$ bilayer ($H_c = 44Oe$) in comparison with the bare NiFe (20 nm) film ($H_c = 2.1Oe$) (Figures 9.4c, 9.4d) which in combination with reduced magnetic moment (Figures 9.4c, 9.4d) demonstrates magnetic hardening indicating the creation of a spinterface [247, 260]. Similar interactions at the interface between ferromagnet and perovskite layers have already been reported [247, 249]. Especially in the case where the ferromagnet is deposited on top of a spin coated perovskite film the effect of the interaction is maximized [247, 249], resulting in substantial coercivity enhancement.

9.5 Discussion

The AFM data indicates a typical thickness dependent surface morphology evolution during deposition of thin-metal films on non-metallic substrates [261–263]. Together with the MOKE results, they demonstrate the transition from island growth to percolation and finally formation of a multidomain NiFe thin film. The evolution of the NiFe film morphology is also reflected in FMR measurements through the associated change in the ferromagnetic resonance field, H_{FMR}. The island growth during the NiFe deposition on the perovskite layer causes a shift in the H_{FMR} (Figure 9.2.c), compared to that of a NiFe thin film due to weak inter-island dipolar interaction [264] contributing to the local effective field. As the island's filling factor grows the inter-island spacing is diminished resulting in an enhancement of magnetic dipolar interaction [264, 265]. For the case of $t_{NiFe} = 20nm$ the creation of multidomain continuous NiFe thin film is confirmed, since the ferromagnetic resonance field of the $CH_3NH_3PbI_{3-x}Cl_x/NiFe(20nm)$ film and $NiFe(20nm)$ are almost equal. Figure 9.5 shows the H_{FMR} dependence on the out-of-plane angle (θ_H) of the external magnetic field for all $CH_3NH_3PbI_{3-x}Cl_x/NiFe$ samples. We observe that they display the same behavior as thin films. If the distance between the magnetic islands is comparable with their sizes, the dipole-dipole interaction couples the magnetization of different islands and as a result the whole granular ferromagnetic sample behaves as a continuous

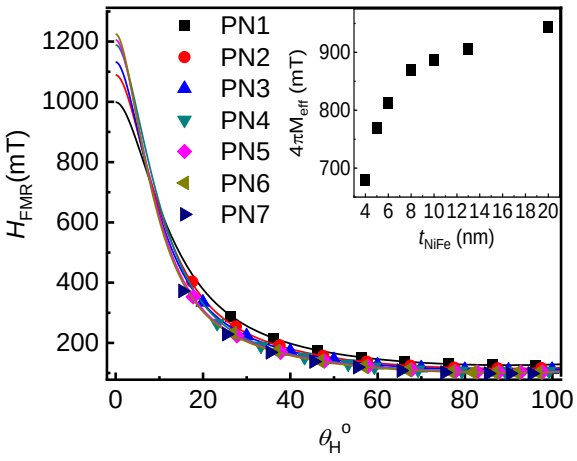

Figure 9.5: Dependence of ferromagnetic resonance field H_{FMR} on the applied field angle, θ_H, with increasing t_{NiFe}. The solid lines are fitted curves to the experimental data (solid points).

film even without direct contact between the islands [264, 266]. Consequently, for ferromagnetic resonance of our granular system we use the common resonance condition of continuous thin films [92, 267]

$$\left(\frac{\omega}{\gamma}\right)^2 = [H_{FMR}cos(\theta_H - \theta_M) - 4\pi M_{eff}cos2\theta_M] \times [H_{FMR}cos(\theta_H - \theta_M) - 4\pi M_{eff}cos^2\theta_M], \tag{9.3}$$

where M_{eff} corresponds to the effective saturation magnetization for each morphology estimated by fitting equation, which fits H_{FMR} as a function of θ_H for each sample (inset of Figure 9.5). In order to interpret the behavior of $CH_3NH_3PbI_{3-x}Cl_x/NiFe$ heterostructure linewidth, ΔH_{pp}, as a function of NiFe deposition thickness and calculate the spin pumping contribution, we have to take into consideration the possible contribution of different magnetic relaxation mechanisms. In general, it is well known that except of intrinsic Gilbert-type mechanisms, linewidth may be broadened by extrinsic non-Gilbert-type mechanisms which have as main representatives two-magnon scattering (Section 4.2.1) and inhomogeneity (Section 4.2.2). Two-magnon scattering appears on magnetic systems characterized by strong exchange and dipolar interactions and it is a process where a uniform magnon with $q = 0$ scatters into degenerate states of magnons with $q \neq 0$ due to defects or imperfections on the surface of magnetic films which act as scattering centers [64, 71, 75, 76, 268]. On the other hand, the inhomogeneity contribution to the linewidth arises from a wide variety of microstructural film origins, most importantly,

$t_{NiFe}(nm)$	$4\pi M_{eff}(mT)$	$\alpha_{Per/NiFe}$	α_{NiFe}	Δ_{θ_H}	$g^{\uparrow\downarrow}(m^{-2})$
4	679.8	0.0193	0.0147	0.0217	4.84×10^{18}
5	770.1	0.0150	0.0119	0.0106	3.62×10^{18}
6	813.3	0.0143	0.0114	0.0082	5.99×10^{18}
8	869.9	0.0135	0.0088	0.0093	1.22×10^{19}
10	886.6	0.0154	0.0091	0.0087	2.03×10^{19}
13	906	0.0173	0.0085	0.0096	4.74×10^{19}
20	943.7	0.0235	0.0081	0.0147	1.48×10^{20}

Table 9.1: Parameters obtained from theoretical fitting.

the non-homogeneous distribution of the demagnetizing field due to the film morphology and the spread in the alignment of crystallographic axes leading to a distribution in the magnetocrystalline anisotropy [268–273]. Consequently, the total linewidth is the sum of the three magnetic relaxation mechanisms,

$$\Delta H_{tot} = \Delta H_{intr} + \Delta H_{2mag} + \Delta H_{inhom}. \tag{9.4}$$

The first term represents the intrinsic linewidth due to Gilbert damping and its out-of-plane external magnetic field angle dependence can be written as [54, 268, 274]

$$\Delta H_{intr} = \frac{2\alpha}{\sqrt{3}\Xi}\frac{\omega}{\gamma}, \tag{9.5}$$

where α represents the damping parameter. The parameter Ξ corresponds to the dragging function (defined at equation C.3 in Appendix C.1) reflecting the enhancement in the Gilbert damping when the applied field direction is not aligned with the equilibrium magnetization direction, defined by θ_M [268]. ΔH_{2mag}, corresponds to the linewidth contribution arising from the two-magnon scattering mechanism induced by surface defects, and its specific formula is given in the Appendix C.1 (Equations C.1, C.2). Finally, the inhomogeneous linewidth enhancement, ΔH_{inhom}, can be expressed as [82, 275]

$$\Delta H_{inhom} = \left|\frac{\partial H_{FMR}}{\partial \theta_H}\right|\Delta_{\theta_H} + \left|\frac{\partial H_{FMR}}{\partial 4\pi M_{eff}}\right|\Delta_{4\pi M_{eff}}, \tag{9.6}$$

where Δ_{θ_H} represents the angular spread of the crystallographic axis between different magnetic grains and $\Delta_{4\pi M_{eff}}$ the distribution of the local demagnetization field.

Figures 9.6.a-9.6.g show the dependence of the FMR linewidth on the external magnetic field angle, θ_H, for increasing NiFe deposition thickness

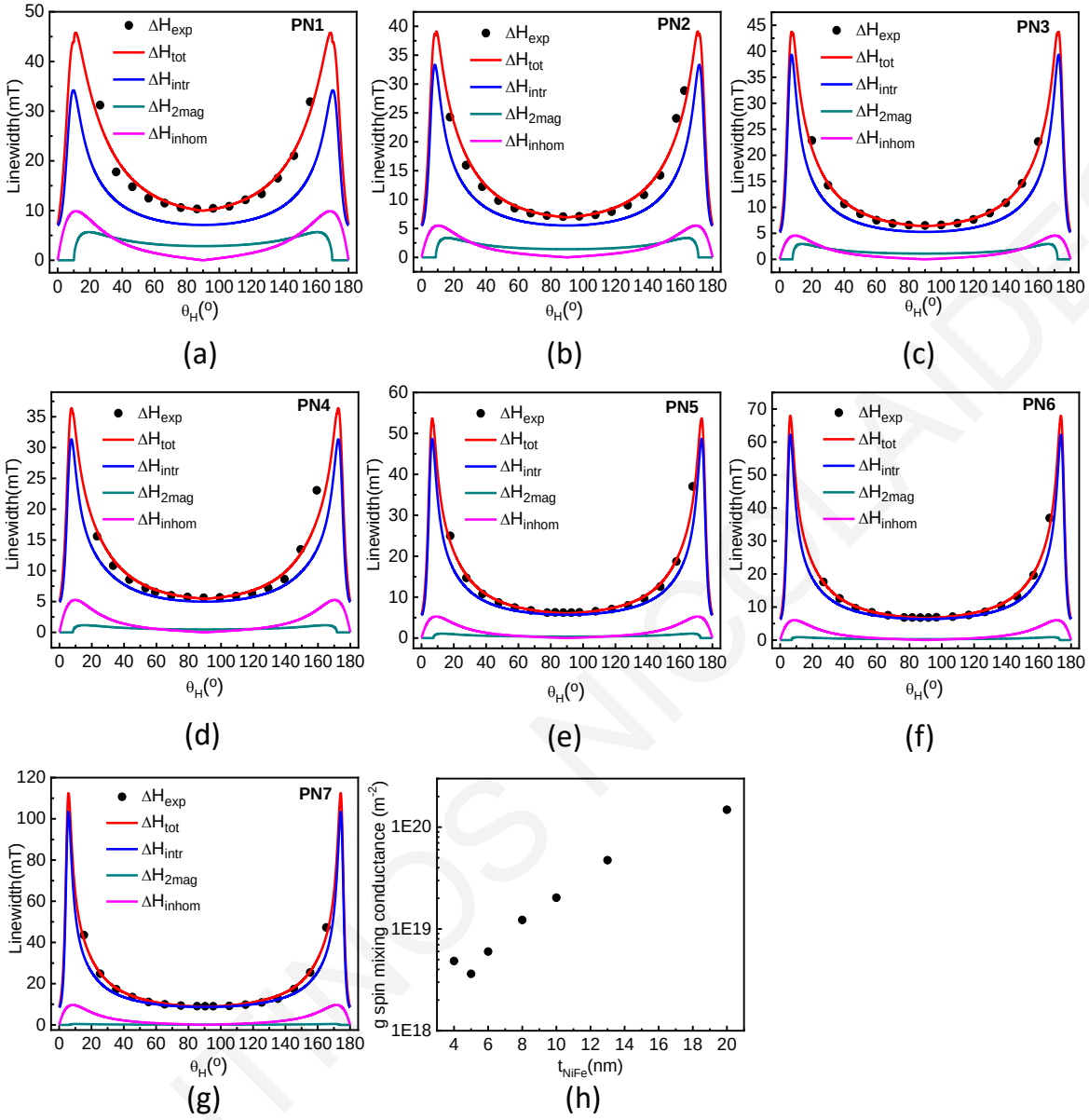

Figure 9.6: (a)-(g) Angular dependence of different linewidth contributions on the out-of plane orientation θ_H with increasing t_{NiFe}. (h) Spin mixing conductance parameter as a function of t_{NiFe}

accompanied by the fitting curves of equations 9.4-9.6 (for further details about the fitting procedure see Appendix C.1). For all samples, the main linewidth contribution is attributed to the intrinsic linewidth part, ΔH_{intr}, (note the overall shape of the experimental data is very close to that of the intrinsic contribution). We observe that ΔH_{2mag} is seen to decreases monotonically as a function of NiFe deposition thickness, as expected for a process arising at interface (edge defect induced scattering) and also from the corresponding suppression of the surface magnetic field, (H_s) (Eqs. C.1, C.2). Furthermore, according to our fitting results the $\Delta_{4\pi M_{eff}}$ term is negligible for

all samples and the inhomogeneity linewidth is due to the first term of equation 9.6. Δ_{θ_H} is shown in Table 9.1 and we note that for $4nm \leq t_{NiFe} \leq 10nm$, it decreases and remains roughly constant for higher thicknesses. Considering the morphology evolution with thickness in our samples, we expect a gradual decrease of the inhomogeneity contribution during the transition from island growth to a formation of a thin film which is associated with suppression of inhomogeneous regions. After accounting for all different contributions to the linewidth, we concentrate on the fitted ΔH_{intr} curve and extract the damping term, $\alpha_{Per/NiFe}$, for all $CH_3NH_3PbI_{3-x}Cl_x/NiFe$ heterostructures together with α_{NiFe} for NiFe single layers (Table 9.1). We can then calculate the spin mixing conductance parameter, $g^{\uparrow\downarrow}$, using equation 9.2 for every NiFe deposition thickness. As shown in Figure 9.6.h, $g^{\uparrow\downarrow}$ is roughly constant for $4nm \leq t_{NiFe} \leq 6nm$ then, followed by rapid increase as a function of t_{NiFe}. For $t_{NiFe} = 20nm$ the spin mixing conductance is estimated $g^{\uparrow\downarrow} = 1.48 \times 10^{20} m^{-2}$, a relatively large value, proving the efficient spin transport into the perovskite and its suitability as a high spin sink spintronic material. This is indicative of the expected presence of a strong spin to charge conversion process caused by the simultaneous existence of a surface-dominated component due to Rashba splitting and a traditional bulk spin to charge conversion due to SOC [200, 253]. Since the spin mixing conductance refers to the efficiency of spin current generation that depends on interface properties, the dramatic change of $g^{\uparrow\downarrow}$ illustrates the importance of taking into account the properties of such interfaces both for the interpretation of spin dependent phenomena and the design of future spintronic devices.

Chapter 10

Conclusions - Future Work

Understanding the physics of spin current has always been one of the fundamental purposes for the field of spintronics. Accordingly, the studies that have been presented in this thesis share as a common goal, the investigation of injection, manipulation and detection from and to solution processed materials and the revealing of the factors that affect the propagation of spin information. This was accomplished by using solution-processed-material / metallic-ferromagnet bilayers by exploiting spin pumping. The findings of this thesis motivate us for further studies with an ulterior purpose to create purely organic spintronic devices.

- **Chapter 7:Effect of structural conformation of conjugated polymers on spin transport.**

Spin transport in organic semiconductors has long been a subject of discussion, since there were experimental reports with unexpectedly high SOC strength, followed by measurements with widely varying values of spin diffusion length in materials with similar chemical structure [32, 39]. The link between the conformation of the polymer and the strength of its SOC has been suggested as a possible explanation. In this context, we estimate the spin diffusion length and the spin admixture parameter, γ^2, of the prototype system PEDOT:PSS at different polymer backbone conformations induced by chemical doping. The spin diffusion length obtained, varies from 154 nm to 275 nm with increasing dedoping while by taking into account the contributions of hopping as well as exchange on spin

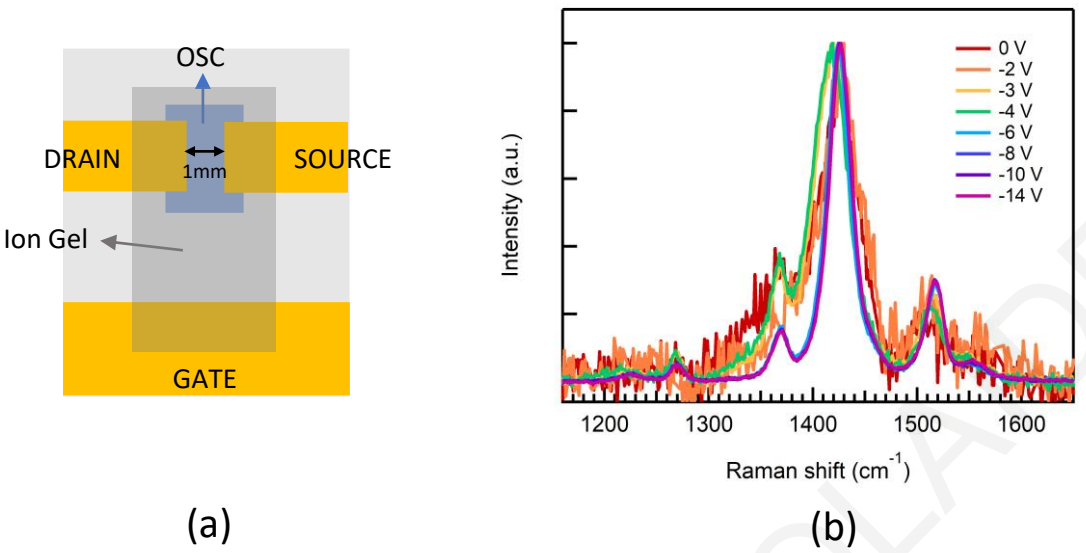

Figure 10.1: (a)Schematic illustration of a top contact side-gate geometry for electrolyte-gating with an ion-gel on a spin coated film of OSC (top view). (b)Normalized resonance Raman spectra of PEDOT:PSS upon electrochemical reduction (dedoping) by using different electrochemical voltage difference, V_G, and with excitation at 532 nm.

transport, we estimated a gradual reduction of the γ^2 by one order of magnitude and therefore an associated SOC strength reduction. A similar trend is observed in a separate set of experiments in the spin Hall angle, θ_{SH}, estimated via ISHE measurements induced by FMR spin pumping. Since the chemical composition of the organic semiconductor remains the same during the doping procedure, we attribute the change of the SOC strength to the alteration of the structural conformation of the polymer. This is confirmed through resonance Raman spectroscopy with the predominance of the more planar quinoid structure at lower doping levels, indicating that enhanced planarity is associated with SOC strength reduction. Our results offer a new way to manipulate spin phenomena via controlling the structural conformation in conjucated polymers through chemical doping, and it can be used for future spin transport studies in these materials as well as to enhance functionality in spintronic devices.

We plan to extent this project by examining systematically the effect of conjugated polymer backbone conformation on SOC strength. We are going to use electrochemical doping of a series of polythiophene based OSCs (PEDOT, P3HT or

PBTTT) to induce a systematic degree of control of the conformation and study the effect of the latter on spin transport. Electrochemical doping provides the advantage of easily accessing larger range of doping levels on a single polymer film, avoiding thus any sample-to-sample variation present with other means of doping such as, chemical or molecular doping. A side-gate arrangement will be used for the electrolyte-gated transistor (Figure 10.1.a) where the electrolyte ion-gel will be spin coated out of a solution over the active area, while the doping procedure is controlled via the electrochemical voltage difference (V_G). The relevant transistor devices have already been fabricated and some preliminary resonance Raman electrochemical measurements of a spin-coated PEDOT:PSS film were carried out (Figure 10.1.b) with excitation at 532 nm. The results agree with the corresponding behavior of Raman spectra during chemical doping and/or dedoping (Section 7.5). We can then proceed with the proposed project which combines a number of spin and electrical measurements such as ESR, ISHE e.t.c at various doping levels with direct structural characterization of the conjucated polymers using resonance Raman spectroscopy. Our ultimate goal is to establish a pathway for electrically controlled spin phenomena in these systems.

- **Chapter 8:Metal-free organic radical spin source.**

In this study the emission of spin current from an all-organic radical that can act as a spin source has been reported. The majority of spintronic studies in organic materials rely on conventional metallic or insulating ferromagnets as a source or detector of spin. The search for an all-organic replacement and for organic magnets in general, is a particularly active research area, while organic radicals have long been suggested as candidates for organic magnets and components in organic spintronic devices.

Here, we demonstrated that a metal-free all organic radical can fulfill the role of spin emitter without the need to be in a ferromagnetic state. More specifically, we fabricated a stable Blatter-type radical/NiFe bilayer and carried out simultaneous ESR and FMR measurements. A signature of spin current emission from the radical was obtained through its increased linewidth. By carefully tuning the two resonances to coincide we demonstrated that the radical linewidth increase can be reversibly reduced due to emission of a backward spin current from the FM layer, effectively canceling the

radical's emission. We used a standard Blatter radical in this work, slightly modified to improve its film forming ability.

In principle, the work reported could be applicable to other organic radicals and enable their use as spin sources for a variety of future spintronics studies and device concepts. The results are also important from a fundamental perspective, related to the spin pumping mechanism and its versatility as a tool for creating spin currents. Spin pumping is shown to be applicable to yet another wide class of materials, organic radical systems, beyond the conventional ferromagnets. This could spark further interest in the spintronics community to expand spin pumping theory to include radical systems.

More generally, the results of this study will significantly impact several scientific areas from the community studying radicals - synthesis and physical properties - since it opens a new application area for these molecules, to the community studying organic spintronics as a new source of spin current has been opening a new avenue for the development of purely organic spintronic devices. This simultaneously raises questions regarding the spin pumping mechanism in the absence of ferromagnetic order and the dominant spin transport mechanisms into these radical systems. In this context, we intend to be actively involved in the formation of this new field. As a first step, we plan to extent our published research via the fabrication of a series of Blatter-radical / non-magnetic (NM) bilayers, where the NM's SOC strength will be varied. The radical's linewidth enhancement will be recorded and if the variation in the spectral broadening corresponds to that of the NM's SOC strength, this will be another proof that radical layer can operate as a source of spin current via spin pumping. Another evidence of successful spin current injection from Blatter radical layer can be derived by the ISHE voltage measurement under ESR condition. More specifically, we plan to build a Blatter radical/Pt bilayer and detect an ISHE votage under ESR conditions. Moreover, we would like to investigate fundamental properties for a variety of different Blatter radical structures and classify them in terms of the SOC strength, the conductivity and the film forming ability. This would guide us to the appropriate choice in order to investigate the possibility of using Blatter radical as a spin sink layer, where spin injection will be carried out through a common FM. Finally, the accomplishment of the previous studies will enable us to examine the mechanism that mediates spin transport in

Blatter radical via a common FM/Blatter radical/Pt trilayer. Ideally, ISHE voltage measurement will be detected under FMR and ESR conditions separately. By carefully tuning the two resonances to coincide, the ISHE voltage that we will receive, will give us important information about the spin transport mechanism.

- **Chapter 9:Spin pumping across hybrid organic-inorganic perovskite / ferromagnet interface: the effect of ferromagnetic morphology.**

In the present study we focus on the influence of the ferromagnet's morphology on the spin pumping process and out of plane angular dependent FMR was used to study the spin pumping in a $CH_3NH_3PbI_{3-x}Cl_x/NiFe$ heterostructure. More specifically, the magnetic damping parameters were obtained from the θ_H dependence of both the peak-to-peak FMR linewidth and the resonance field for different thicknesses of NiFe film, by taking into consideration the extrinsic contribution of the two-magnon scattering and the inhomogeneity. The growth of NiFe film on $CH_3NH_3PbI_{3-x}Cl_x$ has been studied also by AFM and MOKE techniques. The combined analysis reveals that the growth of the NiFe film begins via island formation, where small isolated islands grow larger to coalesce with other islands and eventually form a continuous film. This evolution of NiFe morphology seems to affect the ability of spin angular momentum transfer to the $CH_3NH_3PbI_{3-x}Cl_x$ layer reflected as an intense enhancement of $g^{\uparrow\downarrow}$ until the formation of a continuous thin film, illustrating the importance of interface properties on the spin dependent phenomena. Our result could also have wider implications for other material systems, especially organic semiconductors where a similar growth of ferromagnets takes place onto solution processed films.

By taking advantage of the spin properties of OIHPs that we have already discussed in sections 6.7.4 and 9.1 as a following project we plan to inject and detect spin polarized electrons on $CH_3NH_3PbI_{3-x}Cl_x$ by using the optical spin orientation technique [276]. More specifically, a $CH_3NH_3PbI_{3-x}Cl_x$ Hall-bar device is going to be illuminated by circular polarized light at specific wavelength and simultaneously a voltage difference ($V_{||}$) is applied in one direction of the Hall-bar device (Figure 10.2.a). The generated spin polarized electrons drift through perovskite Hall-bar and experience spin dependent transverse deflection generated via the ISHE. As a consequence, charge accumulation occurs, which can be measured as voltage difference ($V_{\perp}$) (Figure 10.2.a).

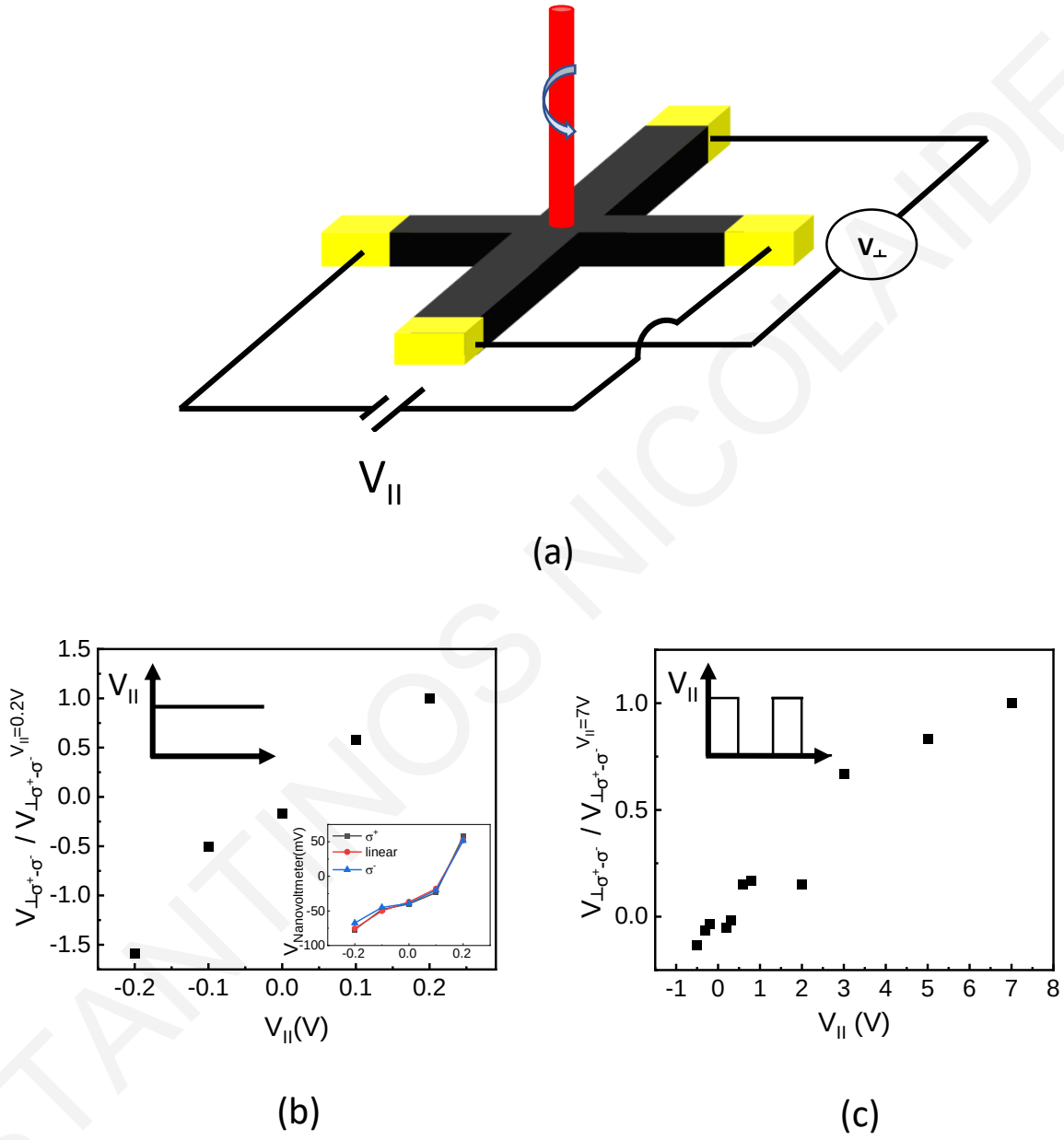

Figure 10.2: (a)Schematic representation of optical spin orientation method in a $CH_3NH_3PbI_{3-x}Cl_x$ Hall-bar. (b)Normalized transverse voltage difference ($V_{\perp\sigma^+-\sigma^-}$) of right and left circularly polarized light as a function of longitudinal continuous, (c) alternating voltage.

This project is already in progress in a very early stage, so we will present some preliminary results along with some difficulties we have already faced.

The first obstacle that we had to overcome was the need for sample morphology improvement. By following the typical fabrication method, OIHP films always suffer from non-uniform coverage with grains and voids [277], which are provoked by the formation of the rough solvent containing the intermediate phase of the $DMF - PbI_2 - MAI$ bulk structure during the slow evaporation of the solvent [278]. The improvement of the film uniformity has been realized by the addition of a post treatment step by the spontaneous insertion of $CH_3NH_2(MA)$ gas [279]. This extra step provokes the acceleration of the solvent removal and therefore the rate of nucleation and spatial distribution is increased and has resulted in a continuous disordered crystal of the order of a centimeter which can be manageable for our goal. By following this method, a compact $CH_3NH_3PbI_{3-x}Cl_x$ film with an approximate thickness of 0.5 μm was obtained. Then we selectively scratched the film to pattern the desired Hall-bar and four Cu contacts were deposited by thermal evaporation. We also observed a first indication of successful injection and detection of spin information in the $CH_3NH_3PbI_{3-x}Cl_x$ Hall-bar by using two measurement methods. The first involves a continuous voltage difference ($V_{||}$) applied at one direction of the Hall-bar device while simultaneously a right/left circularly polarized light ($\sigma^+/\sigma^-, hv = 1.7eV$) was incident at the center of the Hall-bar. At the same time the transverse voltage, $V_\perp$, was measured by a nanovoltmeter as a function of longitudinal voltage. Figure 10.2.b shows the normalized transverse voltage difference ($V_{\perp\sigma^+-\sigma^-}$) between right and left circularly polarized light. The change in the sign of $V_{\perp\sigma^+-\sigma^-}$ upon reversing the longitudinal current indicates the successful detection of the ISHE transverse voltage. Furthermore, for the second measurement method we followed the same procedure, but this time an alternating square wave voltage, with frequency 2 KHz, was applied and the detection of the transverse voltage carried out by a lock-in amplifier. The $V_{\perp\sigma^+-\sigma^-}$ had again the same behavior as before (Figure 10.2.c) which confirm the indication of spin current injection and detection. However, the existence of a series of other effects like thermal gradients and the dember effect [280, 281], result in a noisy signal which very often masks the ISHE. In order to confirm the effect we plan to repeat the procedure for different temperatures and at the presence of an external

magnetic field. We will also try to improve further the experimental setup and develop perovskite Hall-bars with better quality and smaller dimensions, in order to achieve smaller resistance and greater stability over time at ambient conditions.

Appendix A

Supplementary data for Chapter 7

A.1 Hall effect results

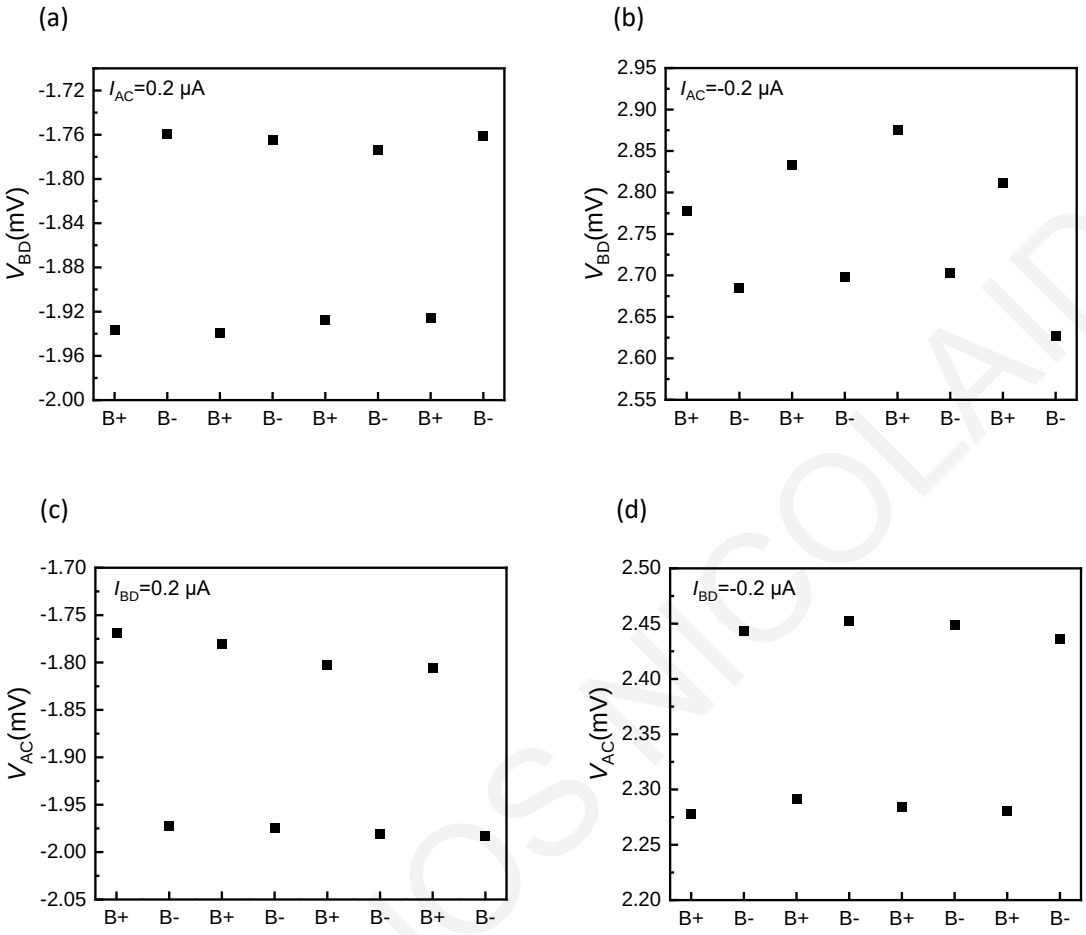

Figure A.1: Hall voltage measurements for opposite directions of the applied magnetic field for sample P5. (a) V_{BD} for I_{AC}=0.2 μA , (b) V_{BD} for I_{AC}=-0.2 μA, (c) V_{AC} for I_{BD}=0.2 μA and (d) V_{AC} for I_{BD}=-0.2 μA

A.2 ESR results

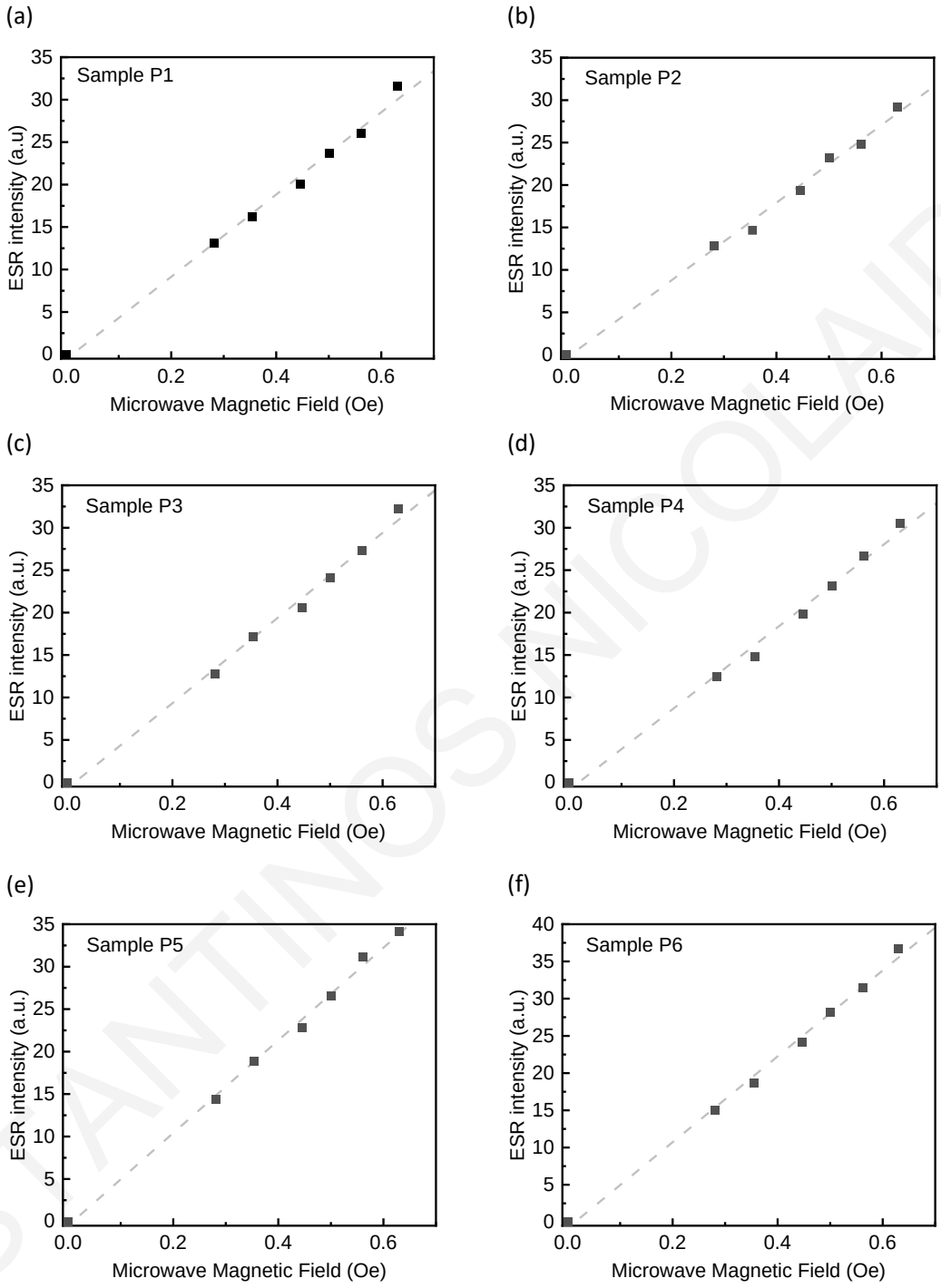

Figure A.2: ESR intensities as a function of the microwave magnetic field at room temperature for (a) P1, (b) P2, (c) P3, (d) P4, (e) P5 and (f) P6. The dashed line is a linear fit to the data.

A.3 PEDOT:PSS film thickness measurement

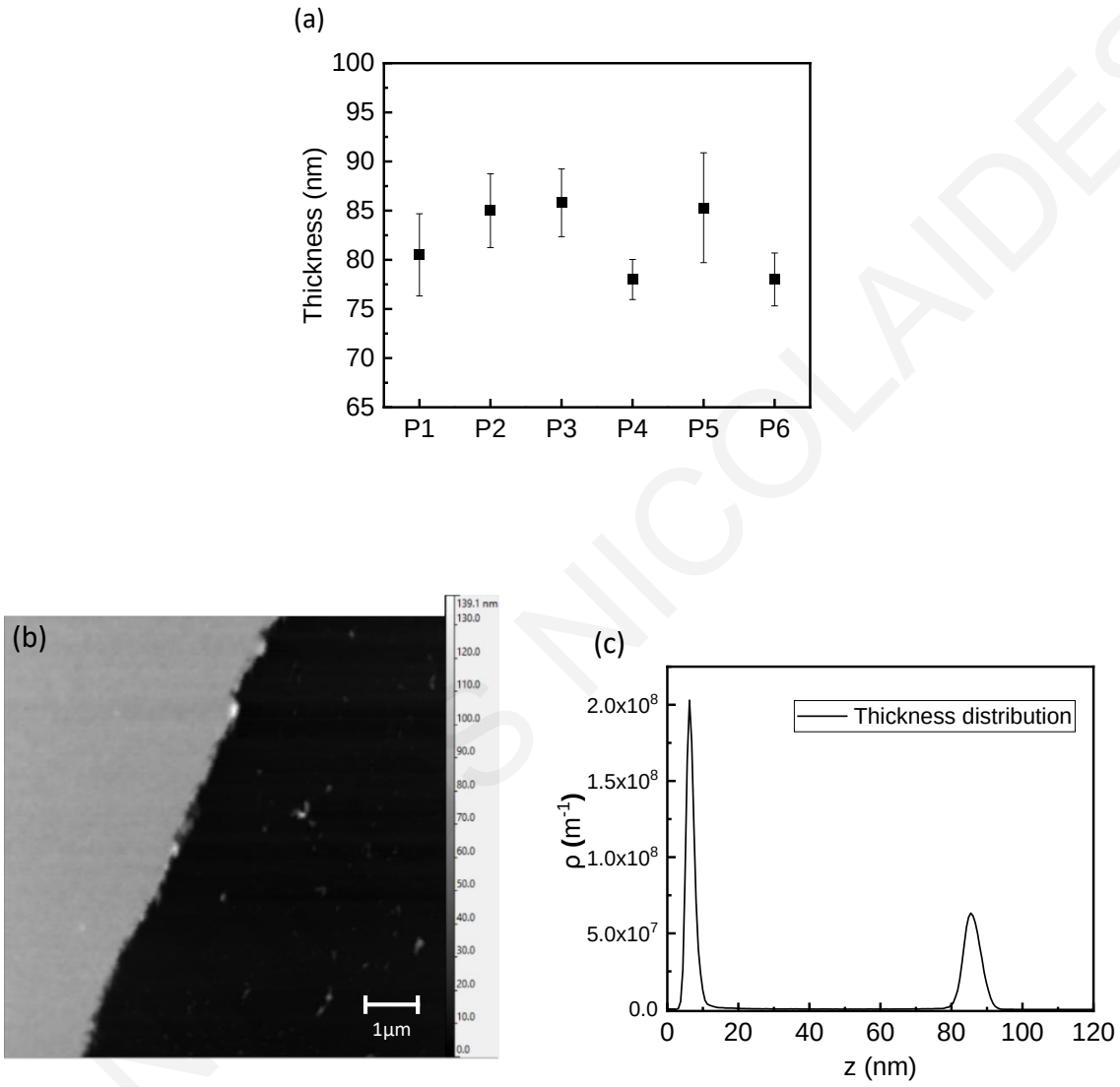

Figure A.3: (a)AFM thickness measurements for all samples. (b) A typical surface morphology of a step created by scratching with a stainless-steel needle for sample P4 in order to determine sample's thickness. (c) Thickness distribution of sample P4.

A.4 Microwave power dependence of voltage signal

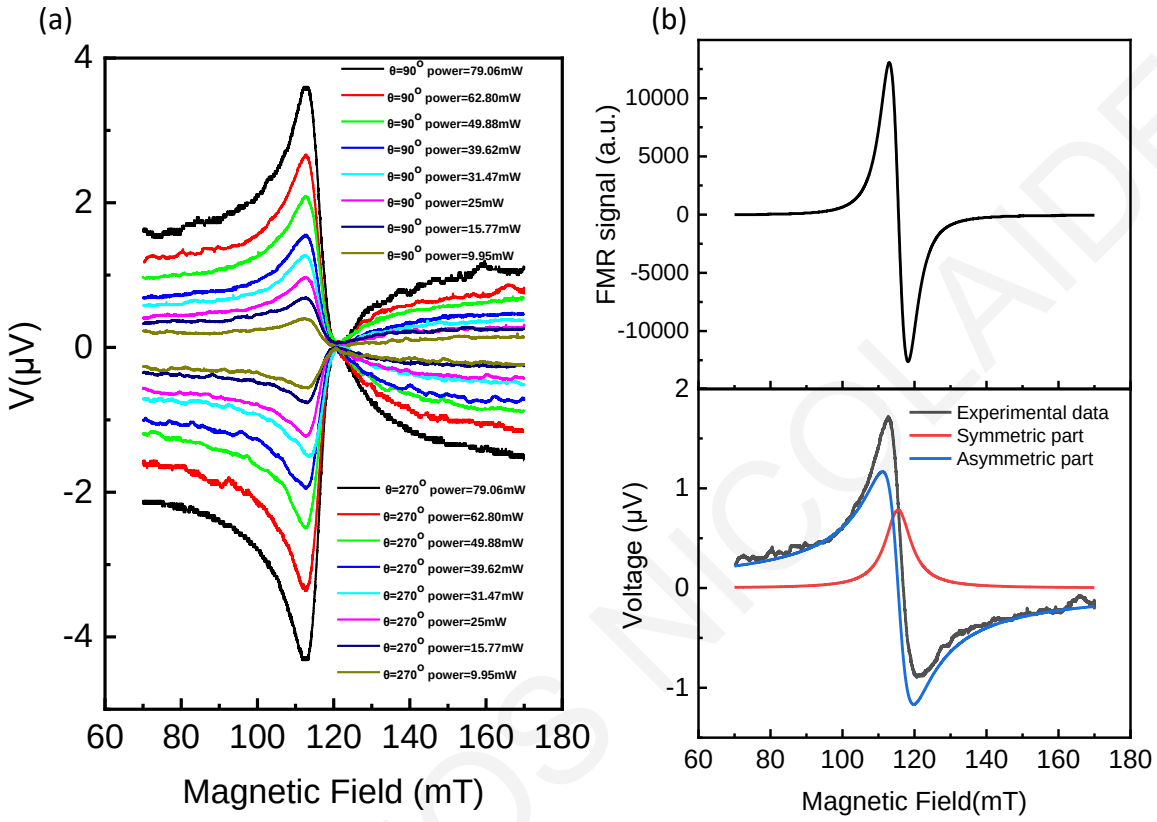

Figure A.4: (a) Voltage signal detected at different microwave power, from the sample NiFe/P2 for the two in-plane external magnetic field directions $\theta_H = 90^o$ and $\theta_H = 270^o$, (b) FMR spectrum and measured voltage V for the NiFe/P2 sample.

A.5 Measurement of Seebeck coefficient

The Seebeck coefficient was determined with the experimental setup shown in Figure A.5.a consisting of a heater to induce a temperature gradient in the PEDOT:PSS sample. In order to measure the thermal voltage, two Cu electrodes with a spacing $L = 300\mu m, 400\mu m$ were thermally evaporated on the film and were connected to a Keithley 2181A nanovoltmeter through spring-loaded Be-Cu probes. Two K-type micro-thermocouples (μTCs) were connected on the sample with a spacing K which was much larger than both the μTC diameter and the electrodes spacing. The temperature difference (ΔT) across the electrode spacing was given as $\Delta T = \Delta T_{TC} L/K$. ($\Delta T_{TC}$ is the temperature difference between the μTCs) [146]. Finally, the thermal voltage was measured as a function of the temperature difference and the Seebeck coefficient, S, obtained from the slope of the linear relationship between thermal voltage and temperature difference. The results for all samples are plotted in Figure A.5.b. We note that the Seebeck coefficient shows an opposite trend to the spin Hall voltage with increasing dedoping ($P1 \rightarrow P6$). Seebeck coefficient increases with dedoping, while the spin Hall voltage decreases approximately by one order of magnitude.

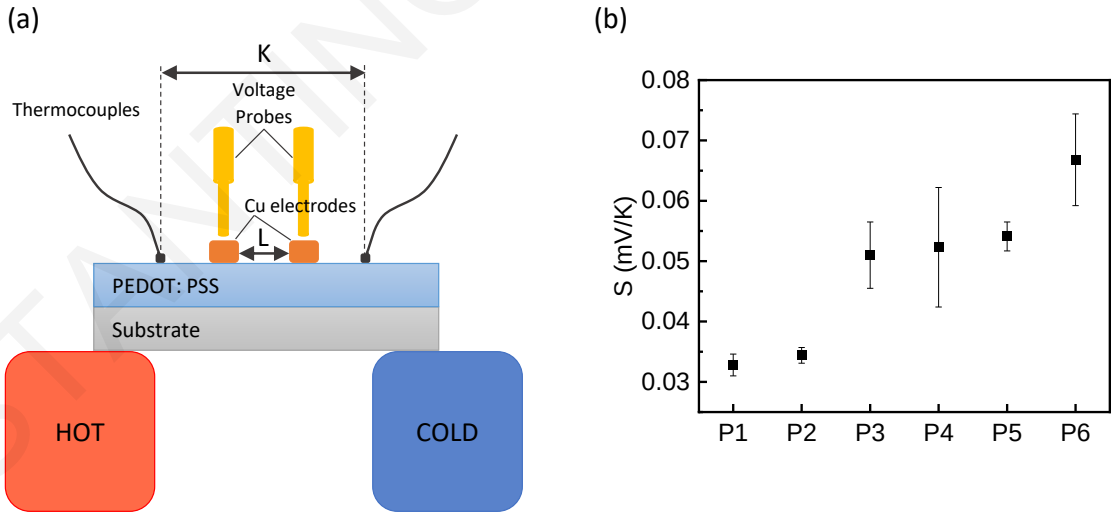

Figure A.5: (a)Schematic of the experimental setup used for determining the Seebeck coefficient. (b) Seebeck coefficient measurement for all doping levels from P1 to P6.

A.6 Estimation of spin Hall angle, θ_{SHE}

The estimation of the spin Hall angle, θ_{SHE}, was carried out throughthe ISHE voltage and the calculation of the parameters that characterize the NiFe/PEDOT:PSS interface and we relied on the spin pumping theory used by Saitoh et al (section 4.4) as applied to inorganic [92] and organic [135] materials. More precisely, at FMR of the NiFe layer in our NiFe/PEDOT:PSS structure, a pure spin current is injected into the PEDOT:PSS layer via spin pumping. The spin current density at the interface and with in-plane external magnetic field is given by $j_s^o = \frac{g^{\uparrow\downarrow}\gamma^2 h^2 \hbar \left[4\pi M_s\gamma + \sqrt{(4\pi M_s)^2\gamma^2 + 4\omega^2}\right]}{8\pi\alpha^2[(4\pi M_s)^2\gamma^2 + 4\omega^2]}$. The spin mixing parameter, $g^{\uparrow\downarrow}$, in turn can be calculation as $g^{\uparrow\downarrow} = \frac{2\sqrt{3}\pi M_s \gamma t_{FM}}{g\mu_B\omega}(W_{FM/NM} - W_{FM})$, where $W_{FM/NM}$ and W_{FM} are the FMR spectral width of the NiFe/PEDOT:PSS bilayer and NiFe layer, respectively. The θ_{SHE} can then be expressed as $\theta_{SHE} = \frac{V_{ISHE}(d_F\sigma_F + d_N\sigma_N)}{j_s^o w \lambda_N tanh(d_N/2\lambda_N)}\left(\frac{\hbar}{2e}\right)$, where w is the width of the NiFe layer between the contacts, d_N , σ_N and d_F , σ_F are the thickness and the conductivity of the PEDOT:PSS layer and the NiFe layer, respectively. Some of the most significant parameters obtained are presented in Table A.1.

Table A.1: Estimation of θ_{SHE} through experimental parameters derived from FMR/ISHE measurements.

Sample	$W_{FM/OSC} - W_{FM}(mT)$	$4\pi M_s(mT)$	$g^{\uparrow\downarrow}(m^{-2})$	$j_s^o(Jm^{-2})$	$V_{ISHE}(\mu V)$	θ_{SHE}
P1	1.163	760.4	8.54E+18	9.75E-08	1.415	1.28E-06
P2	1.002	762.2	7.38E+18	8.95E-08	0.580	5.38E-07
P3	1.142	727.1	8.02E+18	9.29E-08	0.332	2.94E-07
P4	1.107	699.8	7.49E+18	8.82E-08	0.195	1.99E-07
P5	0.902	759.3	6.62E+18	8.35E-08	0.259	2.55E-07
P6	1.141	708.6	7.81E+18	9.07E-08	0.171	1.68E-07

A.7 Raman Spectroscopy

Resonance Raman (RR) experiments were conducted with excitation at 532 nm using a custom-made Raman microscope (Raman AlphaSource RLS4032, NanoBioAnalytics). A 20x objective was used to focus 35 mW of the laser light onto the film surface. The Raman scattered light was collected through an optical fiber and delivered to a 0.30 m focal-length Czerny-Turner spectrograph (SpectraPro, SP2300i, Princeton Instruments), equipped with a 1200 $grooves/mm$ classically-ruled grating. The slit width was set to 30 μm providing 2 cm^{-1} spectral resolution at 532 nm. The scattered light was detected by a LN2-cooled 1340 $\times$ 100 pixel, back-illuminated CCD detector (Spec10:100B/LN, Princeton Instruments). Each spectrum is the accumulation of 5 $\times$ 10 min spectra. Frequency calibration of the spectra was accomplished with the use of cyclohexane. The area, linewidth (FWHM) and the position of all Raman bands (see Table A.2, A.3), including quinoid and benzoid bands were determined by deconvolution of Resonance Raman spectra (see Figure A.6.a and Table A.3, as an example corresponding to P1 and Figure A.6.b for P6), which were modeled using Voigt peaks (distribution of Lorentzian and Gaussian profiles).

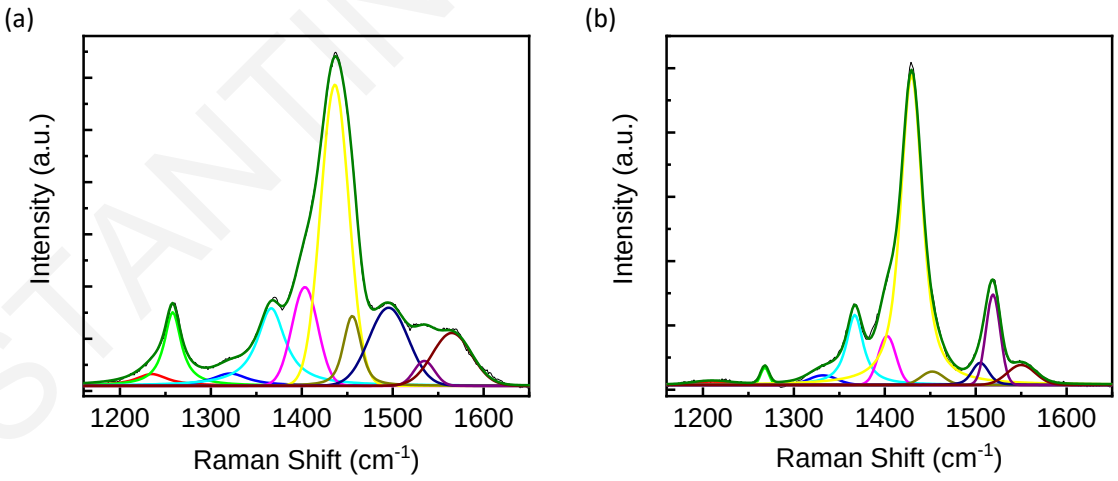

Figure A.6: Deconvolution of RR spectra for (a) P1 and (b) P6 with excitation at 532 nm.

Table A.2: Comparison of the frequencies (cm^{-1}) of Raman bands of P1-P6 extracted from deconvolution of resonance Raman spectra.

Frequency(cm^{-1})						Assignment
P1	P2	P3	P4	P5	P6	
1235	1235	1238	1240	1236	1209	$C_a - C_a$ inter-ring stretching
1258	1258	1255	1255	1255	1268	$C_a - C_a$ inter-ring stretching
1321	1321	1324	1320	1324	1332	$C_b - C_b$ stretching
1366	1366	1363	1363	1364	1367	$C_b - C_b$ stretching
1403	1403	1400	1400	1399	1402	Asymmetric $C_a = C_b(-O)$ stretching
1436	1436	1432	1431	1432	1429	Quinoid symmetric $C_a - C_b(-O)$ stretching
1456	1456	1453	1452	1453	1452	Benzoid symmetric $C_a = C_b(-O)$ stretching
1495	1495	1492	1494	1497	1505	Asymmetric $C = C$ stretching
1535	1533	1529	1529	1533	1519	Asymmetric $C = C$ stretching
1565	1565	1562	1560	1562	1550	Asymmetric $C = C$ stretching

Table A.3: Comparison of the frequencies (cm^{-1}) of Raman bands of P1-P6 extracted from deconvolution of resonance Raman spectra.

Frequency (cm^{-1})	Width Gaussian (cm^{-1})	Width Lorentzian (cm^{-1})	Area
1235	4	42	7499
1258	-	22	24837
1321	-	47	8793
1366	-	37	43532
1403	34	-	33852
1436	36	-	111758
1456	16	11	19802
1495	51	-	40586
1535	27	-	6740
1565	50	-	27164

Appendix B

Supplementary data for Chapter 8

B.1 ESR spectroscopy

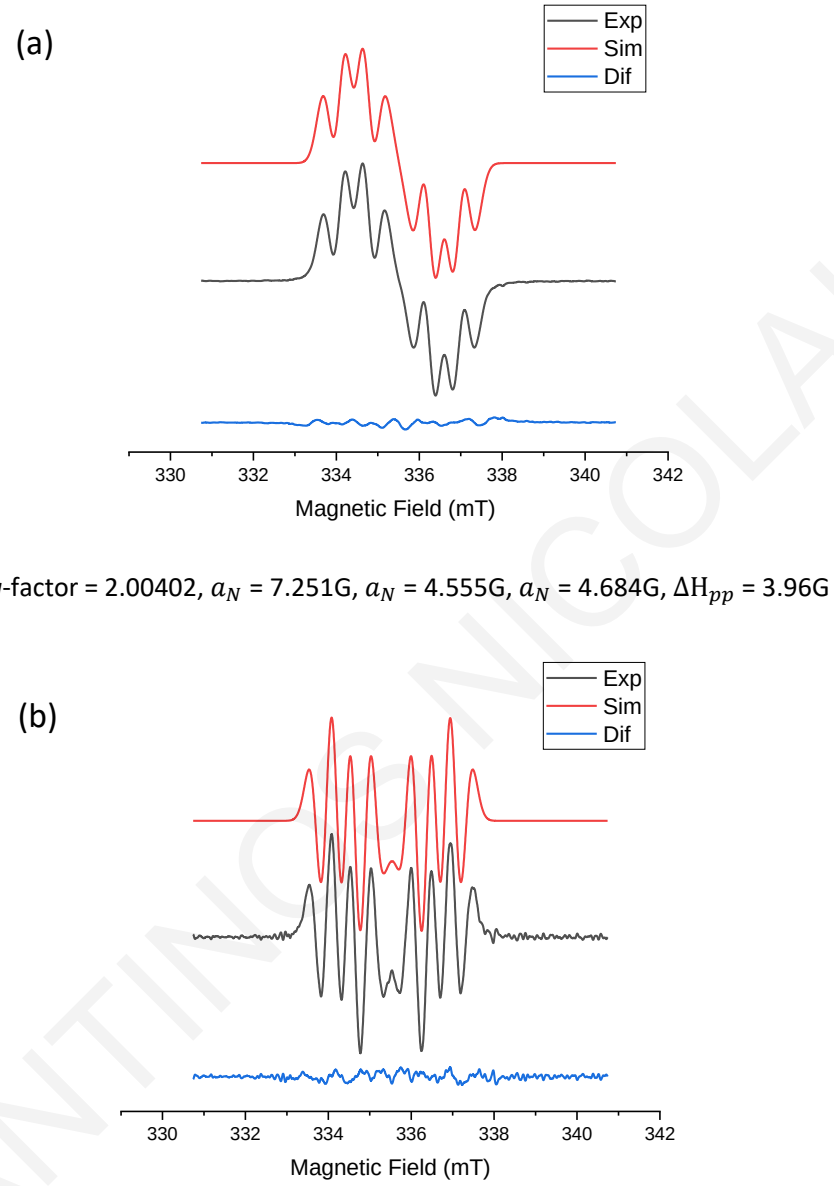

Figure B.1: Experimental (CH_2Cl_2, ca. 20 °C) and simulated first (a) and second (b) order ESR spectra of ESR along with their simulation parameters. Simulations of the solution spectra were performed using EasySpin.

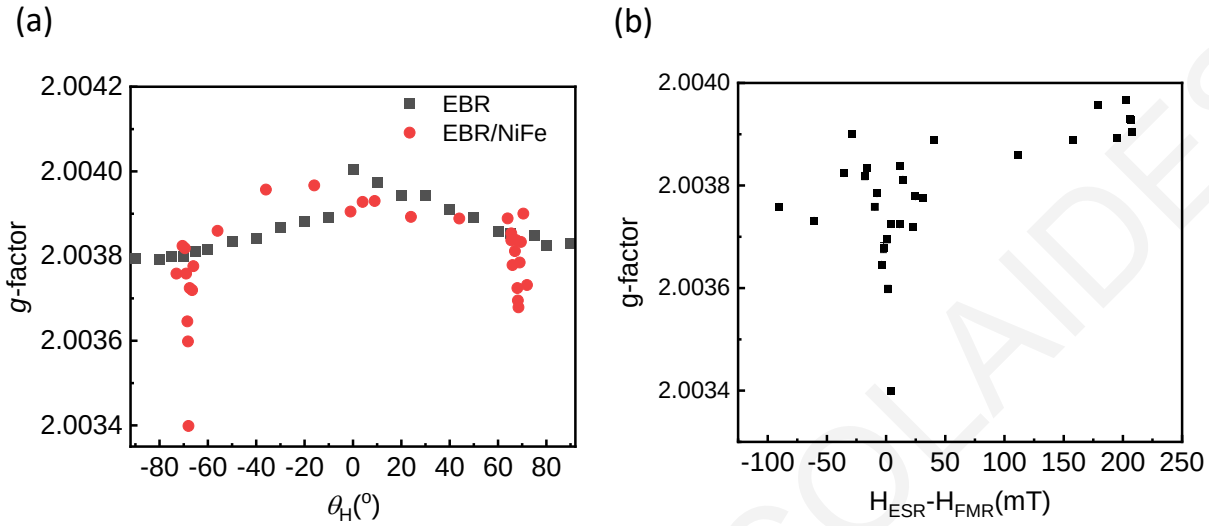

Figure B.2: The g-factor of the EBR layer and the EBR/NiFe bilayer as a function of θ_H angle (b) as a function of the field separation of the two resonances, $H_{ESR} - H_{FMR}$.

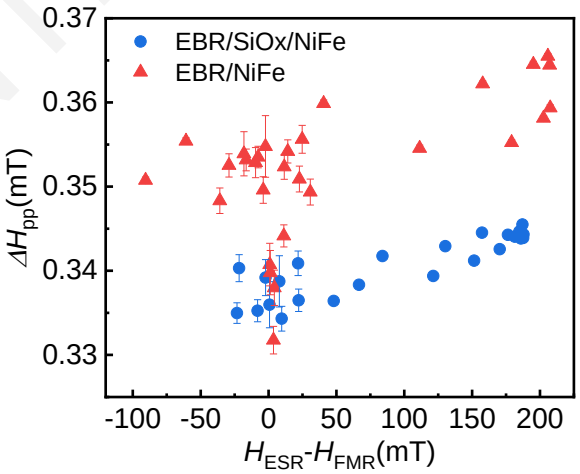

Figure B.3: The linewidth, ΔH_{pp}, of the EBR/NiFe bilayer and the EBR/SiOx/NiFe trilayer as a function of the field separation of the two resonances, $H_{ESR} - H_{FMR}$.

B.2 AFM measurement

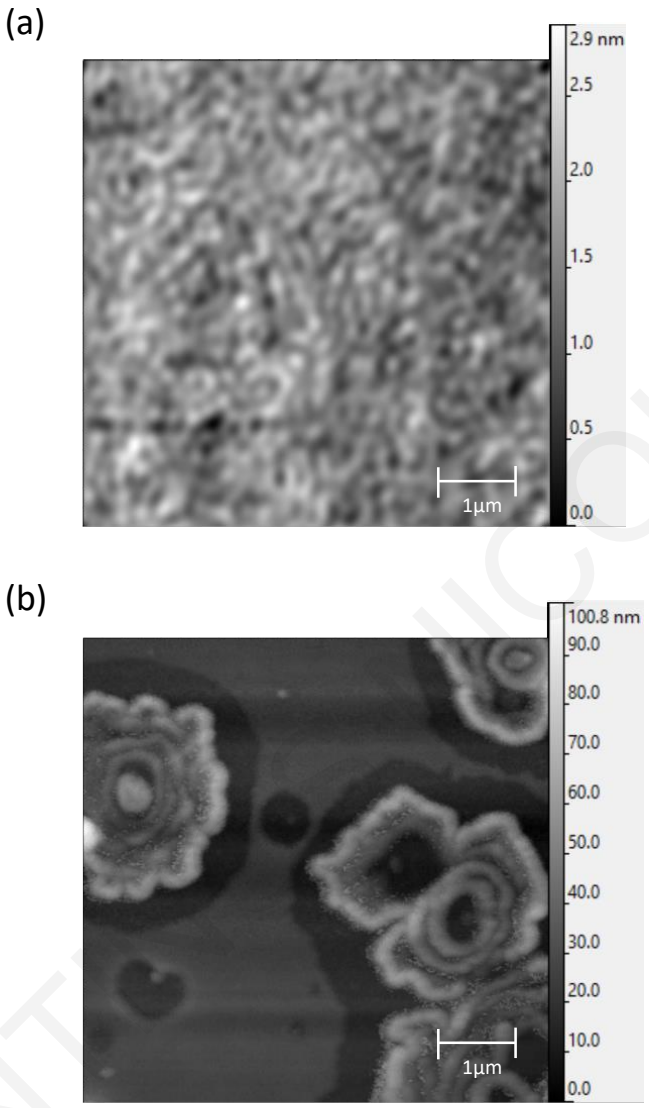

Figure B.4: Typical 6 μm x 6 μm AFM images for the (a) EBR and (b) MBR thin film from which a root mean square (rms) roughness 250 $\pm$ 30 pm and 11 $\pm$ 3 nm was calculated, respectively.

B.3 Conductivity measurement

The conductivity of EBR thin films was measured using two-probe method. Two Au electrodes with a spacing of 40 μm were thermally evaporated on the film and were connected to Keithley 2450 sourcemeter. The IV curve was measured and combined with the thickness obtained by AFM the conductivity was estimated $\sigma \approx 5 \times 10^{-4} Scm^{-1}$.

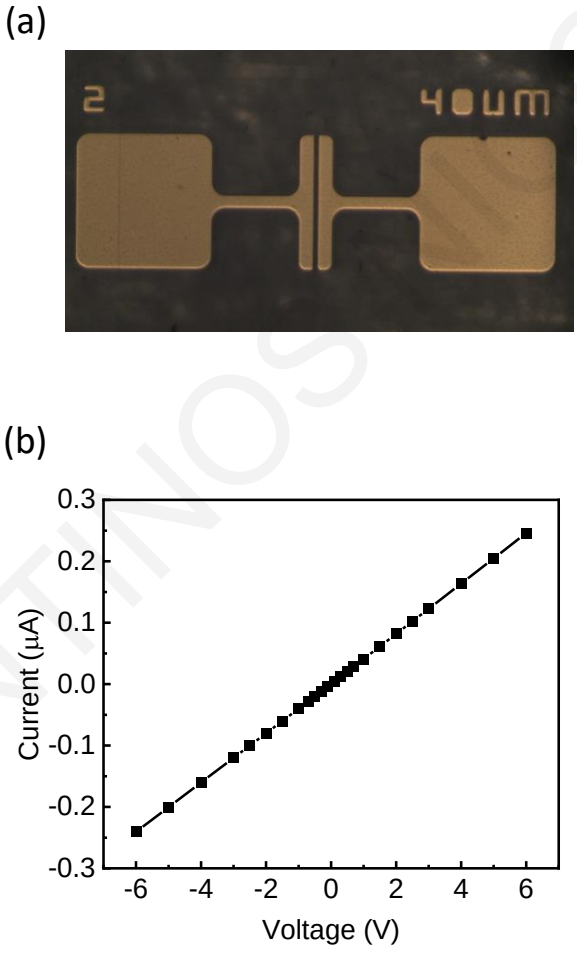

Figure B.5: (a) Device used for the measurement of EBR film's conductivity. (b) Typical I-V curve of an EBR film.

B.4 ESR fitting procedure

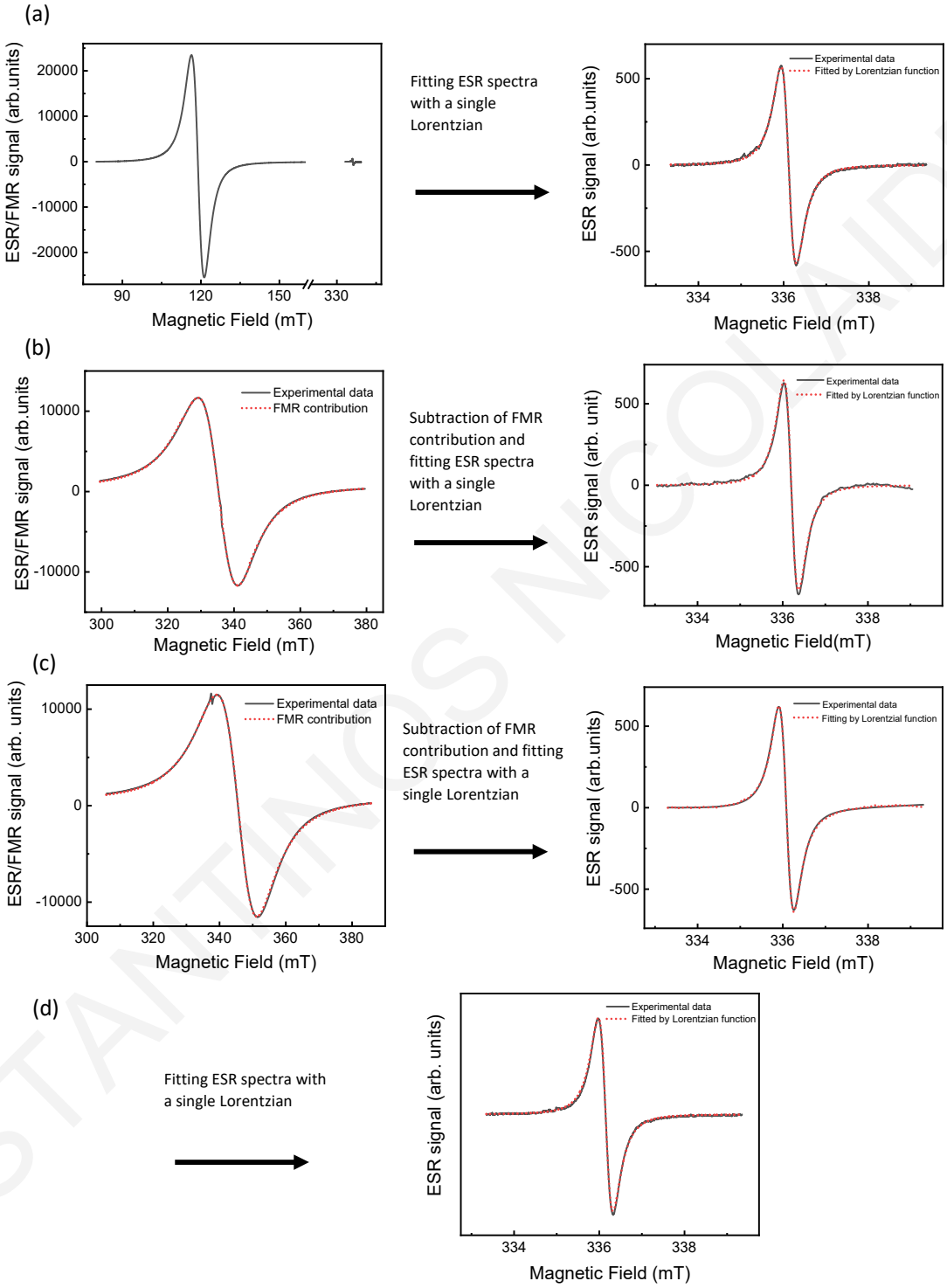

Figure B.6: Detailed presentation of the fitting procedure of ESR spectra for the EBR/NiFe bilayer at (a) $\theta_H = 0^o$, (b) $\theta_H = 68.25^o$, (c) $\theta_H = 69^o$ and the EBR single layer (d) at $\theta_H = 0^o$.

Appendix C

Supplementary data for Chapter 9

C.1 Estimation of magnetic damping parameters.

The θ_H dependence of both the FMR linewidth (ΔH_{pp}) and the FMR resonance field (H_{FMR}) have been used to obtain the magnetic damping parameters of the $CH_3NH_3PbI_{3-x}Cl_x/NiFe$ bilayers ($\alpha_{Per/NiFe}$) and the pristine NiFe layers (α_{NiFe}). In addition to the intrinsic damping contribution to the linewidth (Eq. 9.5), ΔH_{intr}, we took into consideration extrinsic contributions arising from inhomogeneity (Eq. 9.6), ΔH_{inhom}, and due to two-magnon scattering, ΔH_{2mag}. The last term, ΔH_{2mag}, corresponds to surface defect induced two-magnon scattering mechanism and can be written as [268, 282]

$$\Delta H_{2mag} = \frac{2}{\sqrt{3}}\Gamma(H_{FMR},\theta_H)\sin^{-1}\sqrt{\frac{H_x}{H_x+4\pi M_{eff}}\frac{\cos(2\theta_M)}{\cos^2\theta_M}}. \tag{C.1}$$

The term $\Gamma(H_{FMR},\theta_H)$ reflects the magnitude of two-magnon scattering and is related to the surface magnetic field (H_S) and the characteristics of defects in the samples and is given by

$$\begin{aligned}\Gamma(H_{FMR},\theta_H) = \frac{8H_S^2b^2p}{\pi D(H_x+H_y)^2\Xi}\Bigg\{\left(\left\langle\frac{c}{\alpha}\right\rangle-1\right)H_y^2+\left(\left\langle\frac{\alpha}{c}\right\rangle-1\right)\times \\ \Big[H_x\cos(2\theta_M)+H_y\cos^2\theta_M\Big]^2+\Big[H_x\cos(2\theta_M)-H_y\sin^2\theta_M\Big]^2\Bigg\}\end{aligned} \tag{C.2}$$

where Ξ, H_x, H_y are defined as

$$\Xi \equiv \cos(\theta_H-\theta_M)-\frac{3H_x+H_y}{H_y(H_x+H_y)}H_{FMR}\sin^2(\theta_H-\theta_M) \tag{C.3}$$

$$H_x \equiv H_{FMR}\cos(\theta_H-\theta_M)-4\pi M_s\cos^2\theta_M \tag{C.4}$$

$$H_y \equiv H_{FMR}\cos(\theta_H-\theta_M)-4\pi M_s\cos 2\theta_M \tag{C.5}$$

$D = 20000mTnm^2$ [78] and p corresponds to the exchange stiffness of the ferromagnet and the percentage coverage of the ferromagnetic surface by defects which we assume to have a rectangular shape with lateral dimensions α and c and height b. By assuming that there is no anisotropy between both lateral directions $\left\langle\frac{c}{\alpha}\right\rangle = \left\langle\frac{\alpha}{c}\right\rangle$ and by setting typical geometrical parameters $b = 1nm$, $<\alpha>= 1nm$ and $p = 0.5$ [75, 268] and by using the relations [78]

$$r = \frac{16s}{\pi D}\ln\left[\left(\frac{q_m}{q_o}\right)^{\frac{1}{2}}+\left(1+\frac{q_m}{q_o}\right)^{\frac{1}{2}}\right] \tag{C.6}$$

where $r = 0.00008mT^{-1}$ ([78]) corresponds to renormalization factor with $s = pb^2\left(\left\langle\frac{\alpha}{c}\right\rangle-1\right)$ being a geometrical factor characteristic of the surface roughness,

$q_o = \frac{2\pi M_s t}{D}$ a characteristic volume-mode wavenumber and $q_m = \frac{1}{<\alpha>}$ a cut-off wavenumber determined by the transverse length scale of the surface defects, we calculate the $\left\langle \frac{\alpha}{c} \right\rangle$ geometrical parameter.

Using the ferromagnetic resonance field, H_{FMR}, measured as a function of applied field angle, θ_H, the corresponding θ_M can be obtained by using the static equation [92]

$$2H_{FMR}\sin(\theta_H - \theta_M) + 4\pi M_{eff}\sin 2\theta_M = 0. \tag{C.7}$$

Employing the ferromagnetic resonance condition, Eq. 9.3, the effective saturation magnetization, $4\pi M_{eff}$, can be estimated for each t_{NiFe}. Moreover, the surface magnetic anisotropic field, H_s, can be calculated via

$$4\pi M_{eff} = 4\pi M_s - H_s = 4\pi M_s - \frac{2K_s}{M_s t_{NiFe}} \tag{C.8}$$

and combined with the use of typical geometrical parameters [75, 268] for the defects the two-magnon scattering linewidth contribution, ΔH_{2mag}, can be estimated. We can then proceed with the fitting of the data using all three contributions to the linewidth the Eqs. 9.4-9.6, C.1 with α, Δ_{θ_H} and $\Delta_{4\pi M_{eff}}$ as fitting parameters. In this way the magnetic damping parameters, $\alpha_{Per/NiFe}$ and α_{NiFe} were calculated for every NiFe deposition thickness.

Appendix D

List of Publications and Presentations

(A) Publications directly related to the thesis.

(1) 'Effect of structural conformation of conjugated polymers on spin transport.'
C. Nicolaides, E. Nicolaidou, P. Papagiorgis, G. Itskos, S. C. Hayes, T. Trypiniotis
Phys. Rev. Materials 6, 095601, 2022

(2) 'Metal-Free Organic Radical Spin Source'
C. Nicolaides, F. Bazzi, E. Vouros, D. F. Flesariou, N. Chrysochos, P. Koutentis, C. Constantinides, T. Trypiniotis
Nano Lett. 23, 10, 4579-4586, 2023

(3) 'Spin pumping across hybrid organic-inorganic perovskite/ferromagnet interface: the effect of ferromagnet morphology.'
C. Nicolaides, T. Trypiniotis
Submitted in AIP Advances in October 2023

(B) Other Publications

(1) 'Preparation of Blatter Radicals via Aza-Wittig Chemistry: The Reaction of N Aryliminophosphoranes with 1-(Het)aroyl-2-aryldiazenes.'
A. C. Savva, S. Mirallai, G. Zissimou, A. A. Berezin, M. Demetriades, A. Kourtellaris, C. Constantinides, **C. Nicolaides**, T. Trypiniotis, P. A. Koutentis
J. Org. Chem. 82, 14, 7564-7575, 2017

(2) 'Efficient Optical Amplification in the Nanosecond Regime from Formamidinium Lead Iodide Nanocrystals.'
P. Papagiorgis, A. Manoli, L. Protesescu, C. Achilleos, M. Violaris, **C. Nicolaides**, T. Trypiniotis, M. I. Bodnarchuk, M. V. Kovalenko, A. Othonos, G. Itskos
ACS Photonics 5, 3, 907-917 2018

(3) '3,3',3"-(Benzene-1,3,5-triyl)tris(1-phenyl-1H-benzo[e][1,2,4]triazin-4-yl): A C3 symmetrical Blatter-type triradical.'
G. Zissimou, A. A. Berezin, M. Manoli, **C. Nicolaides**, T. Trypiniotis, P. A. Koutentis
Tetrahedron 76, 15, 131077, 2020

(4) 'Methyl-Driven Overhauser Dynamic Nuclear Polarization.'
F. A. Perras, D. F. Flesariu, S. A. Southern, **C. Nicolaides**, J. D. Bazak, N. M. Washton, T. Trypiniotis, C. P. Constantinides, P. A. Koutentis
J. Phys, Chem. Lett. 13, 18, 4000-4006, 2022

(5) 'The Impact of Ligand Removal on the Optoelectronic Properties of Inorganic and Hybrid Lead Halide Perovskite Nanocrystal Films.'
P. Papagiorgis, M. Sergides, A. Manoli, M. Athanasiou, C. Bernasconi, F. Galatopoulos, **C. Nicolaides**, E. Leontidis, T. Trypiniotis, S. Choulis, M. I. Bodnarchuk, M. V. Kovalenko, A. Othonos, G. Itskos
Accepted in Advanced Optical Materials 2023

(6) 'Temperature-Dependent Antiferromagnetic Exchange Along 1D Linear Regular Chains of Phthalonitrile Blatter Radical.'
N. Chrysochos, C. Constantinides, G. Leitus, A. Kourtellaris, D. Lawson, M. Deumal, J. Ribas-Arino, M. A. Carvajal, G. Zissimou, **C. Nicolaides**, T. Trypiniotis, P. A. Koutentis
Accepted in Crystal Growth & Design 2023

(C) Presentations

(1) 'Demonstration of spin transport and inverse spin Hall effect in GeOI at room temperature.' (Oral talk)
C. Nicolaides, A. Papachristodoulou, T. Trypiniotis
CTMNM/NAGC Workshop (2017)

(2) 'Spin Pumping in Hybrid Organic-Inorganic Perovskite.' (Oral talk)
C. Nicolaides, T. Trypiniotis
7th International Meeting on Spin in Organic Semiconductors (SpinOS), Halle, Germany (2018)

(3) 'Spin Pumping in Hybrid Organic-Inorganic Perovskite.' (Oral talk)
C. Nicolaides, T. Trypiniotis
XXXIII Panhellenic Conference on Solid State Physics and Material Science, Nicosia (2018)

(4) 'Influence of Carriers in Spin Pumping in Organic Semiconductors.' (Oral talk-Hybrid)
C. Nicolaides, T. Trypiniotis
IEEE-Magnetism and Magnetic Materials (MMM) Conference (2020)

Bibliography

[1] J. A. Weil and J. R. Bolton, *Electron Paramagnetic Resonance: Elementary Theory and Practical Applications*. John Wiley, Hoboken, NJ, 2007.

[2] Z. G. Yu, "Suppression of the Hanle Effect in Organic Spintronic Devices," *Physical Review Letters*, vol. 111, p. 16601, 2013.

[3] Z. G. Yu, "Spin-Orbit Coupling, Spin Relaxation, and Spin Diffusion in Organic Solids," *Phys. Rev. Lett.*, vol. 106, p. 106602, 2011.

[4] S. A. Wolf, D. D. Awschalom, R. A. Buhrman, J. M. Daughton, S. von Molnar, M. L. Roukes, A. Y. Chtchelkanova, and D. M. Treger, "Spintronics: A Spin-Based Electronics Vision for the Future," *Science*, vol. 294, pp. 1488–1495, 2001.

[5] J. Puebla, J. Kim, K. Kondou, and Y. Otani, "Spintronic devices for energy-efficient data storage and energy harvesting.," *Communications Materials*, vol. 1, pp. 1–9, 2020.

[6] M. N. Baibich, J. M. Broto, A. Fert, F. N. V. Dau, F. Petroff, P. Etienne, G. Creuzet, A. Friederich, and J. Chazelas, "Giant Magnetoresistance of (001)Fe/(001)Cr Magnetic Superlattices.," *Phys. Rev. Lett.*, vol. 61, pp. 2472–2475, 1988.

[7] G. Binasch, P. Grünberg, F. Saurenbach, and W. Zinn, "Enhanced magnetoresistance in layered magnetic structures with antiferromagnetic interlayer exchange.," *Phys. Rev. B*, vol. 39, pp. 4828–4830, 1989.

[8] A. D. Kent, D. C. Worledge, H.-S. P. Wong, S. Salahuddin, S. Parkin, and S.-H. Yang, "Spin-transfer-torque memory," *Nature Nanotechnology*, vol. 10, pp. 185–198, 2015.

[9] G. E. W. Bauer, E. Saitoh, and B. J. van Wees, "Spin caloritronics," *Nature Materials*, vol. 11, pp. 391–399, 2012.

[10] R. Jansen, "Silicon spintronics," *Nature Materials*, vol. 11, pp. 400–408, 2012.

[11] T. Jungwirth, X. Marti, P. Wadley, and J. Wunderlich, "Antiferromagnetic spintronics," *Nature Nanotechnology*, vol. 11, p. 231–241, 2016.

[12] D. Sun, E. Ehrenfreund, and Z. V. Vardeny, "The first decade of organic spintronics research," *Chemical communications*, vol. 50, pp. 1781–1793, 2014.

[13] D. Li and G. Yu, "Innovation of Materials, Devices, and Functionalized Interfaces in Organic Spintronics," *Adv. Funct. Mater.*, vol. 31, p. 2100550, 2021.

[14] J. H. Burroughes, D. D. C. Bradley, A. R. Brown, R. N. Marks, K. Mackay, R. H. Friend, P. L. Burns, and A. B. Holmes, "Light-Emitting Diodes Based on Conjugated Polymers," *Nature*, vol. 347, 1990.

[15] J. Zhao, Y. Li, G. Yang, K. Jiang, H. Lin, H. Ade, W. Ma, and H. Yan, "Efficient Organic Solar Cells Processed from Hydrocarbon Solvents," *Nat. Energy*, vol. 1, 2016.

[16] J. Lenz, F. del Giudice, F. R. Geisenhof, F. Winterer, and R. T. Weitz, "Vertical, Electrolyte-Gated Organic Transistors Show Continuous Operation in the MA Cm2 Regime and Artificial Synaptic Behaviour," *Nat. Nanotechnol.*, vol. 14, 2019.

[17] U. Zschieschang and H. Klauk, "Organic Transistors on Paper: A Brief Review," *J. Mater. Chem. C*, vol. 7, 2019.

[18] D.Griffiths, *Introduction to quantum mechanics*. Pearson, 2014.

[19] S. Maekawa, "Magnetism: A flood of spin current," *Nature Materials*, vol. 8, pp. 777 – 778, 2009.

[20] K. Takanashi, "Generation and control of spin current in magnetic nanostructures," *AAPPS Bulletin*, vol. 18, pp. 47 – 51, 2008.

[21] S.-Q. Shen, "Spintronics and spin current," *AAPPS Bulletin*, vol. 18, pp. 29 – 36, 2008.

[22] I. Zutic, J. Fabian, and S. Das Sarma, "Spintronics: Fundamentals and applications," *Rev. Mod. Phys.*, vol. 76, pp. 323–410, 2004.

[23] P. A. M. Dirac, "The quantum theory of the electron," *Proc. R. Soc. Lond. A*, vol. 117, p. 610–624, 1928.

[24] K. V. Shanavas, Z. S. Popović, and S. Satpathy, "Theoretical model for Rashba spin-orbit interaction in d electrons," *Phys. Rev. B*, vol. 90, p. 165108, 2014.

[25] R. J. Elliott, "Theory of the effect of spin-orbit coupling on magnetic resonance in some semiconductors," *Phys. Rev.*, vol. 96, pp. 266–279, 1954.

[26] Y. Yafet, *g Factors and Spin-Lattice Relaxation of Conduction Electrons*. 1963.

[27] M. Dyakonov and V. Perel, "Current-induced spin orientation of electrons in semiconductors," *Physics Letters A*, vol. 35, pp. 459–460, 1971.

[28] A. Privitera, M. Righetto, F. Cacialli, and M. K. Riede, "Perspectives of Organic and Perovskite-Based Spintronics," *Adv. Optical Mater*, vol. 9, p. 2100215, 2021.

[29] M. I. D'yakonov and V. I. Perel, "Optical orientation in a system of electrons and lattice nuclei in semiconductors. Theory," *Sov. Phys. JETP*, vol. 38, pp. 177–183, 1974.

[30] L. Guo, Y. Qin, X. Gu, X. Zhu, Q. Zhou, and X. Sun, "Spin transport in organic molecules," *Frontiers in Chemistry*, vol. 7, pp. 1–11, 2019.

[31] S. Watanabe, K. Ando, K. Kang, S. Mooser, Y. Vaynzof, H. Kurebayashi, E. Saitoh, and H. Sirringhaus, "Polaron spin current transport in organic semiconductors," *Nature Physics*, vol. 10, pp. 308–313, 2014.

[32] E. Vetter, I. VonWald, S. Yang, L. Yan, S. Koohfar, D. Kumah, Z.-G. Yu, W. You, and D. Sun, "Tuning of spin-orbit coupling in metal-free conjugated polymers by structural conformation," *Physical Review Materials*, vol. 4, pp. 1–8, 2020.

[33] D. Sun, K. J. van Schooten, M. Kavand, H. Malissa, C. Zhang, M. Groesbeck, C. Boehme, and Z. V. Vardeny, "Inverse spin hall effect from pulsed spin current in organic semiconductors with tunable spin-orbit coupling.," *Nature Materials*, vol. 15, pp. 863–869, 2016.

[34] L. Nuccio, M. Willis, L. Schulz, S. Fratini, F. Messina, M. D'Amico, F. L. Pratt, J. S. Lord, I. McKenzie, M. Loth, B. Purushothaman, J. Anthony, M. Heeney, R. M. Wilson, I. Hernández, M. Cannas, K. Sedlak, T. Kreouzis, W. P. Gillin, C. Bernhard, and A. J. Drew, "Importance of Spin-Orbit Interaction for the Electron Spin Relaxation in Organic Semiconductors," *Phys. Rev. Lett.*, vol. 110, p. 216602, 2013.

[35] Z. G. Yu, "Spin-orbit coupling and its effects in organic solids," *Physical Review B*, vol. 85, p. 115201, 2012.

[36] H. Liu, J. Wang, A. Chanana, and Z. V. Vardeny, "Studies of spin transport in fullerene films," *Journal of Applied Physics*, vol. 125, p. 142908, 2019.

[37] U. Chopra, S. Shambhawi, S. A. Egorov, J. Sinova, and E. R. McNellis, "Accurate and general formalism for spin-mixing parameter calculations," *Physical Review B*, vol. 100, p. 134410, 2019.

[38] U. Chopra, S. A. Egorov, J. Sinova, and E. R. McNellis, "Chemical and Structural Trends in the Spin-Admixture Parameter of Organic Semiconductor Molecules," *Journal of Physical Chemistry C*, vol. 123, pp. 19112–19118, 2019.

[39] S.-J. Wang, D. Venkateshvaran, M. R. Mahani, U. Chopra, E. R. McNellis, R. D. Pietro, S. Schott, A. Wittmann, G. Schweicher, M. Cubukcu, K. Kang, R. Carey, T. J. Wagner, J. N. M. Siebrecht, D. P. G. H. Wong, I. E. Jacobs, R. O. Aboljadayel, A. Ionescu, S. A. Egorov, S. Mueller, O. Zadvorna, P. Skalski, C. Jellett, M. Little, A. Marks, I. McCulloch, J. Wunderlich, J. Sinova, and H. Sirringhaus, "Long spin diffusion lengths in doped conjugated polymers due to enhanced exchange coupling.," *Nature Electronics*, vol. 2, pp. 98–107, 2019.

[40] S. Schott, E. R. McNellis, C. B. Nielsen, H.-Y. Chen, S. Watanabe, H. Tanaka, I. McCulloch, K. Takimiya, J. Sinova, and H. Sirringhaus, "Tuning the effective spin-orbit coupling in molecular semiconductor," *Nature Communications*, vol. 8, pp. 1–10, 2017.

[41] C. Nicolaides, E. Nicolaidou, P. Papagiorgis, G. Itskos, S. C. Hayes, and T. Trypiniotis, "Effect of structural conformation of conjugated polymers on spin transport," *Physical Review Materials*, vol. 6, p. 095601, 2022.

[42] P. A. Bobbert, "What makes the spin relax?," *Nature Materials*, vol. 9, pp. 288–290, 2010.

[43] Z. G. Yu, F. Ding, and H. Wang, "Hyperfine interaction and its effects on spin dynamics in organic solids," *Phys. Rev. B*, vol. 87, p. 205446, 2013.

[44] T. D. Nguyen, G. Hukic-Markosian, F. Wang, L. Wojcik, X.-G. Li, E. Ehrenfreund, and Z. V. Vardeny, "Isotope effect in spin response of O€-conjugated polymer films and devices," *Nature Materials*, vol. 9, p. 345–352, 2010.

[45] Q. Lu, S. Xie, and F. Qu, "Hopping-Dominated Spin Transport in Unintentionally Doped Organic Semiconductors," *Journal of Physical Chemistry Letters*, vol. 12, p. 3540–3544, 2021.

[46] M. Kimata, D. Nozaki, Y. Niimi, H. Tajima, and Y. Otani, "Spin relaxation mechanism in a highly doped organic polymer film," *Physical Review B*, vol. 91, p. 224422, 2015.

[47] Q. Lu, S. Yin, T. Gao, W. Qin, S. Xie, F. Qu, and A. Saxena, "Spin Transport Based on Exchange Coupling in Doped Organic Polymers," *Journal of Physical Chemistry Letters*, vol. 11, pp. 1087–1092, 2020.

[48] S. Jiang, S. Liu, P. Wang, Z. Z. Luan, X. D. Tao, H. F. Ding, and D. Wu, "Exchange-Dominated Pure Spin Current Transport in Alq3 Molecules," *Physical Review Letters*, vol. 115, pp. 1–5, 2015.

[49] N. Nagaosa, J. Sinova, S. Onoda, A. H. MacDonald, and N. P. Ong, "Anomalous Hall effect," *Rev. Mod. Phys.*, vol. 82, pp. 1539–1592, 2010.

[50] M. I. Dyakonov and V. . I. Perel, "Spin orientation of electrons associated with the interband absorption of light in semiconductors," *JETP*, vol. 33, no. 5, p. 1053, 1970.

[51] J. E. Hirsch, "Spin hall effect," *Phys. Rev. Lett.*, vol. 83, pp. 1834–1837, 1999.

[52] Y. K. Kato, R. C. Myers, A. C. Gossard, and D. D. Awschalom, "Observation of the spin hall effect in semiconductors," *Science*, vol. 306, no. 5703, pp. 1910–1913, 2004.

[53] S. O. Valenzuela and M. Tinkham, "Direct electronic measurement of the spin Hall effect," *Nature*, vol. 442, pp. 176–179, 2006.

[54] M. Farle, "Ferromagnetic resonance of ultrathin metallic layers," *Rep. Prog. Phys.*, vol. 61, 1998.

[55] T. Gilbert *Phys. Rev.*, vol. 100, p. 1243, 1955.

[56] T. Gilbert *IEEE Trans. Mag.*, vol. 40, p. 3443, 2004.

[57] W.Lowrie, *Fundamentals of Geophysics.* Oxford University Press, 2007.

[58] B. Heinrich and J. F. Cohran *Adv. Phys. Phys.*, vol. 42, pp. 523–639, 1993.

[59] Z. Celinski, K. B. Urquhart, and B. Heinrich *J. Magn. Mater.*, vol. 166, pp. 6–26, 1997.

[60] J. Smith and H. G. Beljers *Phillips Res. Rep.*, vol. 113, no. 10, 1955.

[61] J. O. Artmann *Phys. Rev.*, vol. 105, pp. 74–84.

[62] L. Baselgia, F. Wardner, S. L. Hutton, J. E. Drumbeller, J. Q. He, P. Wigen, and M. Marysko *Phys. Rev. B*, vol. 39, no. 865, 1988.

[63] B. Heinrich, D. Fraitova, and V. Kambersky *Phys. Stat. Sol.*, vol. 23, no. 501, 1967.

[64] J. Bland and B. Heinrich, *Ultrathin Magnetic Structures III. Fundamentals of Nanomagnetisms.* Springer-Verlag, Berlin Heidelberg, 2005.

[65] V. Kambersky, "On ferromagnetic resonance damping in metals," *Czech. J. Phys. B.*, vol. 26, pp. 1366–1383, 1976.

[66] V. Kambersky and C. E. Patton, "Spin-wave relaxation and phenomenological damping in ferromagnetic resonance," *Phys. Rev. B.*, vol. 11, pp. 2668–2672, 1975.

[67] K. Gilmore, Y. Idzerda, and M. Stiles, "Identification of the dominant precession damping mechanism in fe, co and ni by first-principles calculations.," *Phys. Rev. Lett.*, vol. 99, p. 027204, 2007.

[68] H. Suhl, "Theory of the magnetic damping constant.," *IEEE Trans. Magn.*, vol. 34, pp. 1834–1838, 1998.

[69] H. A. Sodano and J. S. Bae, "Eddy current damping in structures," *The Shock and Vibration Digest*, vol. 36, no. 6, pp. 469–478, 2004.

[70] B. Heinrich, R. Urban, and G. Wolterdorf, "Magnetic relaxation in metallic films. single and multilayers structures.," *J. Appl. Phys.*, vol. 91, pp. 7523–7525, 2002.

[71] R. D. McMichael and P. Krivosik, "Classical model of extrinsic ferromagnetic resonance linewidth in ultrathin films.," *IEEE Transactions on magnetics*, vol. 40, no. 1, 2004.

[72] M. Sparks, *Ferromagnetic Relaxation Theory.* Mc-Graw-Hill, New York, 1966.

[73] C. E. Patton, C. H. Wilts, and F. Humphrey, "Relaxation processes for ferromagnetic resonance in thin films.," *J. Appl. Phys.*, vol. 38, pp. 1358–1359, 1967.

[74] R. D. McMichael, M. D. Stiles, P.J.Chen, and W.F.Egelhoff *Jr. J. Appl. Phys.*, vol. 83, no. 7037, 1998.

[75] R. Arias and D. L. Mills, "Extrinsic contributions to the ferromagnetic resonance response of ultrathin films.," *Phys. Rev. B.*, vol. 60, pp. 7395–7409, 1999.

[76] P. Landeros, R. Arias, and D. L. Mills, "Two magnon scattering in ultrathin ferromagnetism: The case where the magnetization is out of plane.," *Phys. Rev. B.*, vol. 77, 2008.

[77] G. Woltersdorf and B. Heinrich, "Two-magnon scattering in a self-assempled nanoscale network of misfit dislocations.," *Phys. Rev. B.*, vol. 69, 2004.

[78] A. Azevedo, A. B. Oliveira, F. M. de Aguiar, and S. M. Rezende, "Extrinsic contributions to spin-wave damping and renormalization in thin $Ni_{50}Fe_{50}$ film," *Physical Review B*, vol. 62, pp. 5331–5333, 2000.

[79] R. D. McMichael, D. J. Twisselmann, and A. Kunz *Phys. Rev. Lett.*, vol. 90, 2003.

[80] M. S.Valenzuela, "Electrical detection of spin currents: The spin-current induced hall effect," *Journal of applied physics*, vol. 101, p. 09B103, 2007.

[81] M.Prins et al. *Journal of Physics: Condensed Matter*, vol. 7, no. 49, p. 9447, 1995.

[82] "Effect of spin diffusion on Gilbert damping for a very thin permalloy layer in Cu/permalloy/Cu/Pt film,"

[83] Y. Tserkovnyak, A. Brataas, and G. Bauer, "Spin pumping and magnetization dynamics in metallic multilayers," *Physical Review B*, vol. 66, p. 224403, 2002.

[84] P. W. Brouwer, "Scattering approach to parametric pumping.," *Phys. Rev. B*, vol. 58, 1998.

[85] A. Brataas, Y.V.Nazarov, and G. E. W. Bauer, "Spin transport in multi-terminal normal metal-ferromagnet systems with non-collinear magnetizations.," *The European Physical Journal B.*, vol. 22, 2001.

[86] Y. Tserkovnyak, A. Brataas, G. Bauer, and B. Halperin, "Nonlocal magnetization dynamics in ferromagnetic heterostructures," *Rev. Mod. Phys*, vol. 77, p. 1375, 2005.

[87] S.Maekawa, S. O. Valenzuela, E. Saitoh, and T. Kimura, *Spin Current*. Oxford University Press, 2012.

[88] A. Brataas, Y.V.Nazarov, and G. E. W. Bauer *Phys. Rev. Lett.*, vol. 84, 2000.

[89] G. Woltersdorf, *Spin-pumping and two-magnon scattering in magnetic multilayers. PhD thesis.* 2004.

[90] S. S. Kalarickal, P. Krivosik, M. Wu, C. E. Patton, M. L. Schneider, P. Kabos, T. J. Silva, and J. P. Nibarger, "Ferromagnetic resonance linewidth in metallic thin films: Comparison of measurement methods," *Journal of Applied Physics*, vol. 99, p. 093909, 2006.

[91] J.-C. Rojas-Sánchez, M. Cubukcu, A. Jain, C. Vergnaud, C. Portemont, C. Ducruet, A. Barski, A. Marty, L. Vila, J.-P. Attané, E. Augendre, G. Desfonds, S. Gambarelli, H. Jaffrès, J.-M. George, and M. Jamet, "Spin pumping and inverse spin Hall effect in germanium," *Phys. Rev. B*, vol. 88, p. 064403, 2013.

[92] K. Ando, S. Takahashi, J. Ieda, Y. Kajiwara, H. Nakayama, T. Yoshino, K. Harii, Y. Fujikawa, M. Matsuo, S. Maekawa, and E. Saitoh, "Inverse spin-hall effect

induced by spin pumping in metallic system," *Journal of Applied Physics*, vol. 109, no. 10, 2011.

[93] H. Wang, C. Du, Y. Pu, R. Adur, P. Hammel, and F. Yang, "Scaling of Spin Hall Angle in 3d, 4d, and 5d Metals from $Y_3Fe_5O_{12}$/Metal Spin Pumping," *Phys. Rev. Lett.*, vol. 112, p. 197201, 2014.

[94] F. D. Czeschka, L. Dreher, M. S. Brandt, M. Weiler, M. Althammer, I. M. Imort, G. Reiss, A. Thomas, W. Schoch, W. Limmer, H. Huebl, R. Gross, and S. T. B. Goennenwein, "Scaling behavior of the spin pumping effect in ferromagnet platinum bilayers.," *Phys. Rev. Lett.*, vol. 107, p. 046601, 2011.

[95] P. Deorani and H. Yang, "Role of spin mixing conductance in spin pumping: Enhancement of spin pumping efficiency in Ta/Cu/Py structures," *Appl. Phys. Lett.*, vol. 103, p. 232408, 2013.

[96] A. Ruiz-Calaforra, T. Brächer, V. Lauer, P. Pirro, B. Heinz, M. Geilen, A. V. Chumak, A. Conca, B. Leven, and B. Hillebrands, "The role of the non-magnetic material in spin pumping and magnetization dynamics in NiFe and CoFeB multilayer systems," *Journal of Applied Physics*, vol. 117, p. 163901, 2015.

[97] A. Wittmann, G. Schweicher, K. Broch, J. Novak, V. Lami, D. Cornil, E. R. McNellis, O. Zadvorna, D. Venkateshvaran, K. Takimiya, Y. H. Geerts, J. Cornil, Y. Vaynzof, J. Sinova, S. Watanabe, and H. Sirringhaus, "Tuning Spin Current Injection at Ferromagnet-Nonmagnet Interfaces by Molecular Design," *Phys. Rev. Lett.*, vol. 124, p. 027204, 2020.

[98] E. Saitoh, M. Ueda, H. Miyajima, and G. Tatara, "Conversion of spin current into charge current at room temperature : Inverse spin- Hall effect," *Applied Physics Letters*, vol. 88, p. 182509, 2006.

[99] K. Ando, Y. Kajiwara, K. Sasage, K. Uchida, and E. Saitoh, "Inverse Spin-Hall Effect Induced by Spin Pumping in Various Metals," *IEEE Transactions on Magnetics*, vol. 46, pp. 3694–3696, 2010.

[100] K. Ando and E. Saitoh, "Observation of the inverse spin hall effect in silicon," *Nature Communications*, 2012.

[101] M. Jamali, J. S. Lee, J. S. Jeong, F. Mahfouzi, Y. Lv, Z. Zhao, B. K. Nikolić, K. A. Mkhoyan, N. Samarth, and J.-P. Wang, "Giant Spin Pumping and Inverse Spin Hall Effect in the Presence of Surface and Bulk Spin-Orbit Coupling of Topological Insulator Bi_2Se_3," *Nano Lett*, vol. 15, p. 7126–7132, 2015.

[102] M. Kimata, H. Chen, K. Kondou, S. Sugimoto, P. K. Muduli, M. Ikhlas, Y. Omori, T. Tomita, A. H. MacDonald, S. Nakatsuji, and Y. Otani, "Magnetic and magnetic inverse spin Hall effects in a non-collinear antiferromagnet," *Nature*, vol. 565, p. 627–630, 2019.

[103] K. Ando, S. Takahashi, J. Ieda, H. Kurebayashi, T. Trypiniotis, C. H. W. Barnes, S. Maekawa, and E. Saitoh, "Electrically tunable spin injector free from the impedance mismatch problem," *Nature Materials*, vol. 10, p. 655–659, 2011.

[104] K. Ando, Y. Kajiwara, S. Takahashi, S. Maekawa, K. Takemoto, M. Takatsu, and E. Saitoh, "Angular dependence of inverse spin–hall effect induced by spin pumping investigated in a $ni_{81}fe_{19}$/Pt thin film," *Phys. Rev. B*, vol. 78, p. 014413, 2008.

[105] X. Tao, Q. Liu, B. Miao, R. Yu, Z. Feng, L. Sun, B. You, J. Du, K. Chen, S. Zhang, L. Zhang, Z. Yuan, D. Wu, and H. Ding, "Self-consistent determination of spin Hall angle and spin diffusion length in Pt and Pd: The role of the interface spin loss," *Science Advances*, vol. 4, p. eaat1670, 2018.

[106] B. Heinrich, Y. Tserkovnyak, G. Woltersdorf, A. Brataas, R. Urban, and G. E. W. Bauer, "Dynamic Exchange Coupling in Magnetic Bilayers," *Phys. Rev. Lett.*, vol. 90, p. 187601, 2003.

[107] Y. Li, Y. Li, R. Sun, N. Li, Z.-Z. Gong, X. Yang, Z.-K. Xie, H.-L. Liu, W. He, X.-Q. Zhang, and Z.-H. Cheng, "Anomalous Gilbert damping induced by the coexisting static and dynamic coupling in Fe/Pd/Fe trilayers," *Phys. Rev. B*, vol. 104, p. 094409, 2021.

[108] P. Omelchenko, E. Girt, and B. Heinrich, "Test of spin pumping into proximity-polarized Pt by in-phase and out-of-phase pumping in Py/Pt/Py," *Phys. Rev. B*, vol. 100, p. 144418, 2019.

[109] H. Yang, Y. Li, and W. E. Bailey, "Large spin pumping effect in antisymmetric precession of $Ni_{79}Fe_{21}$/Ru/$Ni_{79}Fe_{21}$," *Appl. Phys. Lett.*, vol. 108, p. 242404, 2016.

[110] G. Joshi, M. Y. Teferi, R. Miller, S. Jamali, D. Baird, J. V. Tol, H. Malissa, J. M. Lupton, and C. Boehme, "Isotropic Effective Spin-Orbit Coupling in a Conjugated Polymer," *Journal of the American Chemical Society*, vol. 140, pp. 6758–6762, 2018.

[111] V. V. Khramtsov, A. A. Bobko, M. Tseytlin, and B. Driesschaert, "Electron Paramagnetic Resonance Spectra of the Nitroxyl and Trityl Radicals: Multifunctional Spectroscopy and Imaging of Local Chemical Microenvironment," *Analytical Chemistry*, vol. 89, pp. 4758–4771, 2017.

[112] R. S. Alger, *Electron Paramagnetic Resonance:Techniques and applications*. John Wiley, 1968.

[113] C. P. Poole and H. A. Farach, *Relaxation in Magnetic Resonance*. Academic, 1971.

[114] J. Tsurumi, H. Matsui, T. Kubo, R. Häusermann, C. Mitsui, T. Okamoto, S. Watanabe, and J. Takeya, "Coexistence of ultra-long spin relaxation time and coherent charge transport in organic single-crystal single-crystal semiconductors," *Nature Physics*, vol. 13, pp. 994–999, 2017.

[115] A. Abragam and H. A. Farach, *The Principles of Nuclear Magnetism*. Oxford University Press, 1961.

[116] H. Matsui, A. S. Mishchenko, and T. Hasegawa, "Distribution of Localized States from Fine Analysis of Electron Spin Resonance Spectra in Organic Transistors," *Phys. Rev. Lett.*, vol. 104, p. 056602, 2010.

[117] *Operation Manual of ADANI CMS-8400 EPR spectrometer.*

[118] S. Stoll and A. Schweiger, "Easyspin, a comprehensive software package for spectral simulation and analysis in epr.," *J. Phys.: Condens. Matter*, vol. 178, pp. 42–55, 2006.

[119] A. C. Savva, S. I. Mirallai, G. A. Zissimou, A. A. Berezin, M. Demetriades, A. Kourtellaris, C. P. Constantinides, C. Nicolaides, T. Trypiniotis, and P. A.

Koutentis, "Preparation of blatter radicals via aza-wittig chemistry: The reaction of n-aryliminophosphoranes with 1-(het)aroyl-2-aryldiazenes," *Journal of Organic Chemistry*, vol. 82, pp. 7564–7575, 2017.

[120] F. A. Perras, D. F. Flesariu, S. A. Southern, C. Nicolaides, J. D. Bazak, N. Washton, T. Trypiniotis, C. Constantinides, and P. Koutentis, "Methyl-driven overhauser dynamic nuclear polarization," *Journal of Physical Chemistry Letters*, vol. 13, pp. 4000–4006, 2022.

[121] C. Nicolaides and T. Trypiniotis, "Metal-free organic radical spin source.," *Nanoletters*, 2023.

[122] G. A. Zissimou, A. A. Berezin, M. Manoli, C. Nicolaides, T. Trypiniotis, and P. A. Koutentis, "3,3',3"-(Benzene-1,3,5-triyl)tris(1-phenyl-1H-benzo[e][1,2,4]triazin-4-yl): A C3 symmetrical Blatter-type triradical.," *Tetrahedron*, vol. 76, p. 131077, 2020.

[123] C. Nicolaides, A. Papachristodoulou, and T. Trypiniotis, "Demonstration of spin transport and inverse spin hall effect in geoi at room temperature.," in *CTMNM/NAGC workshop, oral presentation*, 2017.

[124] Z. Q. Qiu and S. D. Bader, "Surface magnetooptic kerr effect," *Review of Scientific Instruments*, vol. 71, no. 3, pp. 1243–1255, 2000.

[125] J. Hamrle, S. Blomeier, O. Gaier, B. Hillebrands, H. Schneider, G. Jakob, K. Postava, and C. Felser, "Huge quadratic magnetooptical kerr effect and magnetization reversal in the co 2 fesi heusler compound," *Journal of Physics D: Applied Physics*, vol. 40, no. 6, p. 1563, 2007.

[126] P.Eaton and P. West, *Atomic Force Microscopy*. Oxford University Press, 2010.

[127] *AFM-WORKSHOP, TT-AFM, User's Guide*.

[128] C. Nicolaides and T. Trypiniotis, "Spin pumping across hybrid organic-inorganic perovskite / ferromagnet interface: the effect of ferromagnet morphology.," *Journal of Applied Physics*, 2023.

[129] P. Papagiorgis, A. Manoli, L. Protesescu, C. Achilleos, M. Violaris, C. Nicolaides, T. Trypiniotis, M. I. Bodnarchuk, M. V. Kovalenko, A. Othonos, and G. Itskos,

"Efficient Optical Amplification in the Nanosecond Regime from Formamidinium Lead Iodide Nanocrystals," *ACS Photonics*, vol. 5, p. 907–917, 2018.

[130] S. Ozaki, Y. Wada, and K. Noda, "Hall-effect measurement for inkjet-deposited films of poly(3,4-ethylenedioxythiophene)/poly(4-styrenesulfonate) by using microscale gap electrodes.," *Physical Review Materials*, vol. 215, p. 28, 2016.

[131] L. F. Yin, D. H. Wei, N. Lei, L. H. Zhou, C. S. Tian, G. S. Dong, X. F. Jin, L. P. Guo, Q. J. Jia, and R. Q. Wu, "Magnetocrystalline anisotropy in permalloy revisited.," *Phys. Rev. Lett.*, vol. 97, p. 067203, 2006.

[132] K. Ando, S. Watanabe, S. Mooser, E. Saitoh, and H. Sirringhaus, "Solution-processed organic spin-charge converter.," *Nature Materials*, vol. 12, pp. 622–627, 2013.

[133] P. Wang, L. Zhou, S. Jiang, Z. Luan, D. Shu, H. Ding, and D. Wu, "Unidirectional spin-wave-propagation-induced seebeck voltage in a pedot:pss/yig bilayer.," *Phys. Rev. Lett.*, vol. 120, p. 047201, 2018.

[134] M. M. Qaid, T. Richter, A. Müller, C. Hauser, C. Ballani, and G. Schmidt, "Radiation damping in ferromagnetic resonance induced by a conducting spin sink.," *Phys. Rev. B*, vol. 96, p. 184405, 2017.

[135] M. M. Qaid, M. R. Mahani, J. Sinova, and G. Schmidt, "Quantifying the inverse spin-hall effect in highly doped pedot:pss.," *Physical Review Research*, vol. 2, pp. 1–8, 2020.

[136] T. An, V. I. Vasyuchka, K. Uchida, A. V. Chumak, K. Yamaguchi, K. Harii, J. Ohe, M. B. Jungfleisch, Y. Kajiwara, H. Adachi, B. Hillebrands, S. Maekawa, and E. Saitoh, "Unidirectional spin-wave heat conveyer.," *Nature Materials*, vol. 12, p. 549–553, 2013.

[137] N. Kim, I. Petsagkourakis, S. Chen, M. Berggren, X. Crispin, M. P. Jonsson, and I. Zozoulenko, *Electric Transport Properties in PEDOT Thin Films.* Conjugated Polymers, 2019.

[138] A. Elschner, S. Kirchmeyer, W. Lovenich, U. Merker, and K. Reuter, *PEDOT:Principles and applications of an intrinsically conductive polymer*. CRC Press, 2010.

[139] Y. Wen and J. Xu, "Scientific Importance of Water-Processable PEDOT–PSS and Preparation, Challenge and New Application in Sensors of Its Film Electrode: A Review," *Polymer Chemistry*, vol. 55, pp. 1121–1150, 2017.

[140] L. Manjakkal, A. Pullanchiyodan, N. Yogeswaran, E. S. Hosseini, and R. Dahiya, "A Wearable Supercapacitor Based on Conductive PEDOT:PSS-Coated Cloth and a Sweat Electrolyte," *Advanced Materials*, vol. 32, p. 1907254, 2020.

[141] S. Takamatsu, T. Lonjaret, D. Crisp, J.-M. Badier, G. G. Malliaras, and E. Ismailova, "Direct patterning of organic conductors on knitted textiles for long-term electrocardiography," *Scientific Reports*, vol. 5, p. 15003, 2015.

[142] D. Khodagholy, J. Rivnay, M. Sessolo, M. Gurfinkel, P. Leleux, L. H. Jimison, E. Stavrinidou, T. Herve, S. Sanaur, R. M. Owens, and G. G. Malliaras, "High transconductance organic electrochemical transistors," *Nature Communications*, vol. 4, p. 2133, 2013.

[143] J. G. Tait, B. J. Worfolk, S. A. Maloney, T. C. Hauger, A. L. Elias, J. M. Buriak, and K. D. Harris, "Spray coated high-conductivity PEDOT:PSS transparent electrodes for stretchable and mechanically-robust organic solar cells," *Solar Energy Materials and Solar Cells*, vol. 110, pp. 98–106, 2013.

[144] Z. Zhang, G. Tian, X. Duan, H. lan Chen, and D. H. K. Richie, "Nanostructured PEDOT Coatings for Electrode–Neuron Integration," *ACS Applied Bio Materials*, vol. 4, pp. 5556–5565, 2021.

[145] G. Heywang and F. Jonas, "Poly(alkylenedioxythiophene)s - New, very stable conducting polymers," *Advanced Materials*, vol. 4, pp. 116–118, 1992.

[146] G. H. Kim, L. Shao, K. Zhang, and K. P. Pipe, "Engineered doping of organic semiconductors for enhanced thermoelectric efficiency," *Nature Materials*, vol. 12, pp. 10–14, 2013.

[147] X. Crispin, F. L. E. Jakobsson, A. Crispin, P. C. M. Grim, P. Andersson, A. Volodin, C. van Haesendonck, M. V. der Auweraer, W. R. Salaneck,

and M. Berggren, "The origin of the high conductivity of poly(3,4-ethylenedioxythiophene)- poly(styrenesulfonate) (PEDOT-PSS) plastic electrodes," *Chemistry of Materials*, vol. 18, pp. 4354–4360, 2006.

[148] O. Bubnova, Z. U. Khan, H. Wang, S. Braun, D. R. Evans, M. Fabretto, P. H. Talemi, D. Dagnelund, J. B. Arlin, Y. H. Geerts, S. Desbief, D. Breiby, J. Andreasen, R. Lazzaroni, W. M. Chen, I. Zozoulenko, M. Fahlman, P. J. Murphy, M. Berggren, and X. Crispin, "Semi-metallic polymers," *Nature Materials*, vol. 13, pp. 190–194, 2014.

[149] Y. Mochizuki, T. Horii, and H. Okuzaki, "Effect of pH on Structure and Conductivity of PEDOT/PSS," *Transactions of the Materials Research Society of Japan*, vol. 37, pp. 307–310, 2012.

[150] T. C. Tsai, H. C. Chang, C. H. Chen, Y. C. Huang, and W. T. Whang, "A facile dedoping approach for effectively tuning thermoelectricity and acidity of PEDOT:PSS films," *Organic Electronics*, vol. 15, pp. 641–645, 2014.

[151] H. M. Blatter and H. Lukaszewsk, "A new stable free radical," *Tetrahedron Letters*, vol. 9, pp. 2701–2705, 1968.

[152] Y. Ji, L. Long, and Y. Zheng, "Recent advances of stable Blatter radicals: Synthesis, properties and applications," *Materials Chemistry Frontiers*, vol. 4, pp. 3433–3443, 2020.

[153] A. Gardias, P. Kaszynski, E. Obijalska, D. Trzybinski, S. Domagała, K. Wozniak, and J. Szczytko, "Magnetostructural Investigation of Orthogonal 1-Aryl-3-Phenyl-1,4-Dihydrobenzo[e][1,2,4]triazin-4-yl Derivatives," *Chemistry - A European Journal*, vol. 24, pp. 1317–1329, 2018.

[154] T. Junghoefer, A. Calzolari, I. Baev, M. Glaser, F. Ciccullo, E. Giangrisostomi, R. Ovsyannikov, F. Kielgast, M. Nissen, J. Schwarz, N. M. Gallagher, A. Rajca, M. Martins, and M. B. Casu, "Magnetic behavior in metal-free radical thin films," *Chem*, vol. 8, pp. 801–814, 2022.

[155] J. H. Gallego, S. Sangtarash, R. Davidson, L. Rincón-García, A. Daaoub, G. R. Bollinger, C. J. Lambert, V. S. Oganesyan, M. R. Bryce, N. Agraït, and H. Sadeghi, "Thermoelectric Enhancement in Single Organic Radical Molecules," *Nano Letters*, vol. 22, pp. 948–953, 2022.

[156] C. P. Constantinides, P. A. Koutentis, H. Krassos, J. M. Rawson, and A. J. Tasiopoulos, "Characterization and magnetic properties of a "super stable" radical 1,3-diphenyl-7-trifluoromethyl-1,4-dihydro-1,2,4-benzotriazin-4-yl," *Journal of Organic Chemistry*, vol. 76, pp. 2798–2806, 2011.

[157] A. Saal, C. Friebe, and U. S. Schubert, "Blatter radical as a polymeric active material in organic batteries," *Journal of Power Sources*, vol. 524, p. 231061, 2022.

[158] Y. Zheng, M. S. Miao, M. C. Kemei, R. Seshadri, and F. Wudl, "The Pyreno-Triazinyl Radical – Magnetic and Sensor Properties," *J. Chem*, vol. 54, p. 774, 2014.

[159] L. A. J. Keane, S. I. Mirallai, M. Sweeney, M. P. Carty, G. A. Zissimou, A. A. Berezin, P. A. Koutentis, and F. Aldabbagh, "Anti-Cancer Activity of Phenyl and Pyrid-2-yl 1,3-Substituted Benzo[1,2,4]triazin-7-ones and Stable Free Radical Precursors," *Molecules*, vol. 23, p. 574, 2018.

[160] F. Ciccullo, N. M. Gallagher, O. Geladari, T. Chasse, A. Rajca, and M. B. Casu, "A Derivative of the Blatter Radical as a Potential Metal Free Magnet for Stable Thin Films and Interfaces," *ACS Applied Materials and Interfaces*, vol. 8, pp. 1805–1812, 2016.

[161] J. Z. Low, G. Kladnik, L. L. Patera, S. Sokolov, G. Lovat, E. Kumarasamy, J. Repp, L. M. Campos, D. Cvetko, A. Morgante, and L. Venkataraman, "The Environment-Dependent Behavior of the Blatter Radical at the Metal-Molecule Interface," *Nano Letters*, vol. 19, pp. 2543–2548, 2019.

[162] P. A. Koutentis and D. L. Re, "Catalytic Oxidation of N-Phenylamidrazones to 1,3-Diphenyl-1,4-dihydro-1,2,4-benzotriazin-4-yls: An Improved Synthesis of Blatter's Radical," *Synthesis*, vol. 2010, pp. 2075–2079, 2010.

[163] C. P. Constantinides, P. A. Koutentis, and G. Loizou, "Synthesis of 7-aryl/heteraryl-1,3-diphenyl-1,2,4-benzotriazinyls via palladium catalyzed Stille and Suzuki-Miyaura reactions.," *Organic and Biomolecular Chemistry*, vol. 9, pp. 3122–3125, 2011.

[164] K. Kobayashi, T. Kimura, H. Sawada, K. Terakura, and Y. Tokura, "Room-temperature magnetoresistance in an oxide material with an ordered double-perovskite structure.," *Nature.*, vol. 395, p. 677–680, 1998.

[165] R. E. Cohen, "Origin of ferroelectricity in perovskite oxides.," *Nature.*, vol. 358, p. 136–138, 1992.

[166] M. Kim, G. M. McNally, H.-H. Kim, M. Oudah, A. S. Gibbs, P. Manuel, R. J. Green, R. Sutarto, T. Takayama, A. Yaresko, U. Wedig, M. Isobe, R. K. Kremer, D. A. Bonn, B. Keimer, and H. Takagi, "Superconductivity in (ba,k)sbo3.," *Nature Materials.*, vol. 21, p. 627–633, 2022.

[167] T. M. Brenner, D. A. Egger, L. Kronik, G. Hodes, and D. Cahen, "Hybrid organic—inorganic perovskites: low-cost semiconductors with intriguing charge-transport properties," *Nature*, vol. 1, no. 7, pp. 1 – 16, 2016.

[168] Nam-Gyu Park, "Perovskite solar cells: an emerging photovoltaic technology," *Materials Today*, vol. 18, no. 2, pp. 65 – 72, 2015.

[169] J. Jeong, M. Kim, J. Seo, H. Lu, P. Ahlawat, A. Mishra, Y. Yang, M. A. Hope, F. T. Eickemeyer, M. Kim, Y. J. Yoon, I. W. Choi, B. P. Darwich, S. J. Choi, Y. Jo, J. H. Lee, B. Walker, S. M. Zakeeruddin, L. Emsley, U. Rothlisberger, A. Hagfeldt, D. S. Kim, M. Grätzel, and J. Y. Kim, "Pseudo-halide anion engineering for α-fapbi3 perovskite solar cells.," *Nature.*, vol. 592, p. 381–385, 2021.

[170] L. D. Wolf, J. Holovsky, S. J. Moon, P. Löper, B. Niesen, M. Ledinsky, F. J. Haug, J. Yum, and C. Ballif, "Organometallic halide perovskites: Sharp optical absorption edge and its relation to photovoltaic performance," *J. Phys. Chem. Lett.*, vol. 5, 2014.

[171] G. E. Eperon, S. D. Stranks, C. Menelaou, M. B. Johnston, L. M. Herz, and H. J. Snaith, "Formamidinium lead trihalide: A broadly tunable perovskite for efficient planar heterojunction solar cells.," *Energy Environ. Sci.*, vol. 7, 2014.

[172] C. R. Kagan, D. B. Mitzi, and C. D. Dimitrakopoulos, "Organic-inorganic hybrid materials as semiconducting channels in thin-film field- effect transistors.," *Science*, vol. 286, 1999.

[173] S. D. Stranks, G. E. Eperon, G. Grancini, C. Menelaou, M. J. Alcocer, T. Leijtens, L. M. Herz, A. Petrozza, and H. J. Snaith, "Electron-hole diffusion lengths exceeding 1 micrometer in an organometal trihalide perovskite absorber.," *Science*, vol. 342, 2013.

[174] J. Even, L. Pedesseau, J.-M. Jancu, and C. Katan, "Importance of spin–orbit coupling in hybrid organic/inorganic perovskites for photovoltaic applications," *The Journal of Physical Chemistry Letters*, vol. 4, no. 17, pp. 2999 – 3005, 2013.

[175] D. Giovanni, H. Ma, J. Chua, and M. Gratzel, "Highly spin-polarized carrier dynamics and ultralarge photoinduced magnetization in ch3nh3pbi3 perovskite thin films," *Nanoletters*, vol. 15, no. 3, pp. 1553 – 1558, 2015.

[176] J. Wang, C. Zhang, H. Liu, R. McLaughlin, Y. Zhai, S. R. Vardeny, X. Liu, S. McGill, D. Semenov, H. Guo, R. Tsuchikawa, V. V. Deshpande, and D. Sun, "Spin-optoelectronic devices based on hybrid organic-inorganic trihalide perovskites.," *Nature Communications*, vol. 10, pp. 1–6, 2019.

[177] Y.-H. Kim, Y. Zhai, H. Lu, Xin, C. Xiao, E. A. Gaulding, S. P. Harvey, J. J. Berry, Z. V. Vardeny, J. M. Luther, and M. C. Beard, "Chiral-induced spin selectivity enables a room-temperature spin light-emitting diode.," *Science*, vol. 371, pp. 1129–1133, 2021.

[178] M. Kepenekian, R. Robles, C. Katan, D. Sapori, L. Pedesseau, and J. Even, "Rashba and dresselhaus effects in hybrid organic–inorganic perovskites: From basics to devices," *ACS Publications Nanoletters*, vol. 9, no. 12, pp. 11557 – 11567, 2015.

[179] R. Singh, S. R. Suranagi, M. Kumar, and V. K. Shukla, "Investigations on the role of mixed-solvent for improved efficiency in perovskite solar cell.," *Journal of Applied Physics*, vol. 122, p. 235302, 2017.

[180] V. A. Dediu, L. E. Hueso, I. Bergenti, and C. Taliani, "Spin routes in organic semiconductors," *Nature Materials*, vol. 8, pp. 707–716, 2009.

[181] S. Schott, U. Chopra, V. Lemaur, A. Melnyk, Y. Olivier, R. D. Pietro, I. Romanov, R. L. Carey, X. Jiao, C. Jellett, M. Little, A. Marks, C. R. McNeill, I. McCulloch, E. R. McNellis, D. Andrienko, D. Beljonne, J. Sinova,

and H. Sirringhaus, "Polaron spin dynamics in high-mobility polymeric semiconductors," *Nature Physics*, vol. 15, pp. 814–822, 2019.

[182] G. Rebetez, O. Bardagot, J. Affolter, J. Réhault, and N. Banerji, "What Drives the Kinetics and Doping Level in the Electrochemical Reactions of PEDOT:PSS?," *Advanced Functional Materials*, vol. 32, p. 2105821, 2022.

[183] B. D. Paulsen, R. Wu, C. J. Takacs, H.-G. Steinrück, J. Strzalka, Q. Zhang, M. F. Toney, and J. Rivnay, "Time-Resolved Structural Kinetics of an Organic Mixed Ionic – Electronic Conductor," *Advanced Materials*, vol. 32, p. 2003404, 2020.

[184] I. Zozoulenko, A. Singh, S. K. Singh, V. Gueskine, X. Crispin, and M. Berggren, "Polarons, Bipolarons, And Absorption Spectroscopy of PEDOT," *ACS Applied Polymer Materials*, vol. 1, pp. 83–94, 2019.

[185] M. Łapkowski and A. Pron, "Electrochemical oxidation of poly(3,4-ethylenedioxythiophene) - 'in situ' conductivity and spectroscopic investigations," *Synthetic Metals*, vol. 110, pp. 79–83, 2000.

[186] G. A. H. Wetzelaer, L. J. A. Koster, and P. M. Blom, "Validity of the einstein relation in disordered organic semiconductors," *Physical Review Letters*, vol. 107, p. 066605, 2011.

[187] K. Kang, ShunWatanabe, K. Broch, A. Sepe, A. Brown, I. Nasrallah, M. Nikolka, Z. Fei, M. Heeney, D. Matsumoto, K. Marumoto, H. Tanaka, S. ichi Kuroda, and H. Sirringhaus, "2D coherent charge transport in highly ordered conducting polymers doped by solid state diffusion," *Nature Materials*, vol. 15, pp. 896–902, 2016.

[188] Q. Wei, M. Mukaida, Y. Naitoh, and T. Ishida, "Morphological change and mobility enhancement in PEDOT:PSS by adding co-solvents," *Advanced Materials*, vol. 25, pp. 2831–2836, 2013.

[189] L.-M. Yu, T. Chen, N. Feng, R. Wang, T. Sun, Y. Zhou, H. Wang, Y. Yang, and Z.-H. Lu, "Highly Conductive and Wettable PEDOT:PSS for Simple and Efficient Organic/c-Si Planar Heterojunction Solar Cells," *Solar RRL*, vol. 4, p. 1900513, 2020.

[190] T. A. Yemata, Y. Zheng, A. K. K. Kyaw, X. Wang, J. Song, W. S. Chin, and J. Xu, "Modulation of the doping level of PEDOT:PSS film by treatment with hydrazine to improve the Seebeck coefficient," *RSC Advances*, vol. 10, pp. 1786–1792, 2020.

[191] A. Zykwinska, W. Domagala, and M. Lapkowski, "ESR spectroelectrochemistry of poly(3,4-ethylenedioxythiophene) (PEDOT)," *Electrochemistry Communications*, vol. 5, pp. 603–608, 2003.

[192] D. Neusser, C. Malacrida, M. Kern, Y. M. Gross, J. van Slageren, and S. Ludwigs, "High Conductivities of Disordered P3HT Films by an Electrochemical Doping Strategy," *Chemistry of Materials*, vol. 32, pp. 6003–6013, 2020.

[193] A. V. Volkov, S. K. Singh, E. Stavrinidou, R. Gabrielsson, J. F. Franco-Gonzalez, A. Cruce, W. M. Chen, D. T. Simon, M. Berggren, and I. V. Zozoulenko, "Spectroelectrochemistry and Nature of Charge Carriers in Self-Doped Conducting Polymer," *Advanced Electronic Materials*, vol. 3, p. 1700096, 2017.

[194] A. Privitera, R. Warren, G. Londi, P. Kaienburg, J. Liu, A. Sperlich, A. E. Lauritzen, O. Thimm, A. Ardavan, D. Beljonne, and M. Riede, "Electron spin as fingerprint for charge generation and transport in doped organic semiconductors," *Journal of Materials Chemistry C*, vol. 9, pp. 2944–2954, 2021.

[195] Y. Sakurai, D. Matsumoto, and K. Marumoto, "Electrically Controlled Dimensionality of Magnetic Systems in Organic Materials," *Applied Magnetic Resonance*, vol. 49, pp. 767–782, 2018.

[196] Z. G. Yu, "Spin Hall Effect in Disordered Organic Solids," *Physical Review Letters*, vol. 115, p. 026601, 2015.

[197] J. Lustikova, Y. Shiomi, and E. Saitoh, "Vector spectroscopy for spin pumping," *Physical Review B - Condensed Matter and Materials Physics*, vol. 92, p. 224436, 2015.

[198] R. Iguchi and E. Saitoh, "Measurement of spin pumping voltage separated from extrinsic microwave effects," *Journal of the Physical Society of Japan*, vol. 86, pp. 53–55, 2017.

[199] Z. Fan, P. Li, D. Du, and J. Ouyang, "Significantly Enhanced Thermoelectric Properties of PEDOT:PSS Films through Sequential Post-Treatments with Common Acids and Bases," *Adv. Energy Mater.*, vol. 7, p. 1602116, 2017.

[200] S. Yang, E. Vetter, T. Wang, A. Amassian, and D. Sun, "Observation of long spin lifetime in MAPbBr3 single crystals at room temperature," *J. Phys.: Mater*, vol. 3, p. 015012, 2020.

[201] X. Li, R. Zou, Z. Liu, J. Mata, B. Storer, Y. Chen, W. Qi, Z. Zhou, and P. Zhang, "Deciphering the superior thermoelectric property of post-treatment-free PEDOT:PSS/IL hybrid by X-ray and neutron scattering characterization," *npj Flexible Electronics*, vol. 6, pp. 1–7, 2022.

[202] A. E. Mansour, A. M. Valencia, D. Lungwitz, B. Wegner, N. Tanaka, Y. Shoji, T. Fukushima, A. Opitz, C. Cocchi, and N. Koch, "Understanding the evolution of the Raman spectra of molecularly p-doped poly(3-hexylthiophene-2,5-diyl): signatures of polarons and bipolarons," *Physical Chemistry Chemical Physics*, vol. 24, pp. 3109–3118, 2022.

[203] J. Gao, B. W. Stein, A. K. Thomas, J. A. Garcia, J. Yang, M. L. Kirk, and J. K. Grey, "Enhanced Charge Transfer Doping Efficiency in J-Aggregate Poly(3-hexylthiophene) Nanofibers," *J. Phys. Chem. C*, vol. 119, p. 16396–16402, 2015.

[204] J. R. Ferraro, *Introductory Raman Spectroscopy: Second Edition*. 2003.

[205] S. Wood, J. R. Hollis, and J.-S. Kim, "Raman spectroscopy as an advanced structural nanoprobe for conjugated molecular semiconductors," *Journal of Physics D: Applied Physics*, vol. 50, p. 073001, 2017.

[206] J. Nightingale, J. Wade, D. Moia, J. Nelson, and J.-S. Kim, "Impact of Molecular Order on Polaron Formation in Conjugated Polymers," *J. Phys. Chem. C*, vol. 122, pp. 29129–29140, 2018.

[207] S. Funda, T. Ohki, Q. Liu, J. Hossain, Y. Ishimaru, K. Ueno, and H. Shirai, "Correlation between the fine structure of spin-coated PEDOT:PSS and the photovoltaic performance of organic/crystalline-silicon heterojunction solar cells," *Journal of Applied Physics*, vol. 120, p. 033103, 2016.

[208] S. Garreau, J. Duvail, and G. Louarn, "Spectroelectrochemical studies of poly(3,4-ethylenedioxythiophene) in aqueous medium," *Synthetic Metals*, vol. 125, pp. 325–329, 2001.

[209] E. Tan, A. Pappa, C. Pitsalidis, S. Wood, F. A. Castro, R. M. Owens, J. Nightingale, and J. Kim, "A highly sensitive molecular structural probe applied to in situ biosensing of metabolites using PEDOT:PSS," *Biotechnology and Bioengineering*, vol. 117, pp. 291–299, 2019.

[210] S. Sakamoto, M. Okumura, Z. Zhao, and Y. Furukawa, "Raman spectral changes of PEDOT–PSS in polymer light-emitting diodes upon operation," *Chemical Physics Letters*, vol. 412, pp. 395–398, 2005.

[211] W. C. Tsoi, D. T. James, J. S. Kim, P. G. Nicholson, C. E. Murphy, D. D. C. Bradley, J. Nelson, and J.-S. Kim, "The Nature of In-Plane Skeleton Raman Modes of P3HT and Their Correlation to the Degree of Molecular Order in P3HT:PCBM Blend Thin Films," *J. Am. Chem. Soc*, vol. 133, pp. 9834–9843, 2011.

[212] K. Banerjee-Ghosh, O. B. Dor, F. Tassinari, E. Capua, S. Yochelis, A. Capua, S.-H. Yang, S. S. P. Parkin, S. Sarkar, L. Kronik, L. T. Baczewski, R. Naaman, and Y. Paltiel, "Separation of enantiomers by their enantiospecific interaction with achiral magnetic substrates," *Science*, vol. 360, pp. 1331–1334, 2018.

[213] O. B. Dor, S. Yochelis, A. Radko, K. Vankayala, E. Capua, A. Capua, S.-H. Yang, L. T. Baczewski, S. S. P. Parkin, R. Naaman, and Y. Paltiel, "Magnetization switching in ferromagnets by adsorbed chiral molecules without current or external magnetic field," *Nature Communications*, vol. 8, pp. 1–7, 2017.

[214] I. Ratera and J. Veciana, "Playing with organic radicals as building blocks for functional molecular materials," *Chemical Society Reviews*, vol. 41, pp. 303–349, 2012.

[215] C. Train, L. Norel, and M. Baumgarten, "Organic radicals, a promising route towards original molecule-based magnetic materials," *Coordination Chemistry Reviews*, vol. 253, pp. 2342–2351, 2009.

[216] H. M. McConnell, "Ferromagnetism in solid free radicals," *The Journal of Chemical Physics*, vol. 39, p. 1910, 1963.

[217] Q. Jiang, J. Zhang, Z. Mao, Y. Yao, D. Zhao, Y. Jia, D. Hu, and Y. Ma, "Room-Temperature Ferromagnetism in Perylene Diimide Organic Semiconductor," *Advanced Materials*, vol. 34, p. 2108103, 2022.

[218] Y. Shiomi and E. Saitoh, "Paramagnetic Spin Pumping," *Phys. Rev. Lett.*, vol. 113, p. 266602, 2014.

[219] K. Oyanagi, S. Takahashi, L. J. Cornelissen, J. Shan, S. Daimon, T. Kikkawa, G. E. Bauer, B. J. van Wees, and E. Saitoh, "Spin transport in insulators without exchange stiffness," *Nature Communications*, vol. 10, pp. 1–6, 2019.

[220] S. Okamoto, "Spin injection and spin transport in paramagnetic insulators," *Physical Review B*, vol. 93, p. 064421, 2016.

[221] Y. Ohnuma, H. Adachi, E. Saitoh, and S. Maekawa, "Enhanced dc spin pumping into a fluctuating ferromagnet near TC," *Physical Review B*, vol. 89, p. 174417, 2014.

[222] Y. Yamamoto, M. Ichioka, and H. Adachi, "Spin Seebeck effect in paramagnets and antiferromagnets at elevated temperatures," *Physical Review B*, vol. 100, p. 064419, 2019.

[223] K. Oyanagi, S. Takahashi, T. Kikkawa, and E. Saitoh, "Mechanism of paramagnetic spin Seebeck effect," *Physical Review B*, vol. 107, p. 014423, 2023.

[224] F. J. M. Rogers, P. L. Norcott, and M. L. Coote, "Recent advances in the chemistry of benzo [e][1,2,4]triazinyl radicals," *Organic Biomolecular Chemistry*, vol. 18, pp. 8255–8277, 2020.

[225] F. Ciccullo, A. Calzolari, K. Bader, P. Neugebauer, N. M. Gallagher, A. Rajca, J. van Slageren, and M. B. Casu, "Interfacing a Potential Purely Organic Molecular Quantum Bit with a Real-Life Surface," *ACS Applied Materials and Interfaces*, vol. 11, pp. 1571–1578, 2019.

[226] S. Zhang, M. Pink, T. Junghoefer, W. Zhao, S.-N. Hsu, S. Rajca, A. Calzolari, B. W. Boudouris, M. B. Casu, and A. Rajca, "High-Spin (S = 1) Blatter-Based Diradical with Robust Stability and Electrical Conductivity," *Journal of the American Chemical Society*, vol. 144, pp. 6059–6070, 2022.

[227] A. B. Rishu Khurana and M. E. Ali, "How Plausible Is Getting Ferromagnetic Interactions by Coupling Blatter's Radical via Its Fused Benzene Ring?," *Journal of Physical Chemistry A*, vol. 124, pp. 6707–6713, 2020.

[228] F. Bazzi, A. J. Danke, D. B. Lawson, M. Manoli, G. M. Leitus, P. A. Koutentis, and C. P. Constantinides, "1-(2-Methoxyphenyl)-3-phenyl-1,4-dihydro-1,2,4-benzotriazin-4-yl: A tricky "structure-to-magnetism" correlation aided by DFT calculations," *CrystEngComm*, vol. 22, pp. 4306–4316, 2020.

[229] C. Poole and H. Farach, *Handbook of Electron Spin Resonance*. Springer-Verlag: New York, 1999, 1999.

[230] M. Mas-Torrent, N. Crivillers, C. Rovira, and J. Veciana, "Attaching persistent organic free radicals to surfaces: How and why," *Chemical Reviews*, vol. 112, pp. 2506–2527, 2012.

[231] M. Mannini, L. Sorace, L. Gorini, F. M. Piras, A. Caneschi, A. Magnani, S. Menichetti, and D. Gatteschi, "Self-assembled organic radicals on Au(111) surfaces: A combined ToF-SIMS, STM, and ESR study," *Langmuir*, vol. 23, pp. 2389–2397, 2007.

[232] N. Niermann, T. H. Degefa, L. Walder, V. Zielke, H.-J. Steinhoff, J. Onsgaard, and S. Speller, "Galvinoxyl monolayers on Au(111) studied by STM, EPR, and cyclic voltammetry," *Physical Review B*, vol. 74, pp. 1–13, 2006.

[233] Y. Tserkovnyak and A. Brataas, "Enhanced Gilbert Damping in Thin Ferromagnetic Films," *Physical Review Letters*, vol. 88, p. 117601, 2002.

[234] Y. Huo, F. L. Zeng, C. Zhou, and Y. Z. Wu, "Spin pumping and the inverse spin hall effect in single crystalline Fe/Pt heterostructure," *AIP Advances*, vol. 7, p. 056024, 2017.

[235] J. Lustikova, Y. Shiomi, Z. Qiu, T. Kikkawa, R. Iguchi, K. Uchida, and E. Saitoh, "Spin current generation from sputtered Y3Fe5O12 films," *Journal of Applied Physics*, vol. 116, p. 153902, 2014.

[236] M. Filipovic, C. Holmqvist, F. Haupt, and W. Belzig, "Spin transport and tunable Gilbert damping in a single-molecule magnet junction," *Physical Review B*, vol. 87, p. 045426, 2013.

[237] T. Murata, C. Yamada, K. Furukawa, and Y. Morita, "Mixed valence salts based on carbon-centered neutral neutral radical crystals," *Communications Chemistry*, vol. 1, pp. 1–8, 2018.

[238] B. Debska, E. Spychaj-Fabisiak, W. Szulc, R. Gaj, and M. Banach-Szott, "EPR Spectroscopy as a Tool to Characterize the Maturity Degree of Humic Acids," *Materials*, vol. 14, pp. 1–9, 2021.

[239] V. I. Krinichnyi, "Dynamics of spin charge carriers in polyaniline," *Applied Physics Reviews*, vol. 1, p. 021305, 2014.

[240] S. Takahashi, "Giant enhancement of spin pumping in the out-of-phase precession mode," *Applied Physics Letters*, vol. 104, p. 052407, 2014.

[241] Y. Li, W. Cao, V. P. Amin, Z. Zhang, J. Gibbons, J. Sklenar, J. Pearson, P. M. Haney, M. D. Stiles, W. E. Bailey, V. Novosad, A. Hoffmann, and W. Zhang, "Coherent Spin Pumping in a Strongly Coupled Magnon-Magnon Hybrid System," *Physical Review Letters*, vol. 124, p. 117202, 2020.

[242] A. Baker, A. Figueroaa, T. Hesjedalb, and G. van der Laan, "Antidamping torques from simultaneous resonances in ferromagnet- topological insulator-ferromagnet heterostructures," *Journal of Magnetism and Magnetic Materials*, vol. 473, pp. 470–476, 2019.

[243] S. Klingler, V. Amin, S. Geprags, K. Ganzhorn, H. Maier-Flaig, M. Althammer, H. Huebl, R. Gross, R. D. McMichael, M. D. Stiles, S. T. B. Goennenwein, and M. Weiler, "Spin-Torque Excitation of Perpendicular Standing Spin Waves in Coupled YIG/Co Heterostructures," *Phys. Rev. Lett.*, vol. 120, p. 127201, 2018.

[244] L. Wang, Z. Lu, X. Zhao, W. Zhang, Y. Chen, Y. Tian, S. Yan, and L. Bai, "Magnetization coupling in a YIG/GGG structure," *Physical Review B*, vol. 102, pp. 1–6, 2020.

[245] Kenichiro Tanaka, T. Takahashi, T. Ban, T. Kondo, K. Uchida, and N. Miura, "Comparative study on the excitons in lead-halide-based perovskite-type crystals $CH_3NH_3PbBr_3$ $CH_3NH_3PbI_3$," *Solid State Communications*, vol. 127, no. 9–10, pp. 619 – 623, 2003.

[246] M. Cinchetti, V. A. Dediu, and L. E. Hueso, "Activating the molecular spinterface," *Nature Materials*, vol. 16, pp. 507–515, 2017.

[247] K. Wang, Q. Yang, J. Duan, C. Zhang, F. Zhao, H. Yu, and B. Hu, "Spin-Polarized Electronic Transport through Ferromagnet/ Organic–Inorganic Hybrid Perovskite Spinterfaces at Room Temperature," *Advanced Materials Interfaces*, vol. 6, p. 1900718, 2019.

[248] R. Pan, K. Wang, Y. Li, H. Yu, J. Li, and L. Xu, "Spinterfaces Manipulate Large Magnetic Field Effects in 3D and Quasi-2D Organic–Inorganic Hybrid Perovskites," *Advanced Electronic Materials*, vol. 7, p. 2100026, 2021.

[249] M. Li, L. Li, R. Mukherjee, K. Wang, Q. Liu, Q. Zou, H. Xu, J. Tisdale, Z. Gai, I. N. Ivanov, D. Mandrus, and B. Hu, "Magnetodielectric Response from Spin–Orbital Interaction Occurring at Interface of Ferromagnetic Co and Organometal Halide Perovskite Layers via Rashba Effect," *Advanced Materials*, vol. 29, p. 1603667, 2017.

[250] D. Niesner, M. Wilhelm, I. Levchuk, A. Osvet, S. Shrestha, M. Batentschuk, C. Brabec, and T. Fausterl, "Giant rashba splitting in $ch_3nh_3pbbr_3$ organic-inorganic perovskite," *Phys. Rev. Lett.*, vol. 117, no. 126401, 2016.

[251] Y. Zhai, S. Baniya, C. Zhang, J. Li, P. Haney, C.-X. Sheng, E. Ehrenfreund, and Z. V. Vardeny, "Giant rashba splitting in 2d organic-inorganic halide perovskites measured by transient spectroscopies," *Science Advances*, vol. 3, no. 7, 2017.

[252] Y. Yang, S. Feng, Z. Li, T. Li, Y. Xiong, L. Cao, and X. Gao, "Unexpected Outstanding Room Temperature Spin Transport Verified in OrganicInorganic Hybrid Perovskite Film," *Journal of Physical Chemistry Letters*, vol. 10, pp. 4422–4428, 2019.

[253] D. Sun, C. Zhang, M. Kavand, J. Wang, H. Malissa, H. Liu, H. Popli, J. Singh, S. R. Vardeny, W. Zhang, C. Boehme, and Z. V. Vardeny, "Surface-enhanced spin current to charge current conversion efficiency in $CH_3NH_3Br_3$-based devices," *Journal of Chemical Physics*, vol. 151, p. 174709, 2019.

[254] O. Mosendz, V. Vlaminck, J. E. Pearson, F. Fradin, S. Bauer, G. E. W.and Bader, and A. Hoffmann *Phys. Rev. Lett.*, vol. 104, p. 046601, 2010.

[255] S. Kaushik, A. G. Khanderao, P. Gupta, V. R. Reddy, and D. Kumar, "Growth of ultra-thin Cobalt on fullerene (C60) thin-film: in-situ investigation under UHV conditions," *Materials Science Engineering B*, vol. 284, p. 115911, 2022.

[256] A. K. Bera, P. Gupta, D. Garai, A. Gupta, and D. Kumar, "Effect of surface morphology on magnetization dynamics of cobalt ultrathin films: An in-situ investigation," *Applied Surface Science Advances journal*, vol. 6, p. 100124, 2021.

[257] G. Herzer, "Grain size dependence of coercivity and permeability," *IEEE Transactions on magnetics*, vol. 26, pp. 1397–1402, 1990.

[258] C. C. Wang, A. O. Adeyeye, and Y. H. Wu, "Magnetic properties of asymmetric antirectangular $Ni_{80}Fe_{20}$ arrays," *Journal of Applied Physics*, vol. 94, pp. 6644–6648, 2003.

[259] D. J. Dunlop *Phys. Earth Planet. Inter*, vol. 26, 1981.

[260] M. Callsen, V. Caciuc, N. Kiselev, N. Atodiresei, and S. Blugel, "Magnetic hardening induced by nonmagnetic organic molecules," *Physical Review Letters*, vol. 111, p. 106805, 2013.

[261] X. Yu, P. M. Duxbury, G. Jeffers, and M. A. Dubson, " Coalescence and percolation in thin metal films.," *Phys. Rev. B*, vol. 44, 1991.

[262] L. Zhang, F. Cosandey, R. Persaud, and T. E. Madey, " Initial growth and morphology of thin Au films on TiO_2 (110)," *Surf. Sci.*, vol. 73, 1999.

[263] C. Polop, C. Rosiepen, S. Bleikamp, R. Drese, J. Mayer, A. Dimyati, and T. Michely, " The STM view of the initial stages of polycrystalline Ag film formation," *New J. Phys.*, vol. 9, 2007.

[264] G. N. Kakazei, A. F. Kravets, N. A. Lesnik, M. M. P. de Azevedo, Y. G. Pogorelov, and J. B. Sousa, "Ferromagnetic resonance in granular thin films," *Solid State Communications*, vol. 85, 1999.

[265] S. Tomita, K. Akamatsu, H. Shinkai, S. Ikeda, H. Nawafune, C. Mitsumata, T. Kashiwagi, and M. Nagiwara, "Tuning magnetic interactions in ferromagnetic-metal nanoparticle systems," *Phys. Rev. B*, vol. 71, 2005.

[266] S. Kazan, A. Şale, J. Gatiiatova, V. Valeev, R. Khaibullin, and F. Mikailzade., "Magnetic resonance and ferromagnetic behaviour in Fe-implanted $SrTiO_3$," *Solid State Communications*, vol. 150, 2010.

[267] K. Ando, T. Yoshino, N. Okamoto, Y. Kajiwara, K. Sasage, K. Uchida, and E. Saitoh, "Angular dependence of inverse spin-Hall effect induced by spin pumping: Experimental verification of phenomenological model of spin pumping," *Journal of Magnetism and Magnetic Materials*, vol. 322, pp. 1422–1424, 2010.

[268] J. Lindner, I. Barsukov, C. Raeder, C. Hassel, O. Posth, R. Meckenstock, P. Landeros, and D. L. Mills *Phys. Rev. B.*, vol. 80, 2009.

[269] Y. Li, C. Li, Y. Zhao, Q. Lu, Y. Zhao, K. Shi, Z. Zhou, M. Liu, and J. Pan, "Suppressing Magnetic Damping Related to Two-Magnon Scattering in Ultrathin NiFe Films by Interface Engineering," *J. Phys. Chem. C*, vol. 126, pp. 7748–7754, 2022.

[270] Y. Cheng, A. J. Lee, J. T. Brangham, S. P. White, W. T. Ruane, P. C. Hammel, and F. Yang, "Thickness and angular dependent ferromagnetic resonance of ultra-low damping $Co_{25}Fe_{75}$ epitaxial films," *Appl. Phys. Lett.*, vol. 113, p. 262403, 2018.

[271] A. Drovosekov, N. Kreines, A. Barkalova, S. Nikolaev, V. Rylkov, and A. Sitnikov, "Mechanisms of FMR line broadening in $CoFeB - LiNbO_3$ granular films in the vicinity of metal-insulator transition," *Journal of Magnetism and Magnetic Materials*, vol. 495, p. 165875, 2020.

[272] Y. You, H. Sakimura, T. Harumoto, F. Pan, and K. Ando, "Study of spin mixing conductance of single oriented Pt in $Pt/Ni_{81}Fe_{19}$ heterostructure by spin pumping," *AIP Advances*, vol. 11, p. 035211, 2021.

[273] J. Dubowik, K. Załeski, H. Głowinski, and I. Goscianska, "Angular dependence of ferromagnetic resonance linewidth in thin film," *AIP Advances*, vol. 84, p. 184438, 2011.

[274] H. Suhl, "Hole-Conductor-Free, Metal-Electrode-Free TiO2/CH3NH3PbI3 Heterojunction Solar Cells Based on a Low-Temperature Carbon Electrode," *Physical Review*, vol. 97, 1955.

[275] C. Chappert, K. L. Dang, P. Beauvillain, H. Hurdequint, and D. Renard *Phys. Rev. B.*, vol. 34, 1986.

[276] N. Okamoto, H. Kurebayashi, T. Trypiniotis, I. Farrer, D. A. Ritchie, E. Saitoh, J. Sinova, J. Mašek, T. Jungwirth, and C. H. W. Barnes, "Electric control of the spin Hall effect by intervalley transitions," *Nature Materials*, vol. 13, p. 932–937, 2014.

[277] Y. Zhao and K. Zhu, "CH_3NH_3Cl-Assisted One-Step Solution Growth of CH3NH3PbI3: Structure, Charge-Carrier Dynamics, and Photovoltaic Properties of Perovskite Solar Cells," *J. Phys. Chem. C*, vol. 118, p. 9412–9418, 2014.

[278] Y. Zhou, O. S. Game, S. Pang, and N. P. Padture, "Microstructures of Organometal Trihalide Perovskites for Solar Cells: Their Evolution from Solutions and Characterization," *J. Phys. Chem. Lett.*, vol. 6, p. 4827–4839, 2015.

[279] Z. Zhou, Z. Wang, Y. Zhou, S. Pang, D. Wang, H. Xu, Z. Liu, N. P. Padture, and G. Cui, "Methylamine-Gas-Induced Defect-Healing Behavior of $CH_3NH_3PbI_3$ Thin Films for Perovskite Solar Cells," *Angew. Chem.*, vol. 54, p. 9705–9709, 2015.

[280] P. A. Obraztsov, D. Lyashenko, P. A. Chizhov, K. Konishi, N. Nemoto, M. Kuwata-Gonokami, E. Welch, A. N. Obraztsov, and A. Zakhidov, "Ultrafast zero-bias photocurrent and terahertz emission in hybrid perovskites," *Communications Physics*, vol. 1, p. 1–7, 2018.

[281] D. Niesner, M. Hauck, S. Shrestha, and T. Fauster, "Structural fluctuations cause spin-split states in tetragonal $(CH_3NH_3)PbI_3$ as evidenced by the circular photogalvanic effect," *PNAS*, vol. 115, pp. 9509–9514, 2018.

[282] Y. Li, C. Li, Y. Zhao, Q. Lu, Y. Zhao, K. Shi, Z. Zhou, M. Liu, and J. Pan, "Suppressing Magnetic Damping Related to Two-Magnon Scattering in Ultrathin NiFe Films by Interface Engineering," *J. Phys. Chem. C*, vol. 126, pp. 7748–7754, 2022.